RADIATION RESPONSE AND MECHANICAL PROPERTY CHANGES OF CHROMIUM AS ACCIDENT-TOLERANT FUEL CLADDING COATING

A Dissertation

by

ADAM GABRIEL

Submitted to the Graduate and Professional School of
Texas A&M University
in partial fulfillment of the requirements for the degree of

DOCTOR OF PHILOSOPHY

Chair of Committee,	Lin Shao
Committee Members,	Pavel Tsvetkov
	Ahmed Karim
	Kenneth Peddicord
	Kelvin Xie
Head of Department,	Michael Nastasi

December 2021

Major Subject: Nuclear Engineering

ABSTRACT

The main goal is of this study is to surrogate the performance and identify possible challenges of using pure chromium as an accident tolerant fuel coating for existing Zircalloy nuclear fuel cladding. After the 2011 tsunami and subsequent loss of coolant accident in the Fukushima Daichi nuclear power plant a large emphasis has been placed throughout the nuclear community to find a mitigation and prevention of similar accident that are caused by the shortcomings of current zirconium based nuclear fuel cladding. Chromium has been chosen as the subject of this study as it is a prime contender for the usage as an accident tolerant fuel cladding coating due to its ability to withstand high temperature corrosion in aqueous environments, wear resistance and ease of application to already existing fuel cladding. Due to the lack of usage of chromium in its pure form in the nuclear industry little information is available on the performance of it under severe radiation conditions encountered in nuclear reactors. This work is divided into 3 parts to investigate necessary performance data for chromium. In the first part a series of 5 heavy ion (Fe) irradiations at 5 MeV between the temperatures of 450 °C and 650 °C are conducted to a damage levels of 50 dpa and damage rate of $1.75 * 10^{-3} \frac{dpa}{s}$ aimed at finding the peak swelling temperature of chromium and subsequently increasing damage levels to 100 and 150 dpa at the peak swelling temperature to showcase the swelling behavior of chromium. During this first phase void ordering is observed at high damage levels and steady state non saturated swelling of 0.04 - 0.05 %/dpa are found after all data is combined. In the second part of this study the temperature range is increased to 6 temperatures between 350 °C and 650 °C and irradiations at damage rates of $3.5 * 10^{-3} \frac{dpa}{s}$, $3.5 * 10^{-4} \frac{dpa}{s}$ and $3.5 * 10^{-5} \frac{dpa}{s}$ were conducted at each temperature to a fuel relevant peak damage level of 15 dpa. Results show a decrease in peak swelling temperature with increase in damage rate. Applying a relationship of the style $\frac{1}{T} = a * log_{10}(K) + c$ as proposed by Brailsford and Bullough in 1972 enables the extrapolation of the chromium peak swelling temperature to reactor typical damage rates of $1 * 10^{-6} \frac{dpa}{s}$ to $1 * 10^{-7} \frac{dpa}{s}$ yielding peak swelling temperatures of 424 °C and 398 °C respectively. In the last part of the study a 2 MeV proton irradiation of pure chromium is performed, and the increasing damage profile is used to manufacture 4 micro pillars from the same grain with damage levels of 0, 0.5, 0.7 and 1 dpa respectively. Subsequent compression of the pillars sowed an increase of up to 57 % in resolved critical stress after 1dpa damage.

ACKNOWLEDGEMENTS

I would like to thank my committee chair, Dr. Lin Shao, and my committee members, Dr. Ahmed Karim, Dr. Kenneth Peddicord, Dr. Pavel Tsvetkov, Dr. Kelvin Xi and Dr. Francis Garner for their guidance and support throughout the course of this research.

Thanks also go to my friends and colleagues and the department faculty and staff for making my time at Texas A&M University a great experience.

Finally, thanks to my mother and father for their encouragement and to my wife Veda for her patience and love.

CONTRIBUTORS AND FUNDING SOURCES

Contributors

This work was supervised by a dissertation committee consisting of Professor Dr. Lin Shao, Dr. Ahmed Karim, Dr. Kenneth Peddicord, Dr. Pavel Tsvetkov and Dr. Francis Garner of the Department of Nuclear Engineering and Professor Dr. Kelvin Xie of the Department of Material Science and Engineering

Some data used in Chapter 3 of this work was produced in a collaborative effort with Ekaterina Ryabikovskaya and were published in (2021). The micro mechanical testing in Chapter 5 were aided and obtained in collaboration with Miguel Pena

All other work conducted for the dissertation was completed by the student independently.

Funding Sources

The work was supported by the Nuclear Science User Facility (NSUF) under the Rapid Turnaround Experiment (RTE) FY2019 through project 1799.

NOMENCLATURE

Begin Typing Here

ATF	Accident Tolerant Fuel
BCC	Body centered cubic
Cr	Chromium (element)
dpa	Displacement per Atom
EBSD	Electron Backscatter diffraction
FeCrAl	Iron chrome aluminum alloy
FIB	Focused Ion Beam
MAX	early transition-A group carbide
SNICS	Solid Negative Ion Cesium Sputtering Source
SRIM	Stopping Range of Ions in Materials
TEM	Transmission Electron Microscope

TABLE OF CONTENTS

Page

Page

LIST OF FIGURES

LIST OF TABLES

Page

1. INTRODUCTION

Since the catastrophic accident in the Fukushima Daichi nuclear power plant the need for accident tolerant fuel has been showcased and great efforts have been undertaken to find a solution to this shortcoming of current claddings for nuclear fuel assemblies [1]. This chapter provides an overview of the working principles of the world's current Light Water reactor fleet and subsequently details the causes in the Light water reactor of the Fukushima Daichi power plant. Lastly a summery is given on current approaches and candidates on accident tolerant fuel and a case is made for the validity of testing them via Ion irradiation.

1.1 Current fleet of LWRs

1.1.1 Background on LWRs

Light water nuclear reactors form the vast majority of the world's current nuclear reactor fleet consisting of 359 operating reactors producing cumulatively 328.4 gigawatts of energy. The basic working principle of any light water reactor can be boiled down to a nuclear and a conventional part of the power plant. In the nuclear part of the plant nuclear fission of Uranium and the subsequent decay of radioactive products produce heat, that in turn heats water which is used to either directly or indirectly produce steam. The pressurized steam drives steam turbines that in turn power generators producing electricity. Nuclear reactors in which the produced heat during fission directly produces steam are called boiling water reactors and in cases where heat is removed via water and subsequently used to evaporate water in a secondary circle are called pressurized water reactors[2]. In either case of reactor, the water in it serves two important purposes. The first is to cool the nuclear fuel assemblies and to transport the heat away from its generation site. The second purpose is to moderate the fast neutrons emitted during nuclear fission, slowing them down to thermal speeds which increases the probability of said neutron to trigger further fission when impacting another fuel assembly hence driving a nuclear chain reaction [2]. The number of thermal neutrons inside the reactor is controlled via the insertion of control rods that absorb excess neutrons to avoid an uncontrollable runaway of the reactor core. As a result of the nuclear chain reaction the environment in which the nuclear fuel and its cladding operate are subject to some of the most extreme environments encountered in the engineering world being subject to corrosion and stress from water, heat, stress and radiation damage [4]. The current approach for most light water reactors is to use a protective fuel cladding around individual nuclear fuel roads made from Zircalloy [3]. Zircalloy is an alloy consisting of mostly Zirconium and Iron. The main advantage of using Zircalloy in the reactor environment is that it is highly corrosion resistant, has high toughness and has a very low absorption cross section for thermal neutrons not perturbing the thermal neutron flux inside the reactor [5]. With Zircalloy forming a protective sheath around the nuclear fuel roads, it can protect the fuel from failure during excessive heat, shock load and corrosion. Having been used for over 50 years in the light water reactor fleet Zircalloy and its iterations have established excellent performance in reactors and many adverse conditions. One major short coming of Zirconium based cladding though has been made painfully apparent in March 2011 during the disaster that occurred in the Fukushima Daichi nuclear reactor [6].

1.1.2 The Fukushima Daichi accident

In March of 2011 after an earthquake and a 15-meter-high Tsunami hit the nuclear power plant of Fukushima Daichi causing the loss of site power to the 3 of the reactor cores. Due to the loss of power to the reactor units, and failure of the backup power generators the residual heat removal from the reactor cores failed and caused evaporation inside the reactor cores [6]. In light of the evaporation, the nuclear fuel and its cladding exceeded its designed accident temperature for extended period of time. During this excess of the maximum design temperature the Zirconium in the Zircalloy underwent phase change to form β-Zirconium at 863 °C which is highly susceptive to oxidation and undergoes a highly exothermic hydrolysis with the remaining steam and moisture inside the reactor vessel.

$$Zr(c) + 2H_2O(g) \xrightarrow{\text{yields}} ZrO_2(c) + 2H_2(g) + Energy$$

Under this reaction, Zirconium forms Zirconium oxide which is a very hard and brittle ceramic that in turn detaches from the cladding revealing fresh unoxidized Zirconium. With the sheading of the protective zirconium oxide layer fresh metallic zirconium is revealed restarting the oxidation process creating a perpetual cycle. In addition to the reaction products of the oxidation, substantial amounts of heat were released during this reaction as hydrolysis of zirconium is a highly exothermic reaction similar the oxidation of metals in air more commonly known as burning.[7] In the case of the Fukushima Daichi accident the formation of Hydrogen gas in the housing of the reactor became significant enough to form an explosive gas mixture that ignited and caused severe damage to the building around the reactor [8].

1.2 The need for accident tolerant fuel

With the Fukushima Daichi accident in mind a call was send out through the nuclear society to remedy the problem of high temperature hydrolysis of Zirconium based cladding material via the invention and introduction of new materials, coatings, and methods to prevent such catastrophes in case of loss of coolant accidents in light water reactors. The call for a solution was summarized under the umbrella of “Accident tolerant Fuel”. The following chapter will summarize the existing candidates for new fuel claddings and cladding coatings and point out why chromium is a promising candidate as fuel cladding coating and the focus of this study.

1.2.1 MAX- phase coating

One of the promising candidates for creating a coating on zirconium-based fuels are MAX-phase alloys. MAX- phase alloys consist of an early transition metal group of elements present in the “A” group of elements which are located mostly in the IIIA and IVA column of the periodic table and either carbides or nitrides. These MAX-phase alloys exhibit exceptional stability at high temperatures and high resistance to corrosion and radiation damage [9] but have a crucial shortcoming when used in conjunction with zirconium based cladding materials. Under prolonged pressure and heat the MAX phase alloy develops a ceramic phase containing zirconium at the interphase between the coating and fuel cladding [10] which due to its ceramic and therefore brittle nature is likely to fail under stress. Such a failure would cause the coating to delaminate from the cladding preventing a hermetic barrier and allowing leakage of steam towards the cladding rendering the coating useless.

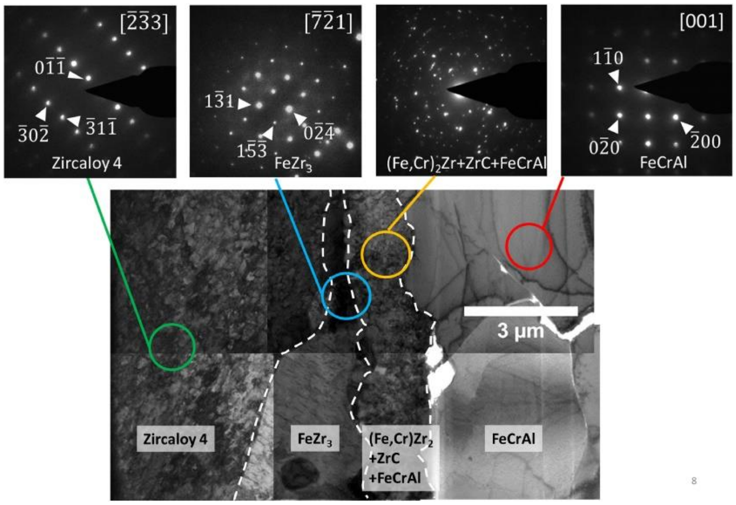

Figure 1.1. TEM cross-section image of FeCrAl coated Zircaloy-4 annealed at 725 C for 500 h. The insets show localized diffraction patterns collected from different phases [11]

1.2.2 Steel coating

The second most prominent material to use as an accident tolerant coating are FeCrAl steels. Such steels are widely used and appreciated in the industry for their mechanical stability and oxidation resistance due to the formation of a passivated chromium and aluminum oxide layer that prevents degradation.[11] A drawback of using FeCrAl coatings is similar to MAX-phase coatings, the interface that it forms with zirconium-based fuel under prolonged heat and pressure. These interfaces have been shown to amorphized under Ion bombardment which indicates poor radiation stability and adverse mechanical properties under prolonged radiation damage [12].

1.2.3 Chromium coatings

Chromium has historically been widely used in nuclear engineering as an alloying material in several stainless steels, which form to this day the backbone of most nuclear reactors.

Chromium as an alloying material provides excellent corrosion resistance for alloys in aqueous and corrosive environments due to its ability to form a passivated oxide layer which protects the underling material from further corrosion and damage [13]. This is accomplished by chromium diffusing from the bulk to the surface of steels and creating said oxide layer. In addition, due to it being a refractory metal chromium improves the hardness of steels and hence aids wear resistance. To this day though chromium has hardly been used in its pure form due to its brittleness and adverse mechanical properties as structural material. Therefore, it has only been used in few instances where it acts as a wear resistant layer between moving parts. Additional reasoning behind the lack of use of chromium is the lack of available swelling data in its pure form and the resulting lack of predictability of its swelling and aging behavior in environments which encounter sever radiation damage.

One of the main advantages of chromium coatings to other competitive coatings for fuel cladding to prevent high temperature hydrolysis is the ease of application and the low cost [13]. Chromium coating on different metals is a well-established process in the surface modification industry as this processes have been used for over 100 years and applied on different alloys. In the past the most common reason for chromium application on surfaces was its superior hardness and wear resistance such as in engine bores, gun barrels or hydraulic cylinders. This applications developed very efficient coating processes such as the galvanic coating of chromium in which the desired part is suspended in a bath of chromium salts dissolved in water and an electrical bias is applied which attracts the free chromium Ions in the solution and deposits them on the desired part [14]. Another more recent development is the method of cold spraying [15]. In this process microscopic chromium particulates are sprayed with high velocities against a substrate and adhesion is achieved purely via the mechanical deformation and interlocking of the micron sized particles. This coating process can be applied independent of the chemistry of substrate and coating and has shown to be reliable method of surface modification.

1.2.4 Previous work and motivation

Chromium as an alloying material has been extensively studied in the field of nuclear material science as a beneficial contributor to different stainless steels, enabling corrosion resistance and increasing hardness. Studies such as one performed by Li Jiang [16] have recently presented a closer look at the swelling behavior of chromium under different adverse nuclear environments such as under the bombardment of Hydrogen, Helium and Iron Ions. This studies though focused on the different affects the incident Ions had on swelling rather than gaining an in depth understanding on how swelling progresses under different radiation fluxes and temperatures. Other publications also presented by Li Jiang [17] investigate the mechanical changes of chromium under gold Ion bombardment and go into great detail of defect evolution dislocation loops and the relationship between columnar grain size and defect density, but again leave out void nucleation and cavity development in chromium. In contrast to this study, work done by Stephen Raiman and Peter Doyle [18,19] show light on the performance of chromium coatings in neutron environments. In a series of studies chromium utilized as hermetic barriers for SiC was irradiated to a neutron fluence of $4.8 * 10^{20} \frac{n}{cm^2}$4.8 >0.1 MeV at 290-340°C particles in the Massachusetts Institute of Technology Nuclear Reactor Laboratory (MITR) for 66 days. Even though in this particular set of studies the chromium among other candidates was used as a coating on SiC, many important findings can also be applied to the current study in which the chromium is used as a coating for Zircalloy based fuel cladding directly.

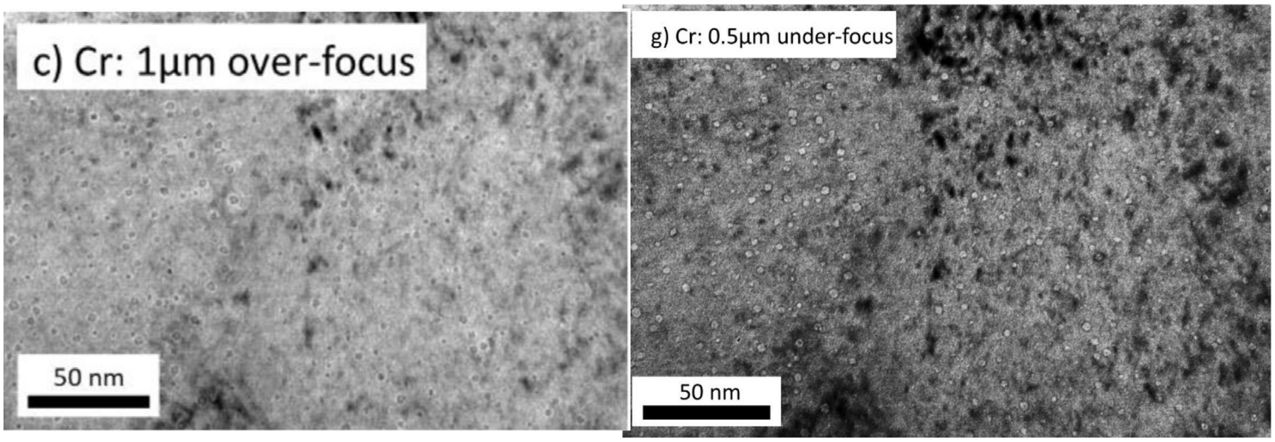

Figure 1.2 Transmission electron micrographs of monolithic Cr exposed to irradiation in an Ar environment to a damage of about 0.5 NRT dpa. c,g correspond to an under-focused beam showing voids in the Cr sample. (reprinted with permission) [18]

Among the main findings, it is reported that 0.2% void swelling was observed in the Cr coating under the mentioned condition which can be used as a verification point for the extrapolation of Cr void swelling under different damage rates. Furthermore, the morphology, size and distribution of the microscopical analysis of the neutron irradiated chromium can be used to compare the case of heavy ion irradiated and neutron irradiated chromium. Further takeaways of this previous studies are the development of cracking under neutron irradiation [18,19]. These results though, must considered carefully as the chromium layers on the substrates were manufactured using cathodic arc physical vapor-deposition (PVD) process, which is a recent development and details on the coating process are still proprietary and may hence affect the physical durability of the coating. Figure 1.4. clearly displays the crack formation of the chromium in the reactor test performed by Raiman et al.

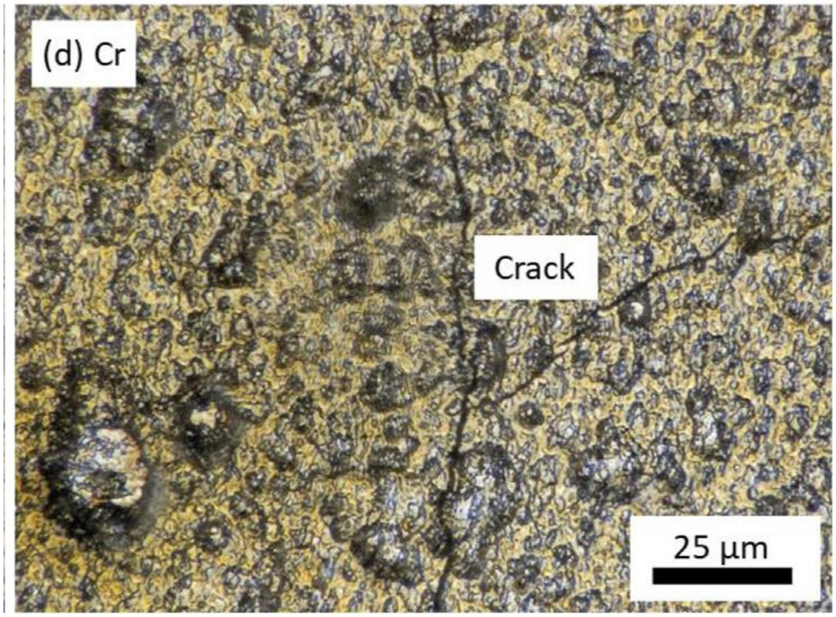

Figure 1.3. Representative optical micrographs demonstrating cracking in dry-irradiated monolithic Cr. (reprinted with permission) [18]

With its intended use as a coating for accident tolerant fuel the particle flux and temperature dependent swelling behavior of chromium is crucial to understand to gage the viability of said coatings. Furthermore, the understanding from analyzing a simple chemical system such as pure chromium which has a body centered cubic structure can give tremendous insight into the mechanics of void nucleation and void evolution in other structural materials. The conclusions drawn in this publication will allow to shed new light on much discussed topics such as the temperature shift in void swelling [20] caused by differences in particle fluxes and the development of nucleated voids such as coalescence or pooling of voids due to Oswald ripening [21].

1.3 Evaluation of Cr for performance as ATF

Considering the main goals of this work are the determination of the radiation stability of pure chromium as a coating for LWR fuel and effects of dose rate and temperature on swelling of chromium, it is important to point out why ion implantations were chosen as the method of damage engineering in chromium.

1.3.1 validity of using heavy ions as surrogate testing for neutron damage

Since damage rate and irradiation time are interconnected and change proportional to each other for constant doses, for example a decrease of two orders in magnitude in damage rate causes a increase of two orders in magnitude in time, a high enough damage rate must be chosen as a starting point for a irradiation matrix. The highest damage rate must create damage fast enough so that experiments are executable in reasonable time when damage rates are decreased over two orders of magnitude which in turn increase the experiment time over two orders of magnitude. The only viable solution to this restraint is offered through the use of particle accelerators which are able to create high damage levels in materials in short periods of time while producing damage characteristics in the target material comparable to nuclear reactors.

When the damage cascades caused by neutrons and Ions are compared, it can be seen from Figure 1.5. that the size, survivability, and energy deposition of damage cascades imparted from heavy ions and neutrons are on a similar scale and therefore produce similar damage patterns.

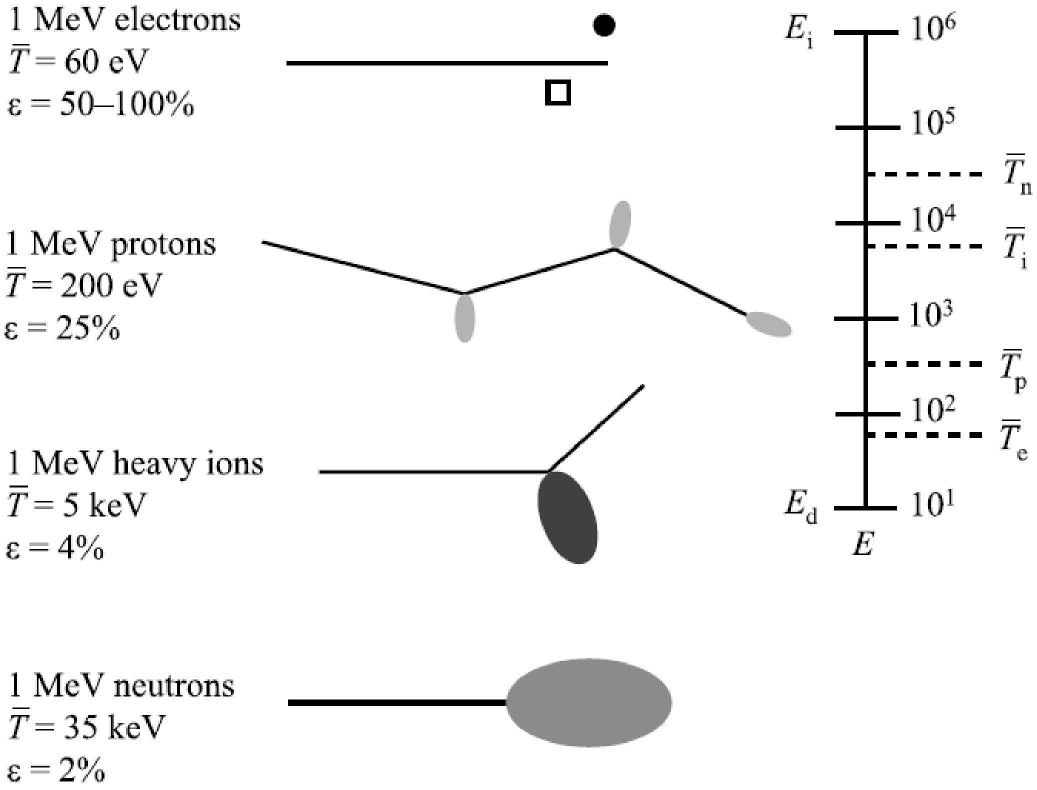

Figure 1.4 Damage cascade size and survivability of different target particles. (reprinted with permission) [27]

As determining the relationship between damage per implanted Ion for ion irradiations can be very challenging and is nearly impossible to achieve with deterministic formulas for large numbers of Ions, a suitable empirical method was used. As the number of Ions interacting with the sample is very large a statistical approach for the calculation of damage per Ion is used. This statistical approach was accomplished by using a Monte Carlo type simulation called Stopping range of Ions in Matter (SRIM). In this simulation designed by Ziegler [22], the Kinchen Pease approach with utilization of the Ziegler-Biersack-Littmark (ZBL) potential for interatomic interaction was chosen for the simulation of damage created by the impeding Iron ions.

The Kinchen Peas model was chosen as it reflects the closest approximation of damage heavy Ions create when compared to neutrons [23]. The purpose of this simulation was to determine the ideal penetration depth for Iron Ions in Chromium, the damage created along their trajectory and the deposition of Iron Ions in the bulk. These parameters as well as restrictions of the equipment determine the Ion energy and flux ranges of Ions within the series of experiments. As any Monte Carlo simulation SRIM relies on the validity of the assumption that the population of particles run in the simulation is large enough to reflect the behavior of an infinite number of particles. This assumption is achieved by running a total of 99999 Ions in the simulation.

Even with a such large number of particles run in the simulation there are some uncertainties associated with the simulation which arise from deviations in the uniformity of the substrate, number density and purity of the substrate. These deviations are only secondary in nature though and do not contribute to significant error in the experiment. With the resulting averaged damage events per Ion as well as the Ion distribution, a depth dependent graph can be developed that gives insight into the damage distribution along the Ion trajectory as well as the distribution of implanted Ions into the sample.

As seen in Figure 1.5. which displays the damage and ion distribution inside a bulk chromium sample irradiated with 5 MeV Iron ions to a peak damage of 15 DPA a peak concentration of 0.4% Iron is implanted. This introduction of a foreign chemical substance as well as several other ion-specific effects introduce some complexity to the series of experiments that must be treated with great care to derive usable and reliable results.

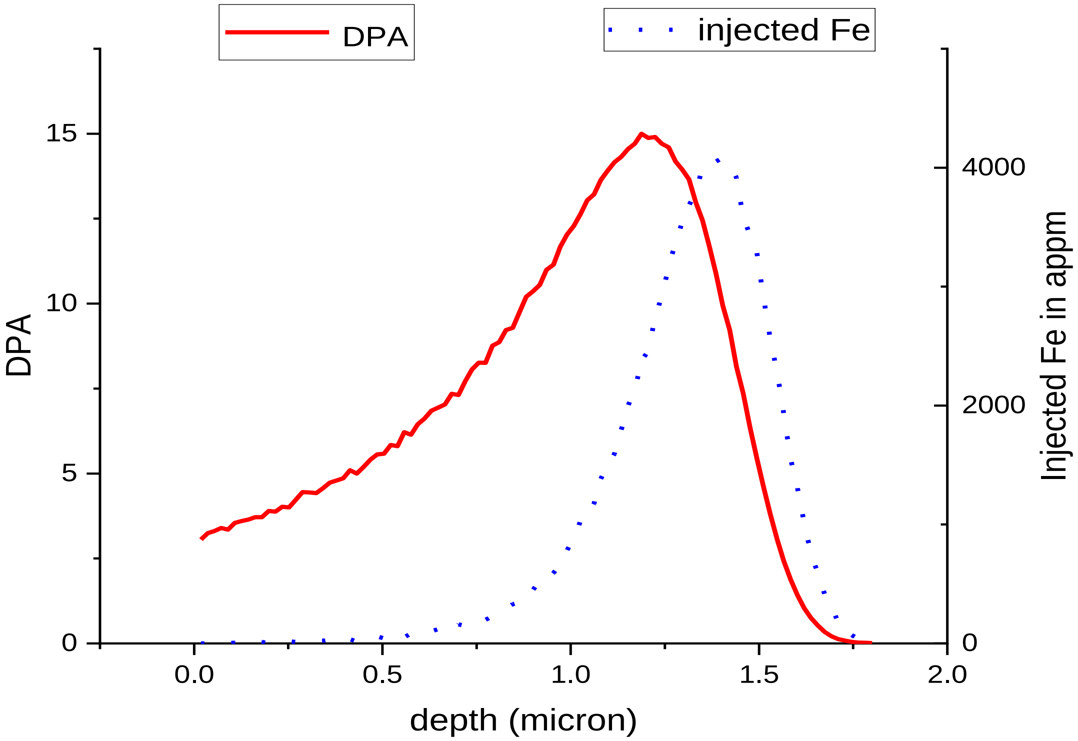

Figure 1.5. SRIM simulation of damage profile and implantation profile produced by 5 MeV Iron ions in pure Cr. This profile was obtained via using Kinchen-Peas calculation mode and assumes a dose $1.5 * 10^{16}\ \frac{\text{Ions}}{\text{cm}^2}$.

A dose of 15 DPA in pure chromium was chosen for all heavy ion irradiations, as this dose is sufficient to promote swelling in chromium as suggested by Ribjakovskaja et al. but at the same time is representative of the dose experienced by fuel claddings on conventional LWR fuels. Furthermore the low dose of 15 DPA keeps the time required for low damage rate experiments within a reasonable time frame of 120 hours per sample. Since one of the main goals of this work is to establish usable swelling data for pure chromium in nuclear environments which includes to a great extend nuclear reactors that experience neutron flux, great care must be taken to account for ion-specific effects that occur during the irradiation of nuclear materials with particle accelerators.

The first effect that must be accounted for is the surface effect in Ion irradiated samples. The free surface of any ion irradiated sample acts as a perfect defect sink and therefore tends to absorb any defects that are formed in its vicinity. This absorption of defects causes a depletion of vacancies and voids near the surface and suppresses swelling in the near surface regions. To avoid any ion-specific effects in the swelling analysis of the samples this near surface region must be excluded in the swelling analysis as it will have lower numbers in voids and less swelling than a sample with the same nominal damage caused by neutrons.

The second Ion-specific effect that must be avoided is the swelling suppression of the injected ions in the stopping region of the implanted ions. As each implanted ion stops in the target material, it acts at is resting site as one half of a frank loop effectively producing an excess interstitial. This excess interstitial than is free to diffuse and preferentially combines with vacancies formed from the damage cascades of previous ion tracks. This recombination of vacancies prevents the vacancies from clustering and creating voids, effectively suppressing void swelling. In order to exclude this second ion specific effect from the swelling analysis of pure chromium any swelling data effected by these injected interstitials must be discarded. In this particular series of experiments additional complications arise due to the use of chemically different elements for Ion and target substrate. The chemical difference is kept to a minimum though with a simulated maximum concentration of 0.4% of Iron in bulk chromium. With such low concentrations of foreign metal in the bulk chromium no significant affect from diffusion of Iron into the bulk chromium is expected.

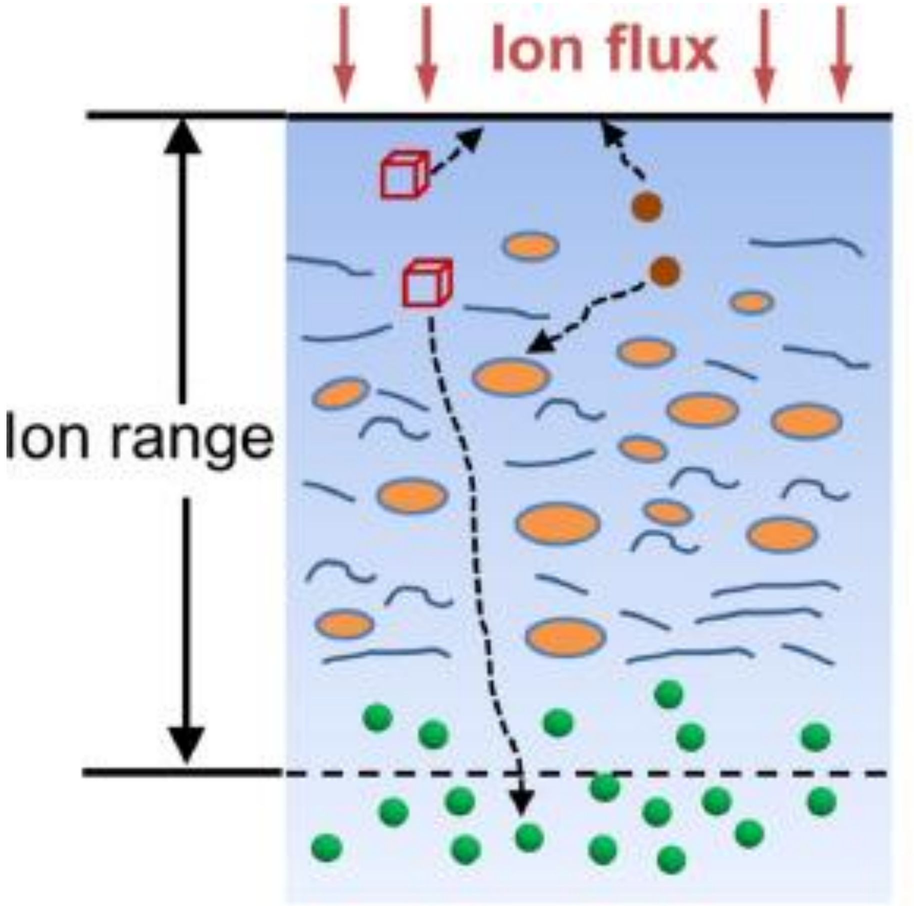

Figure 1.6. Schematic of Ion specific effects encountered when comparing void swelling induced via neutron damage versus heavy ion irradiation.

1.3.2. Modeling approaches to connect heavy ion and neutron flux rates

A major topic that must be addressed and also greatly affects the ability of heavy-ions surrogating neutron damage in reactor materials is the vastly different damage rates that materials experience in nuclear reactors versus accelerator driven damage engineering. The difference in conditions between accelerator and reactor damage levels is illustrated visually in Figure 1.8.

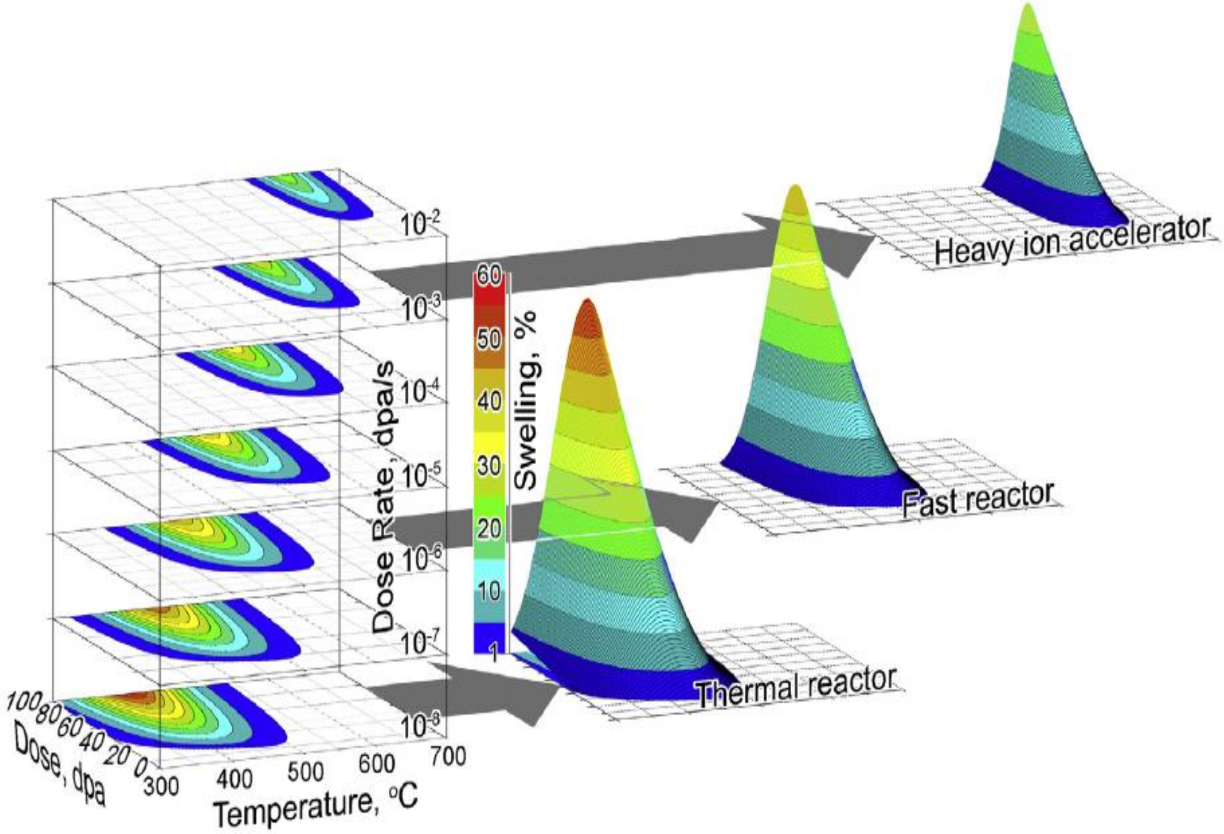

Figure 1.7. Peak swelling temperature shift experienced due to change in damage rate in different nuclear systems. (reprinted with permission) [26]

A model commonly used to address and model the behavior of nuclear materials subject to impeding damage is rate theory. In this approach, the assumption is made that the overall tallying of all sums of specific defects inside a material can be modeled via the summation of all in-fluxes, out-fluxes, generation, and recombination of all specific types of defects.

$$K - D_i C_i k_i^2 - \alpha c_i c_v = 0 \qquad K' - D_v C_v k_v^2 - \alpha c_i c_v = 0 \qquad \text{Eq. 1}$$

With solutions of the forms

$$c_i = \left(\frac{D_v k_v^2}{2\alpha}\right)\left[-(1+\mu) - \{(1+\mu)^2 + \eta\}^{\frac{1}{2}}\right] \quad \text{Eq. 2}$$

$$c_v = \left(\frac{D_i k_i^2}{2\alpha}\right)\left[-(1-\mu) + \{(1+\mu)^2 + \eta\}^{\frac{1}{2}}\right] \quad \text{Eq. 3}$$

The most commonly known formulation of rate theory as applied to comparisons between heavy-ion and neutron damage has been formulated by Mansur in his paper "CORRELATION OF NEUTRON AND HEAVY-ION DAMAGE * II. The predicted temperature shift if swelling with changes in radiation dose rate" in which he predicts the change of peak swelling temperature with increasing damage rate[24]. In his formulation Mansur assumes that the sink strengths referred to as "S" in the formulations can be assumed as a summation of all contributions from sinks $S = \sum_i K^i/D$ to a specific type of defect (vacancies or interstitials). This approach makes the assumption that defects and clusters such as vacancies or interstitial loops have non-biased time independent affinities for specific types of defects. This approach though neglects the true nature of many defects and defect clusters that might have either true neutral bias such as voids or incoherent precipitates, variable-bias such as finite capacity vacancies or coherent precipitates, and lastly true fixed bias sinks such as interstitial loops. [25]. This important distinction of defect affinities and types based on their classification has been made though by the works of Brailsford and Bullough in their 1972 paper "The rate theory of swelling due to void growth in irradiated metals"[25]. In the more concise approach taken by Brailsford and Bullough, the defect generation rates K and K' are taken to be specific dose rate dependent generation terms based on the specific type of defect that are generated from external production (Ion beam) and k is denoted as the loss term for each type of defect.

$$(K' = K + K_1 + K_n) \qquad \text{Eq. 4}$$

$$k^2 = k_1^2 + k_2^2 + k_3^2 + \cdots = k_1^2 + k_n^2 \qquad \text{Eq. 5}$$

With these important distinctions, a dose rate dependent formulation can be made which considers different generation and combination rates for fixed-bias, variable-bias and neutral defect sinks with variable defect production rate for vacancies and interstitials.

$$c_i = \left(\frac{D_v k_v^2}{2\alpha}\right)[-(1+\mu) - \{(1+\mu)^2 + \eta\}^{\frac{1}{2}}]$$

$$\eta = 4\alpha K / D_i D_v k_i^2 k_v^2 \qquad \text{Eq. 6}$$

Individual loss terms based on fixed-bias, variable-bias and neutral defect sinks

$$c_v = \left(\frac{D_i k_i^2}{2\alpha}\right)[-(1-\mu) + \{(1+\mu)^2 + \eta\}^{\frac{1}{2}}]$$

$$\mu = (K' - K)\eta / 4K \qquad \text{Eq. 7}$$

$$(D_v c_v - D_i c_i - D_v \bar{c}_{vs}) 4\pi r_s C_s = \frac{d}{dt}\left(\frac{\Delta V}{V}\right) = \textit{Void swelling} \quad \text{Eq. 8}$$

With these insights a prediction can be made on the varying swelling behavior of materials under varying damage rates and temperatures.

$$\frac{\Delta V}{V} = \left(\frac{\Delta V}{V}\right)_0 F(\eta) \quad \text{Eq. 9}$$

$$F(\eta) = \left(\frac{2}{\eta}\right)\left[-(1+\mu) - \{(1+\mu)^2 + \eta\}^{\frac{1}{2}} - \zeta\eta\right] \quad \text{Eq.10}$$

$$\zeta(T) = \frac{D_v(Z_v \varrho_d + 4\pi r_s C_s)\left\{Z_i \varrho_d + 4\pi\left(r_s C_s + r_p C_p\right)\right\}}{2K(Z_i - Z_v) * \varrho_d\left\{Z_v \varrho_d + 4\pi\left(r_s C_s + r_p C_p\right)\right\}} * \quad \text{Eq.11}$$

$$\left[4\pi r_p C_p \bar{c}_{vs} + Z_v\left\{\varrho_d^n(\bar{c}_{vs} - c_v^e) + \varrho_d^l(\bar{c}_{vs} - \bar{c}_{vL})\right\}\right]$$

Where ζ is composed from several material constants. This function $F(\eta)$ with its high dependence on damage rate is especially interesting when plotted under varying damage rates usually encountered in neutron irradiated materials in reactors and damage inflicted using particle accelerators.

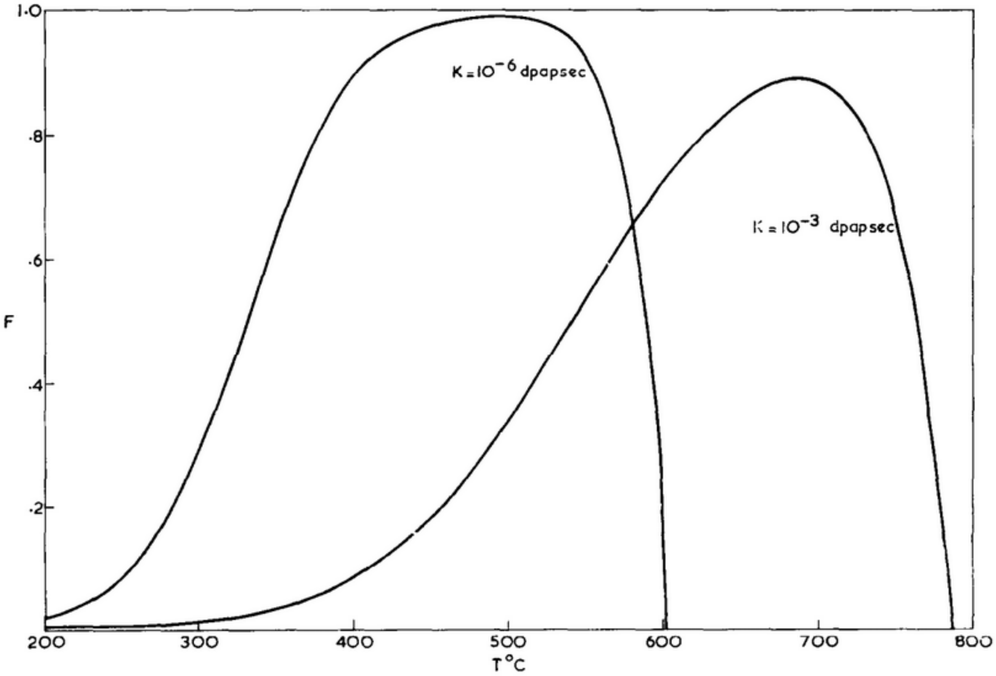

Figure 1.8. The variation of F((η)) in eq. (10) with temperature to illustrate the shift of the peak with dose rate K. (reprinted with permission) [25]

As seen in the above figure an increase in damage rate suggests an increases in peak swelling temperature and vice versa. With the current work on chromium the basis of these theoretical prediction can be supported and allows the void swelling behavior of chromium to be further extrapolated into the low damage rate region of current light water reactors yielding the required information for the surrogating of chromium coatings as an accident tolerant fuel at the fraction of cost of actual neutron testing.

1.3.3 Validity of using protons to create suitable damage for mechanical testing

As mentioned previously, radiation damage in nuclear environments can be readily simulated via the use of heavy ions as the damage cascades produce by latter are closely comparable to damage cascades created by neutrons. An inherent disadvantage of heavy ion irradiation is the limited penetration depth of the impending ion and the resulting limited usable analysis region. This limitation can be overcome for void analysis via the use of cross-sectional TEM but is more difficult to deal with when mechanical testing is undertaken. The most viable solution to overcome the limited range of heavy ion irradiation is the use of light ions such as protons which create a much deeper and flat damage profile. This deep and flat damage profile is suitable for fabrication of micron sized pillar which subsequently can be compressed via nano indentation and yield valuable mechanical data. The use of protons to create flat damage profile carries distinctive disadvantages though. With the use of heavy ions and the increase of damage with increasing depth in a single sample, it is possible to extract defect information with respect to damage levels via the discretization of the sample’s depth into different damage region. With a flat damage profile such as seen in proton irradiation this method is not possible because the usable damage region for swelling or mechanical analysis has the same damage level throughout and therefore the analysis at any point yields the same result.

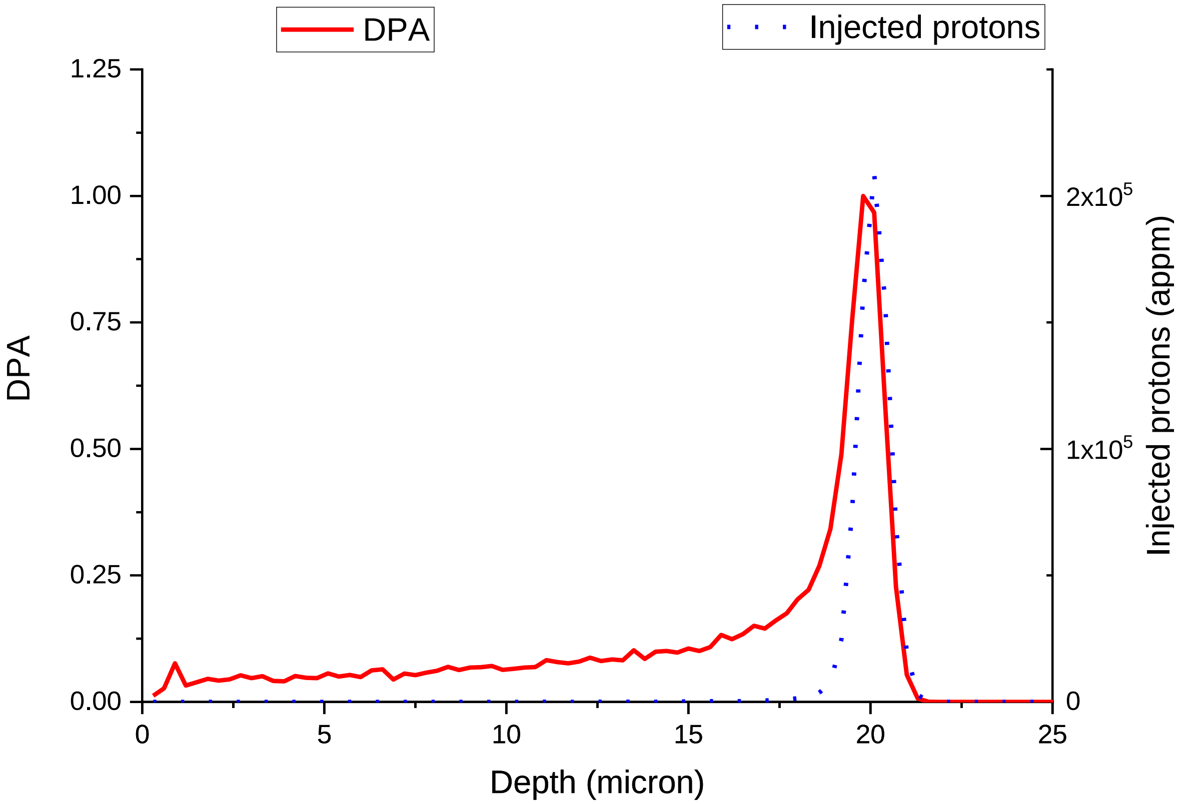

Figure 1.9. SRIM simulation of damage profile produced by 2 MeV protons in pure Cr using Kinchen-Peas calculation mode.

1.4 References

[1] World Nuclear Association, Fukushima Daiichi Accident, Updated October 2018.

[2] Eugene Shwageraus, Advanced Light Water-Cooled Reactor Concepts, Editor(s): Ehud Greenspan, Encyclopedia of Nuclear Energy, Elsevier, 2021, Pages 582-601

[3] P. Rodriguez, Nuclear Reactor Materials: Irradiation Effects, Editor(s): K.H. Jürgen Buschow, Robert W. Cahn, Merton C. Flemings, Bernhard Ilschner, Edward J. Kramer, Subhash Mahajan, Patrick Veyssière, Encyclopedia of Materials: Science and Technology, Elsevier, 2001, Pages 6349-6361

[4] Edward A. Kenik, Jeremy T. Busby, Radiation-induced degradation of stainless steel light water reactor internals, Materials Science and Engineering: R: Reports, Volume 73, Issues 7–8, 2012, Pages 67-83,

[5] Raghvendra Tewari, Karri V. Mani Krishna, Suman Neogy, Clément Lemaignan, 7.08 - Zirconium and its Alloys: Properties and Characteristics☆, Editor(s): Rudy J.M. Konings, Roger E. Stoller, Comprehensive Nuclear Materials (Second Edition), Elsevier, 2020, Pages 284-302

[6] World Nuclear Association, Fukushima Daiichi Accident, Updated October 2018.

[7] Macdonald, D., Urquidi-Macdonald, M., Chen, Y., Ai, J., Park, P., & Kim, H. (2006, December 12). Oxidation of Zircaloy Fuel Cladding in Water-Cooled Nuclear Reactors. OSTI. https://www.osti.gov/biblio/896213

[8] Fujisawa, S. Liu, T. Yamagata, Numerical study on ignition and failure mechanisms of hydrogen explosion accident in Fukushima Daiichi Unit 1, Engineering Failure Analysis, Volume 124, 2021, 105388,

[9] Garcia-Diaz, Brenda & Olson, Luke & Verst, C. & Sindelar, Robert & Hoffman, E. & Hauch, Benjamin & Maier, Benjamin & Sridharan, K.. (2014). MAX phase coatings for accident tolerant nuclear fuel. Transactions of the American Nuclear Society, 110, p. 994-996

[10] Jonathan G. Gigax, Miltiadis Kennas, Hyosim Kim, Tianyao Wang, Benjamin R. Maier, Hwasung Yeom, Greg O. Johnson, Kumar Sridharan, Lin Shao, Radiation response of Ti2AlC MAX phase coated Zircaloy-4 for accident tolerant fuel cladding, Journal of Nuclear Materials, Volume 523, 2019, Pages 26-32,

[11] Miltiadis Kennas, Hyosim Kim, Jonathan G. Gigax, Tianyao Wang, Benjamin R. Maier, Hwasung Yeom, Greg O. Johnson, Tyler Dabney, Kumar Sridharan, Kenneth L. Peddicord, Lin Shao, Radiation response of FeCrAl-coated Zircaloy-4, Journal of Nuclear Materials, Volume 536,

[12] 2020Thermo-mechanical analysis of SiC and FeCrAl cladding behavior under a loss-of-coolant accident, Prepared for U.S. Department of Energy, 2018.

[13] Giovanni Bolelli, Roberto Giovanardi, Luca Lusvarghi, Tiziano Manfredini, Corrosion resistance of HVOF-sprayed coatings for hard chrome replacement, Corrosion Science, Volume 48, Issue 11, 2006,

[14] Aimin Liang, Yuwen Li, Hongyu Liang, Liwei Ni, Junyan Zhang, A favorable chromium coating electrodeposited from Cr(III) electrolyte reveals anti-wear performance similar to conventional hard chromium, Materials Letters, Volume 189, 2017, Pages 221-224,

[15] Martin Ševeček, Anil Gurgen, Arunkumar Seshadri, Yifeng Che, Malik Wagih, Bren Phillips, Victor Champagne, Koroush Shirvan, Development of Cr cold spray–coated fuel cladding with enhanced accident tolerance, Nuclear Engineering and Technology, Volume 50, Issue 2, 2018, Pages 229-236,

[16] Hyun-Gil Kima,*, Jae-Ho Yanga, Weon-Ju Kimb, and Yang-Hyun Koo. (2015, December 11). Development Status of Accident-tolerant Fuel for Light WaterReactors in Korea. Www.Core.Ac.Uk. https://core.ac.uk/download/pdf/82760258.pdf

[17] Kurt A. Terrani, Accident tolerant fuel cladding development: Promise, status, and challenges, Journal of Nuclear Materials, Volume 501, 2018, Pages 13-30, ISSN 0022-3115

[18] Peter J. Doyle, Takaaki Koyanagi, Caen Ang, Lance Snead, Peter Mouche, Yutai Katoh, Stephen S. Raiman, Evaluation of the effects of neutron irradiation on first-generation corrosion mitigation coatings on SiC for accident-tolerant fuel cladding, Journal of Nuclear Materials, Volume 536, 2020, 152203

[19] Stephen S. Raiman (ORNL), Peter J. Doyle, Caen Ang (ORNL/Univ of Tennessee), Takaaki Koyanagi (ORNL), David M. Carpenter (MIT), Kurt A. Terrani, Yutai Katoh (ORNL), Irradiation-Induced Cracking of Dual-Purpose Coatings on SiC,, Proceedings | 19th International Conference on Environmental Degradation of Materials in Nuclear Power Systems - Water Reactors | Boston, MA, August 18-22, 2019 | Pages 428-433

[20]] L.K. Mansur, Correlation of neutron and heavy-ion damage. II. The predicted temperature shift of swelling with changes in radiation dose rate. J. Nucl. Mater. 78, 156–160 (1978).
[21] J.A. Marqusee and John Ross, Theory of Ostwald ripening: Competitive growth and its dependence on volume fraction, J. Chem. Phys. 80 (1984) 536-543

[22] James F. Ziegler, M.D. Ziegler, J.P. Biersack, SRIM – The stopping and range of ions in matter (2010),
Nuclear Instruments and Methods in Physics Research Section B: Beam Interactions with Materials and Atoms, Volume 268, Issues 11–12, 2010, Pages 1818-1823

[23] R.E. Stoller, M.B. Toloczko, G.S. Was, A.G. Certain, S. Dwaraknath, F.A. Garner, On the use of SRIM for computing radiation damage exposure, Nuclear Instruments and Methods in Phys. Res. B 310, (2013) 75-80

[24] L.K. Mansur, Theory of transitions in dose dependence of radiation effects in structural alloys, Journal of Nuclear Materials 206, 306-323 (1993)

[25] A.D. Brailsford, R. Bullough, The rate theory of swelling due to void growth in irradiated metals, J. Nucl. Mat. 44, 121-135 (1972).

[26] A.S. Kalchenko, V.V. Bryk, N.P. Lazarev, V.N. Voyevodin, F.A. Garner,
Prediction of void swelling in the baffle ring of WWER-1000 reactors for service life of 30–60years, Journal of Nuclear Materials, Volume 437, Issues 1–3, 2013, Pages 415-423,

[27] Was, GS, Allen, TR (1994) Mater. Character. 32, p. 239

2 EXPERIMENTAL PROCEDURES: EQUIPMENT AND TECHNIQUES

The following chapter will outline in detail the equipment used in during the experiment and the procedure followed to ensure good data acquisition and accuracy. As the use of particle accelerators, as well as nano scale microscopy equipment such as the FIB and TEM are quite intricate, a detailed description of their working principles and operation are detailed as they will aid to understand the results and limitations of this work.

2.1 Sample preparation

2.1.1 Alloy manufacturing

The chromium used for the series was purchased from Goodfellow United States with a part number CR006115 and a purity of 99.95%. The pure metal is delivered in Lump from which have an average thickness of 0.5mm. The purification of the metal was achieved via hydrogen sparging.

Figure 2.1. Image of pure chromium platelets used in experiments in comparison to a quarter dollar coin.

2.1.2 Surface preparation

In order to provide a usable surface for the ion irradiation and to remove any surface deformation from the sample the chromium samples were polished using Silicone carbide sand with a 2400 grid, and subsequently, electro polished using a Tenupol 5 twin jet electro-polisher. The acid-solution deemed the most appropriate for polishing was 5% perchloric acid mixed with 95% methanol. The etching duration for each individual sample was ~20 seconds with a voltage bias of 19.5 V between the sample and perchloric acid. After the polishing remaining acid residue was removed by repeatedly rinsing the samples in methanol. Samples were then dried with nitrogen gas

2.2 Ion irradiation using particle accelerator

The irradiations conducted for this series of experiments was performed on a 3 Mv National Electrostatic accelerator. This type of accelerator is a linear accelerator of tandem style utilizing a positive acceleration potential. There are several main components that impact the experiment and the operation of the accelerator.

2.2.1 Accelerator background low energy

The SNICS ion source

As this particular series of experiments used Ions generated from a solid metal, the most practical choice of Ion source was the Source of Negative Ions by Cesium sputtering. In this type of Ion source, a solid cathode is inserted into an high vacuum chamber. Inside the same vacuum chamber the outlet of a small oven is mounted containing metallic Cesium. Cesium is a highly reactive alkali metal that melts at relatively low temperatures of 40 C and evaporates around 90 C in high vacuum conditions. This oven is heated via an external heater controlled via the accelerators control panel. The purpose of this Cesium oven is to evaporate small amounts of pure Cesium into the high vacuum chamber containing the Cathode. In addition to the cathode and the outlet of the Cesium oven the Ion source vacuum chamber also contains a filament made from tantalum that acts as an Ionizer. The Ionizer is operated via heating the Tantalum filament to 1200 C by running electric current of up to 25 A through it. The Ionizing effect of the filament is achieved by the thermoelectric emission of the hot Tantalum and the thermal excitation of surrounding atoms and molecules. The purpose of the Ionizer is to Ionize the evaporated Cesium from the source oven.

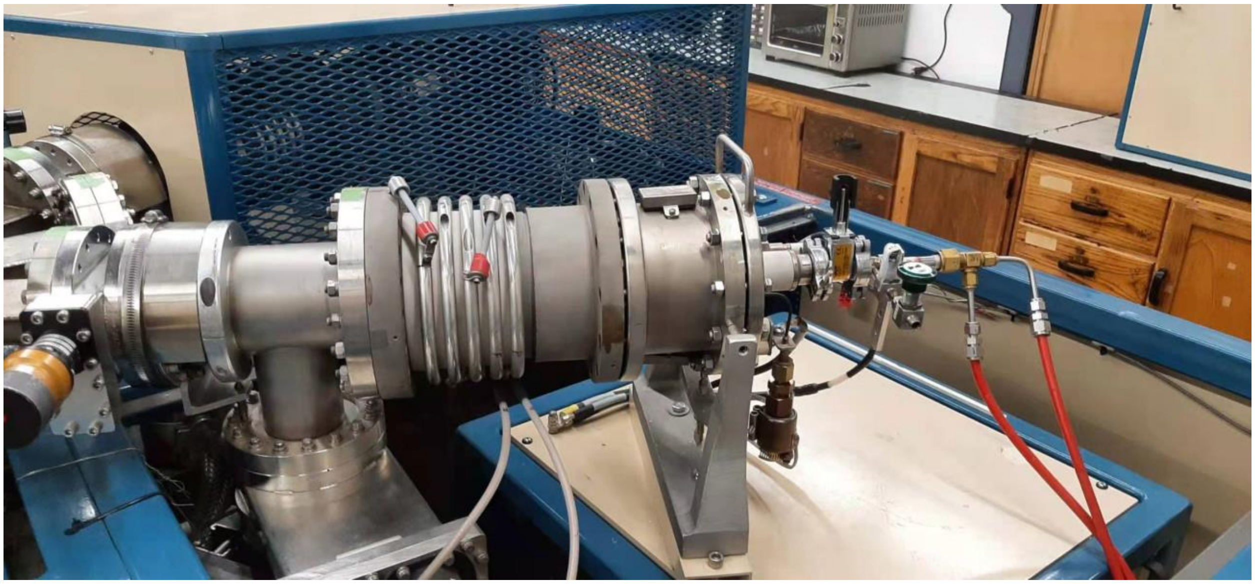

Figure 2.2. Image of a National Electrostatic Solid Negative Ion Cesium Sputtering Ion Source (SNICS) used for the production of Iron ions.

With the Cesium ions ionized they are drawn to the cathode via a potential difference of 6 kilo Volts. By traveling through this potential, the Cesium Ions and clusters gain kinetic energy which they will deposit into the surface of the metallic cathode upon impact. During the impact the cesium will sputter substrate atoms off the surface very similar to the dust thrown up when a large stone is dropped into dust. Subsequently the sputtered substrate atoms will undergo a chemical electron exchange with the Cesium present in the vicinity of the sputtering.

During this electron exchange the cesium gives off an electron to the sputtered material and therefor creates negative Ions. In order to extract this negative Ions from the source chamber, a positive extraction Bias is applied that will draw the negative ions just produced by the Cesium sputtering out of the immediate source vacuum chamber and into the focusing part of the Ions source. The entire source assembly is electrically isolated from ground via several ceramic stand offs and a source cage with an interlock that will automatically shut of power to the Ion source when the source cage is moved.

The low energy focusing

Once the negative Ions are extracted from the immediate source vacuum chamber the stream of ions is still rather brough and uncollimated similar to the light of an open light bulb shining into a broad direction. In order to shape the Ions into a collimated beam, that is pure in its Ion species, the beam passes through an Einzel Lens. This type of lens consists of 3 sets of electrically isolated rings concentric with the axis of the Ion beam, with the first and last ring being grounded and respect to the middle ring which is charged to negative potential of up to 16 kilo volts. This electrical connection between the 3 rings of the Einzel lens creates an electric field whose shape is depicted in Figure x. Through the use of this electrostatic setup a focusing effect is achieved without the alteration of the energy of the incoming beam. After being collimated the beam still contains several different trace amounts of ions as no cathode substrate is absolutely pure. In order to rid the beam of unwanted Ions the beam is deflected through an angle of 45 degrees by the means of an injector magnet.

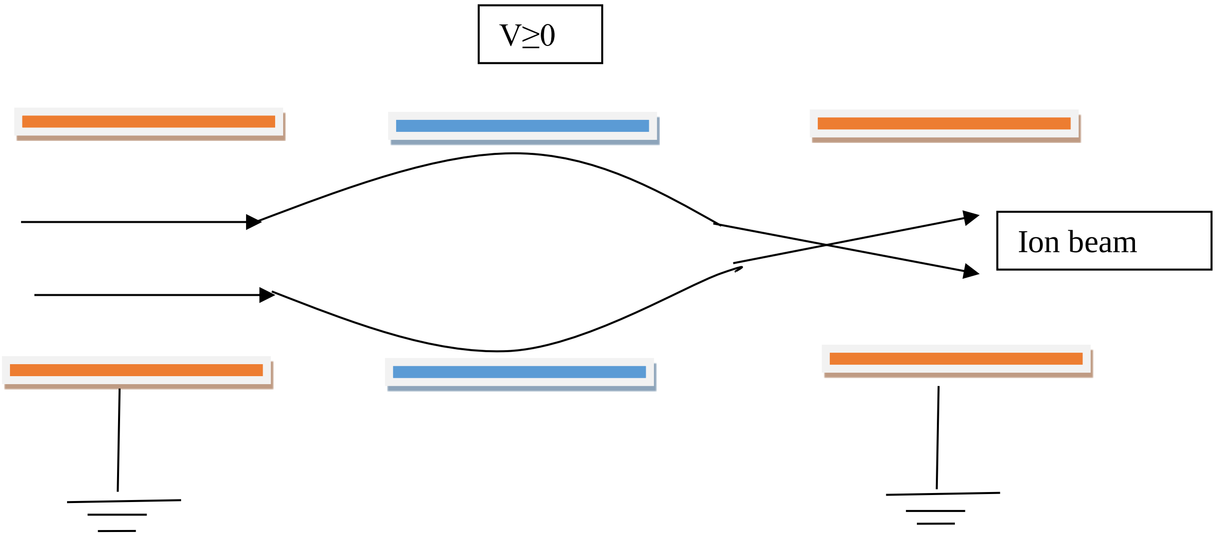

Figure 2.3. Schematic of electrical wiring and ion trajectory induced by an Einzel-lense used for focusing ion beams

The injector magnet is a large electromagnet that is situated over a flat vacuum chamber at the 45 degrees turn. The filtering effect of the magnet is achieved because each Ion entering the magnetic field has the same energy as they all traversed the same extraction potential, but due to their different masses each Ion has a different velocity. The magnetic field of the injector magnet acts on each ion traversing the field with a strenght proportional to the Ions speed and therefore dictating a speciefied radius of curvature of the ions tracjectory. With knowledge of the energy, mass and radius of curvature of vaccum chamber inside the injector magnet the appropriate magnetic field can be calculated to only pass the correct Ions through the apparature at the exit of the injector magnet vaccum chamber. By applying this knowledge to the Ions species used the beam is cleaned and collimated. After the cleaning process a faraday cup is used to measure the intensity of the Ion beam.

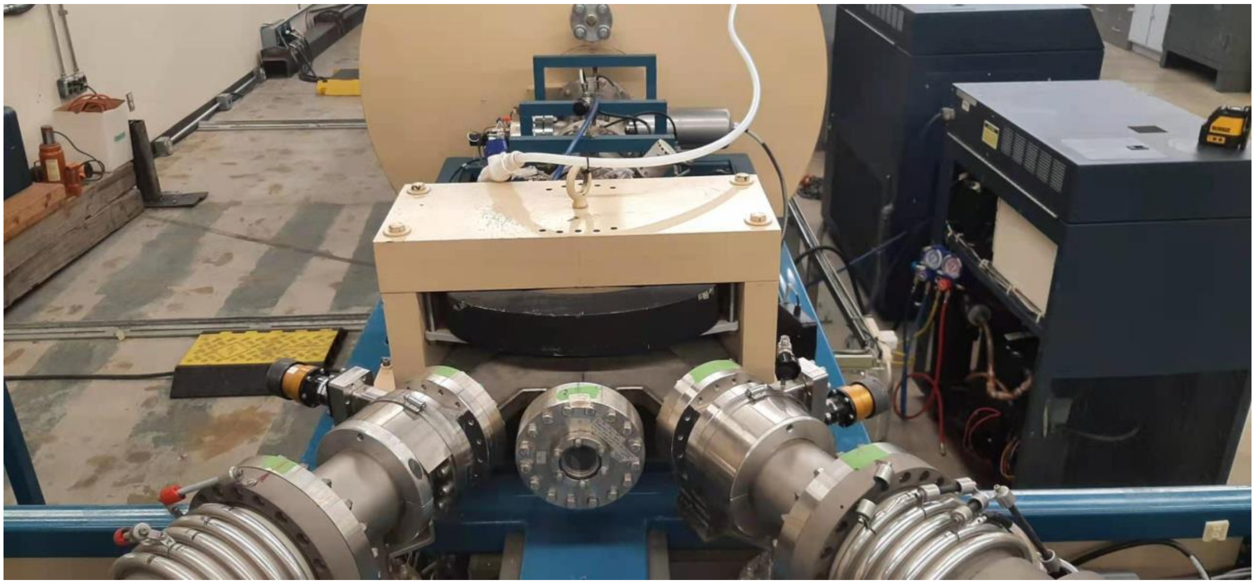

Figure 2.4. Low energy switch magnet with SNICS ion source and RF ion source feeding into the magnet chamber.

2.2.2 Accelerator background high energy

The acceleration path

The heart of the particle accelerator is the accelerator itself which in the case of the 3 Mv national electrostatic is a tandem accelerator with an Van de Graff generator that provides the positive terminal voltage. Utilizing an tandem accelerator system in opposite to a regular accelerator system has several technical advantages that enable the use of higher energy ions being used in experiments while maintaining an comparatively low acceleration voltage. A tandem accelerator is design in which the ion entering the acceleration path is drawn towards a high potential in the center of the accelerator and changes it’s charge state in the center of the of the acceleration path to then be subsequently accelerated away from the high voltage terminal. This change of charge state is accomplished by injecting a low density cloud of nitrogen inside the center of the acceleration column of the accelerator. The nitrogen acts as a chemical electron capturing agent, similar but in an opposing manner to the cesium used in the ion source. The nitrogen cloud strips the passing by ions by several electrons changing the charge state from negative ions to neutral and subsequently positive ions. This causes the negative ions to stop being attracted to the positive terminal voltage in the midpoint of the acceleration path and begins to repel the ions down the acceleration path. During this capture of electrons from the passing by ions a large fraction of the Ions loose more than two electrons causing them to be double or triple charged positive. With their charge state changing to a double or triple charge, the resulting energy of the Ion is increased utilizing the same low terminal voltage. The energy of the different charge state ions is calculated according to equation below.

$$E = q * LE + (1 + q) * HV$$

Additionally, this change in charge state requires careful attention in measuring the flux of the Ion beam as the change in charge state for acceleration also changes the measured current from each ion from 1 elementary charge per ion to multiple elementary charges per ion depending on the charge state used in the particular experiment. As high acceleration or deceleration of charged particles can cause harmful ionizing radiation via the emission of Bremsstrahlung, the entirety of the acceleration path is lined with lead shielding to prevent the escape of radiation.

Van-De-Graff

In order to achieve a high voltage necessary to accelerate the ions in the accelerator a Van-De-Graff generator is used. This generator can be thought of very similarly as of the once used for simple electrostatic physics experiment consisting of a charging power supply, a charge carrying belt and a high voltage terminal. The 3 MV national electrostatic follows the same principle design with a power supply depositing charge onto 2 parallel running chains that subsequently deposit charge on a high voltage terminal. The actual numerical value of the high voltage terminal is controlled by the rate at which charge is deposited onto the chains with an increasing amount of charge deposited per unit time increasing the voltage in the terminal while maintaining a constant leakage of current through the load resistors of the acceleration tube to maintain a uniform linear electric field. The voltage is further stabilized by momentarily leaking current through a corona probe from the high voltage terminal to ground. This leakage current to the corona probe is used in Van-De-Graff type accelerators to compensate for fluctuations in the deposition of charge onto the charging belt. Furthermore, the amount of leaked current is controlled via a feedback loop type control circuit that measures the momentary voltage present at the high voltage terminal and matching the suitable current bleed through the corona probe to return the terminal voltage to a desired value. In such high voltage conditions great care must be placed on the buildup and collapse of the electric field as sudden surges in the electrical field can cause sudden discharge and damage to the acceleration column. In order to prevent such discharge during normal operation, the pressure tank surrounding the Van-De-Graff generator is filled with an Sulfur Hexafluoride gas to 75 psi. This layer of Sulfur Hexafluoride gas acts as an insulation gas between the high voltage parts of the accelerator and ground. An additional purpose of this gas filling is also to cool the moving internal parts of the accelerator such as the chains and electric motors driving the charge chains. The cooling of the accelerator is accomplished via circulating the SF6 gas around the acceleration column and through a heat exchanger that is in turn cooled via pumping chilled water through it that is supplied by an external water chiller. To maintain proper purity and dryness of the SF6, the gas is additionally circulated through a pebble bed chemical drying agents to prevent the uptake and transport of moisture thorough the gas.

The high energy focusing

With the ion beam accelerated to the required energy, a main concern is to collimate the beam sufficiently to achieve a maximum amount of transmission of ions from the accelerator downstream to the target chamber. To achieve this collimation a set of two electromagnetic fields is induced perpendicular to the ion beam that compress the traversing ions to achieve a focusing effect. The required electromagnetic field is produced through the use of two electro-magnets that are mounted perpendicular to the beamline with a 90-degree offset, commonly referred to as quadrupoles. As the name suggest the use of the two electromagnets creates a set of for magnetic poles that each contribute to the collimation effect of the ion beam. In addition to the collimation of the ion beam the quadrupole serves as the main tool to alter the final focal point of the ion beam thus regulating the amount of focusing and defocusing playing a crucial role in creating a homogeneous beam spot.

The switch magnet and energy-charge separation

After the Ion beam has been accelerated to a suitable energy, it still contains a mixture of Ions that have a different charge state and consequently different energies. In order to separate the energy and charge states of the ion beam to receive a mono energetic ion beam a switch magnet is used to bend the beam trough a predetermined angle into a beamline containing a set of apertures leading up to the target chamber. As is commonly know the effect of a magnetic field on a traversing charged particle is dependent on the speed of that said particle multiplied by its charge. In the case of an Ion beam containing differently charged Ions moving at different speeds this basic law of physics can be used to create a filtration effect in which the careful choice of magnetic field inside the switch magnet will cause only the desired Ions with predetermined set of charge state and energy to pass through the aperture in the desired beamline

Figure 2.5. Image of quadrupole with its distinctive four poles used for the collimation of the ion beam downstream of the Van-DeGraaf accelerator.

with a fixed predetermined angle. This filtering effect will cause the ion beam to become mono energetic but also will reduce the ion flux as the beam will lose any ions traveling at either different speeds, mass or charge state. A detailed derivative of the mathematical equations governing this filtration is presented in appendix A.

The beam line

On its final journey from the switch magnet to the target chamber the ion beam passes through its designated beamline. Inside the beamline two sets of slits that act as apertures for the beam determine the final size of the beam spot size. The slits are adjusted in a fashion that the beam spot size exceeds the size of the sample that is to be irradiated only be a small margin of 1mm. This is done in order to minimize the loss of beam current due to the excessive spread of the ion beam. An additional feature of the beamline is a set of deflector magnets mounted around the beamline along the trajectory of the ion beam. The purpose of this deflector magnets is to bend the beam off course away from the target and back again 3 times. This bending and redirecting of the Ion beam is done in order to avoid the dragging effect the beam might have on neutral contaminants along the beamline. As the neutral particles travel at a much slower speed and charge state, they cannot keep up with sharp bending of the ion beam in the deflector magnets and is hence deflected away from the target, preventing any unnecessary contamination. Finally a faraday cup is mounted at the exit of the beamline which acts as an measuring device for the beam current. The faraday cup measures the beam current via collecting the charge of the impeding ions and routing this flow of charge via a cable to a current integrator. This current integrator very accurately measures the current created by the ion beam impeding on the faraday cup. By the relationship of elementary charge state, current, area and time one can than calculate the flux present on the faraday cup which is assumed to be the same flux as present on the sample.

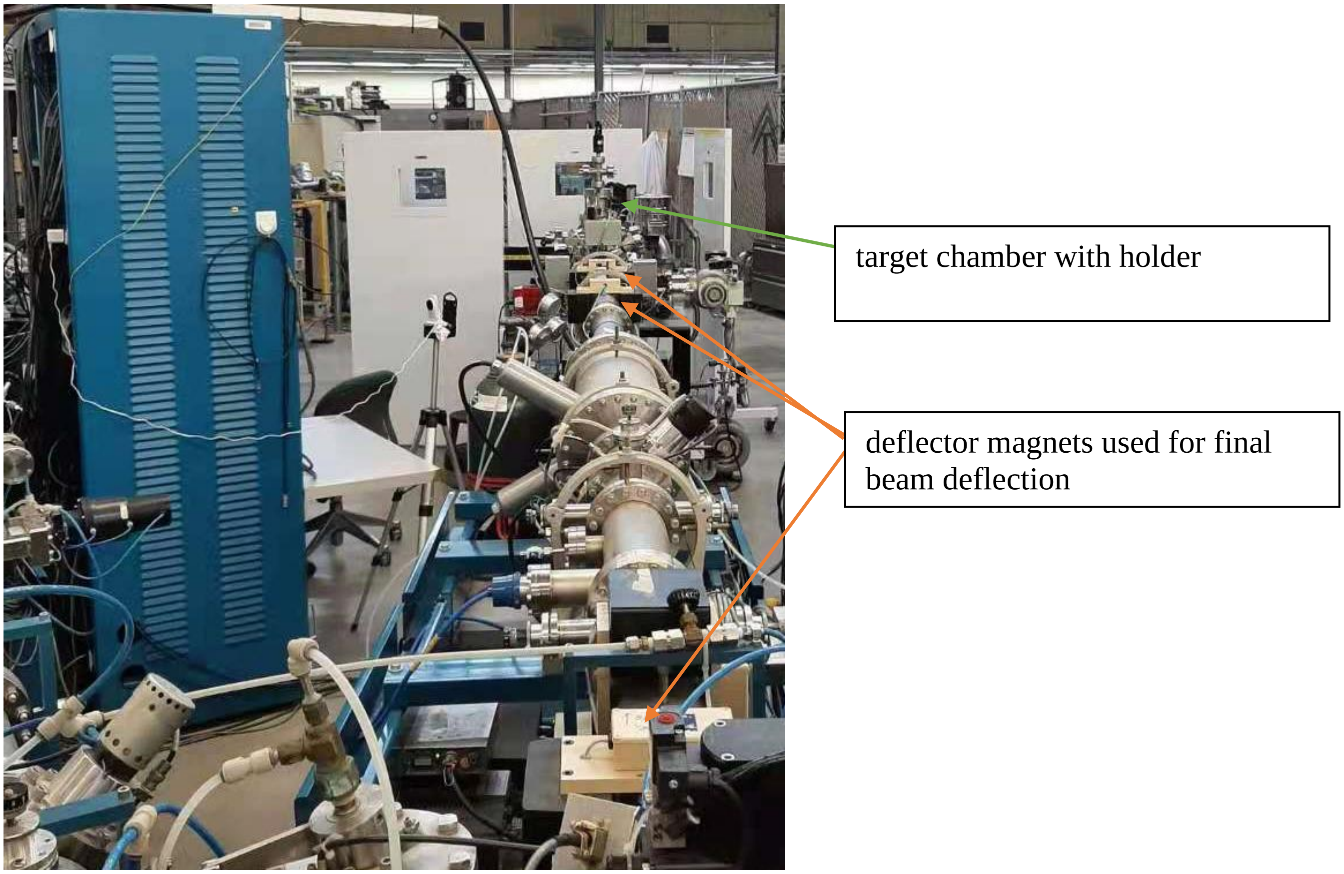

Figure 2.6. The BR 15 beamline used in the implantation of pure chromium with 5 MeV iron ions during the experiment.

The target chamber

The target chamber is the chamber in which the actual interaction between the sample and Ion beam take place. The chamber is equipped with several feed-throughs into the high vacuum system that connect the beamline, vacuum gauge as well as measuring devices such as

thermocouples and heaters. The sample is mounted inside the chamber on a movable and rotatable stage that can be heated and cooled between the temperatures of -100 C to 700 C. The stage itself is made from oxygen free copper that is heated via a 500 Watt light bulb.
The copper was chosen as the stage material as it provides the best heat conductivity and in addition to maintaining structural integrity at high temperatures. The lightbulb heats the stage via conduction and radiative heat exchange. In addition, the quartz housing of the filament around the light bulb prevents the hot filament from out-gasing into the ultra-high vacuum of the target chamber jeopardizing the experiment. The temperature of the stage is controlled via the power input of the light bulb that can be regulated via an variable power transformer. Great care must be placed on not overpowering the lightbulb as that may damage the filament. The temperature on the sample stage is measured via a thermocouple that is connected to the back side of the stage and is measured to be identical to its symmetrical front side in previous calibration runs.

The physical mounting of the sample on the stage is accomplished via ultra-high-performance silver paste. This silver paste was chosen as it can withstand high temperatures without losing its adhesive properties as well as maintaining physical integrity and allowing for thermal and electrical conductivity. The electrical conductivity of the sample to ground must be maintained at all times as a charging of the sample would cause sudden discharges over time which would cause arcing between the sample nearest point of ground potential which could potentially destroy the sample.

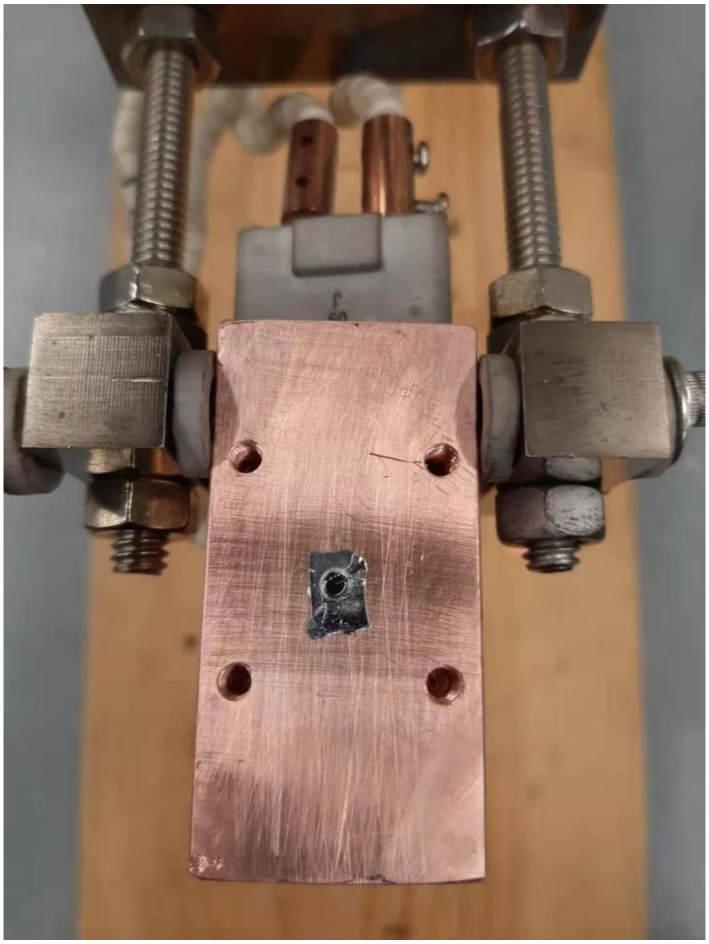

Figure 2.7. Sample stage machined from oxygen free copper, hollow drilled and installed on ceramic insulators on high vacuum manipulator. The heating is achieved via a 500 watt halogen lightbulb mounted on the inside of the stage and the temperature is measured via a K-type thermocouple mounted on the back face of the stage.

2.2.3 The high vacuum and interlock system

One major aspect of ensuring the proper functionality of the particle accelerator and the accuracy of the experiment is the necessity to maintain ultra-high vacuum conditions throughout the system. The first reason for maintaining this ultra-high vacuum conditions is due to the fact that the ion beam traveling through the internals of the particle accelerator cannot be protruded or disturbed by any kind of matter in its way is this collision would cause a declaration of the beam and loss of beam current. Another important aspect is the oxidation prevention and inertness of the interaction between the impeding ion and the chromium samples.

Chromium is prone to oxidation which can cause extensive surface layers of chromium oxides and affect measurements during the experiments. The ultra-high vacuum conditions prevent the exposure of the chromium to any oxygen or contaminants during the high temperature phase of the experiment preserving the chemical composition of the substrate. In order to achieve vacuums up to a level of $1 * 10^{-8}$ tor a large number of Turbo-molecular pumps and dry roughing scroll pumps are used. The level of vacuum inside the system requires the two pumps to act in series in order to achieve sufficient pressure gradient to achieve the desired vacuums. The Turbo-molecular pump creates the first pumping step between the accelerator and environment spinning at a frequency of 833 hz creating a pressure gradient from $1 * 10^{-8}$ tor on its intake side to a pressure of $50 * 10^{-3}$ tor on its exhaust side. The exhaust of the turbo molecular pump is than in turn sucked in by a dry scroll pump and compressed to atmospheric pressure and exhausted to the surrounding. Due to the nature of the high operational speed of the turbo molecular pumps it can never be operated above a pressure of $50 * 10^{-3}$ tor as this would cause catastrophic damage to the internals of the pump. In order to prevent damage to personal or the equipment in cases of unforeseen operational conditions such as power outages or loss of vacuum situations the accelerator is equipped with a series of safety interlocks.

These interlocks activate if any vacuum gauge inside the high vacuum part of the accelerator registers a pressure above $1 * 10^{-6}$ tor or in case of sudden power surges or outages. To protect the personal from electrocution the accelerator is furthermore equipped with interlocks on its maintenance access points which will cut power to the accelerator when opened during normal operation.

2.2.4 The irradiation process

The Ion irradiation of the samples was performed at the Texas A&M Ion beam laboratory and materials testing facility via the use of the 3 MV NEC Pelletron particle accelerator. The first step in conducting the ion irradiation is the preparation of the machine and pre-experiment checks which include but are not limited to checking the insulation gas pressure, stripper gas pressure and vacuum pressure in all subsections described in the outline of the experimental equipment. As a first step the SNICS ion source is equipped with a pure Iron cathode with a purity of 99.5% by screwing the new cathode on the cathode holder. Subsequently the ionizer filament inside the SNICS source is heated to a temperature of over 1300 C to start the ionization of Cesium that is being fed into the Ion source. The Cesium flow is regulated via adjusting the oven temperature which slowly evaporates the Cesium into the vacuum of the ion source and maintains the flux of ionized Cesium. With a sufficient flux of Cesium established the cathode voltage is increased which draws the Cesium Ions onto the cathode which will commence in sputtering Iron ions. These sputtered ions undergoing electronic charge exchange with the Cesium present in its vicinity are extracted from the source head via a 16 KV bias applied across the SNICS ion source and further focusing is achieved via a separate 17 KV focusing bias.

With the Ion beam established the first mass energy separation is taking place in the low energy magnet and the ion beam flux is optimized at the low energy faraday cup via the tuning of the extraction bias, focusing voltage, cathode voltage and magnetic field of the injector magnet. When optimized, the beam is released further down the beamline into the Pelletron where the ions are accelerated through the terminal voltage and change their charge state while passing through a low density cloud of stripping gas which gives the acceleration a tandem effect. This tandem effect is due to the fact that the negative incoming ion sees the positive acceleration potential twice. Once on its way to the center of the acceleration column as a negative ion and then after passing through the stripping as a positive ion again. The stripping gas used is ultra-high purity nitrogen which is recirculated via means of turbo molecular pump inside the acceleration column.

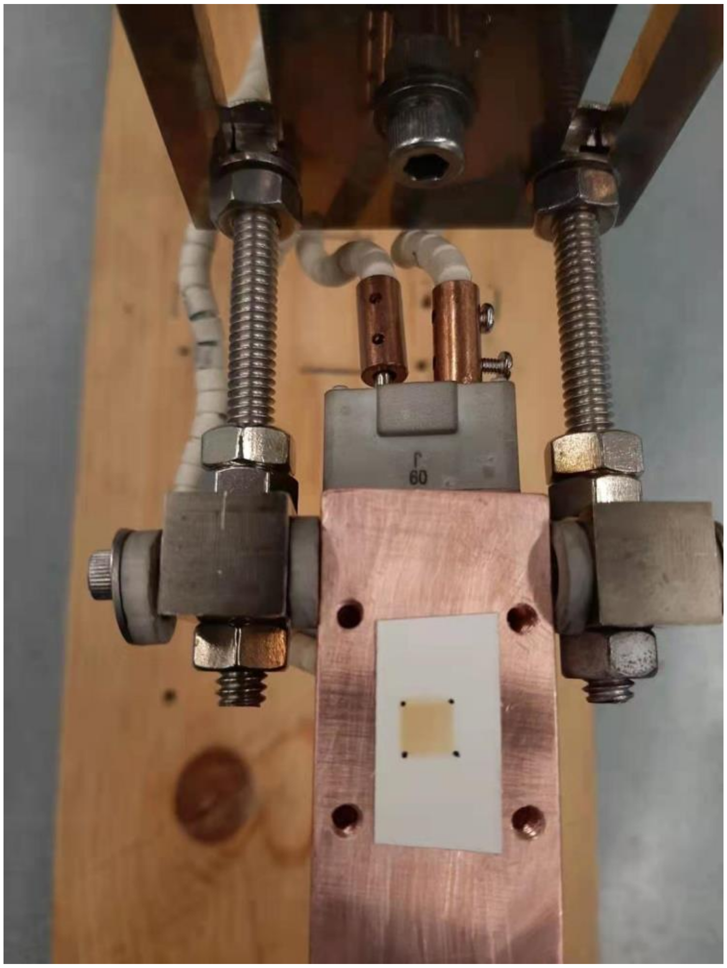

Figure 2.8. Paper burn spot on sample stage marking the dimensions and location of the ion beam used for flux calculation and mounting respectively.

The disadvantage of this tandem design is that only a limited number of ions actually undergo the chemical charge exchange with the stripper gas inside the High voltage column and hence about 60% of the initial ion beam are lost after the mass energy separation in the switch magnet. Furthermore, great care has to be taken not to inject to much stripping gas into the acceleration column because increasing the amount of gas inside the column has a diminishing return on transmission efficiency. This is because the increase in gas flow increases the density of the stripping gas cloud and increases collision between Ions and stripping gas which can decrease transmission in extreme cases.

After exiting the high voltage terminal, the ion beam is again filtered for mass charge ratio in the switch magnet as outlined in the equipment section and then guided into the proper beamline. Inside the beamline two sets of apertures determine the final dimensions of the beam spot. A piece of quartz mounted on a manipulator inside the beamline is used to visualize the beam spot in front of the target chamber. The ion beam flux on the quartz glass creates a distinctive blue glow which increases and decreases according to the intensity of the ion beam. The image of the quartz scintillating is transmitted to the control station via a camara and displayed on a cathode ray television set. The feedback from the illumination of the quartz is used to defocus the beam across the entire beam spot area, which ensures a uniform flux distribution on the sample area.

After the defocusing has taken place a set of 3 deflection magnets mounted along the beamline is used to deflect the ion beam 3 times via steering it of target and back again. This deflection of the ion beam filters out any neutral components that the ion beam is dragging along the beamline via columbic drag and increases the purity of the beam. In order to mount the sample in the correct spot on the sample manipulator and to further verify the uniformity of the beam, a blank piece of paper is mounted on the sample stage which is burned for a few seconds via the bombardment of the ion beam. The burned spot on the paper depicts the actual area used for the flux and fluence calculation of the irradiation dose and aids as a reference when mounting the sample.

The actual mounting of the sample is conducted via pasting the sample onto the stage with high performance silver paste. The silver paste ensures that the heat conduction between the stage and sample is high and the inert nature of the silver prevents the accumulation of contaminants. After the mounting of the sample the entire manipulator is placed inside the target chamber which is subsequently pump down to ultra-high vacuum. Once sufficient vacuum is reached (below 9.9E-8torr) the sample stage is heated to the experiment temperature and the cold trap is filled with liquid nitrogen to condense any remaining impurities inside the vacuum. With the sample at temperature and under vacuum, the irradiation commences and all parameters are logged and monitored constantly. Once the desired dose for the particular sample has been implanted, the vacuum chamber is isolated from the rest of the accelerator system and the sample is cooled down in ultra-high vacuum to maintain a clean environment. After reaching room temperature the sample is extracted from the stage and stored inside a desiccator box until the focused Ion beam analysis is conducted.

2.3 Sample characterization

After the irradiation has been performed no changes to the sample are visible via the naked eye and sophisticated microscopy methods must be applied in order to visualize the nm sized defects introduced into the target Cr.

2.3.1 Scanning electron microscope

As a first step a suitable grain has to be chosen which will used to manufacture a FIB lift out. The grain chosen for the lift out must sufficiently large to accommodate the entire lift out as well as have good surface finish with no scratches or imperfections to ensure that no work hardening has occurred before the irradiation that might severely skew the development of defects inside the sample.

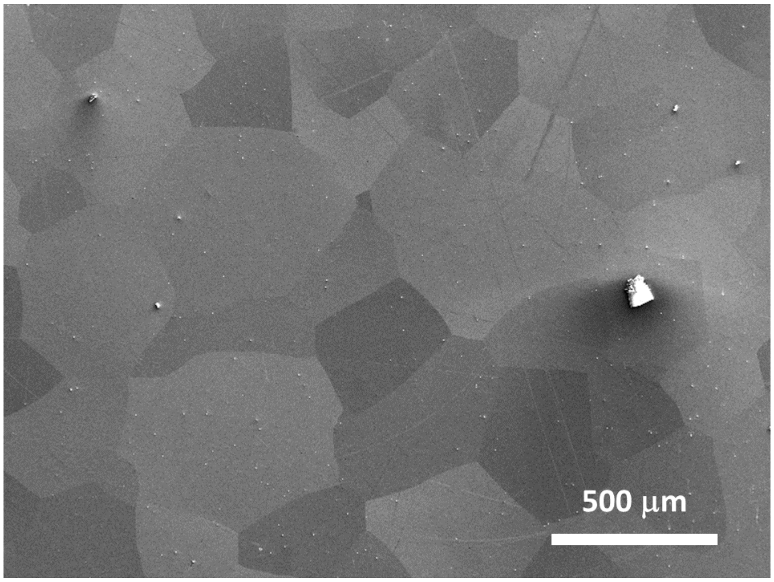

Figure 2.9. SEM image of chromium surface after irradiation and prior to manufacturing of a FIB lift out.

2.3.2 Focused ion beam analysis

In order to prepare the sample for microscopy and to obtain a thin enough sample for the electrons of the transmission electron microscope to pass through the sample, a micron sized lamella has to machined out of each sample using focused Ion beam analysis. The first step of the FIB is to load the sample into the FIB chamber and to pump the chamber down to vacuum. Once at vacuum, the electron beam for the scanning electron microscope can be powered up and a suitable grain is chosen which will be used to mill out the lamella. The main criteria for a suitable gain is that the size is sufficiently large so that the FIB liftout is taken from a singular grain.With a suitable grain selected, platinum is deposited on the surface of the grain in order tor protect the surface from damage of the FIB milling process. The thickness of the platinum layer is usually around 2µm. With the platinum deposited, the trenching can commence and the FIB lamella is starting to take shape. It is important to pay particular attention to the orientation of the scanning field of the gallium beam during the FIB process as the orientation will determine the smoothness and step height of the lamella and the trench.

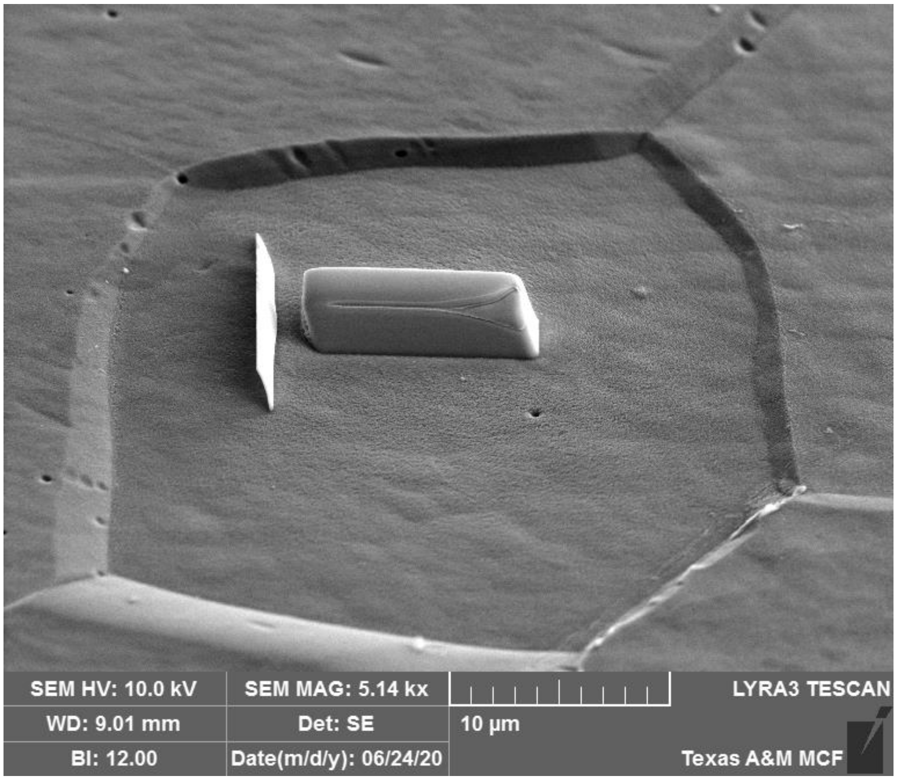

Figure 2.10. Image of selected Grain used for lift-out and platinum deposition on grain creating protective layer during milling process.

Once sufficiently large trenches have been milled out around the perimeter of the lift out, the micro manipulator of the FERA system can be brought into proximity of the lamella, and the tip of the micro manipulator is attached to the milled out lamella via the deposition of platinum. With the lamella secured on the micro manipulator the last remaining connection between the lamella and the bulk material are served and the micro manipulator is slowly lifted away from the bulk sample. With the lamella freed from the bulk, the remaining sample is moved away and the electron microscope and the lamella are aligned to commence the thinning of the sample. With a limited penetration depth of the scanning electron microscope, the lamella’s thickness cannot exceed 150 nm as this would negatively impair the resolution of the microscope due to excessive attenuation of the electrons in the lamella. The thinning of the sample is accomplished

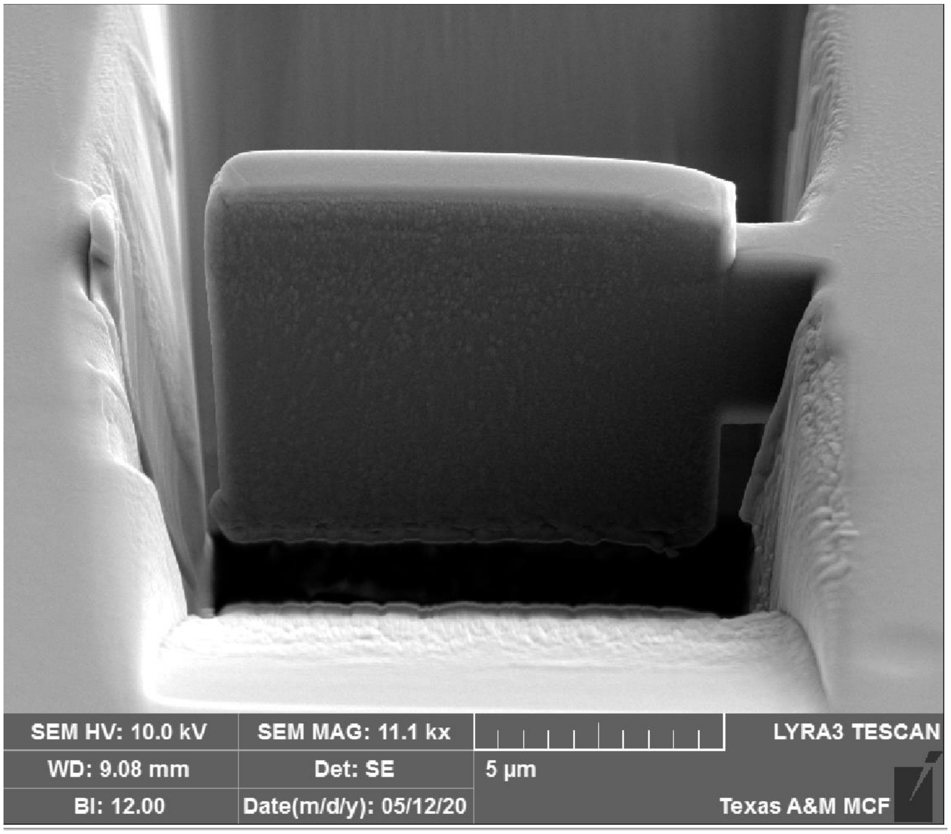

Figure 2.11. Lamella on surface of Cr sample after trenching and before attachment to micro manipulator ready for thinning.

via carefully rotating the sample around its center axis a few degrees away from its perpendicular orientation and using the focused gallium beam to etch away a thin layer one at a time and measuring the thickness of the remaining sample. This careful method of thinning the sample via tacking of thin slices one at a time is necessary to create a good unperturbed surface finish of the ion implanted region. If the thinning was to be done perpendicular to the ion implanted direction, the additional damage from the FIB process would skew the results of the subsequent analysis. With the sample thinned to proper specifications, the lamella is attached to a copper lamella holder via loading the holder into the vacuum chamber of the FIB and moving the micro manipulator to the desired location on the lamella holder. Once close enough, the remaining gap between the lamella and lamella holder is closed via the deposition of platinum which will act as an adhesive between the holder and sample.

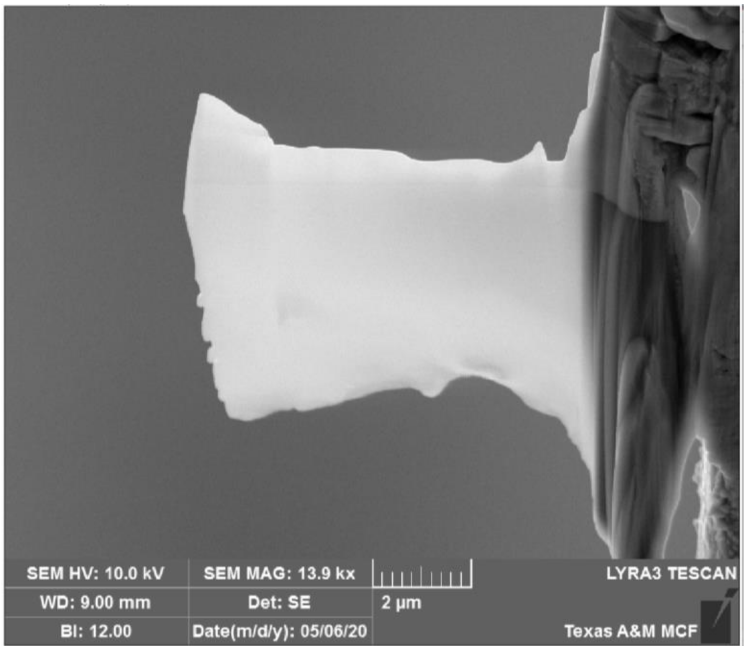

Figure 2.12. Scanning electron microscope image of Lamella attached to lamella holder inside the FIB chamber.

Commencing successful attachment of the sample, the micro manipulator tip cut of the sample via bombardment of gallium ions and resharpened with the same beam to ensure a sharp defined tip for the next user. In order to retrieve the lamella holder and sample from the LYRA, the manipulator and stage are brought into the home position and the electron beam as well as the ion beams are powered off and the chamber is isolated and vented. The stages with the sample holder and sample can now be retrieved from the vacuum chamber and are stored in a decicator until the next step of Analysis. Great care must be taken though when handling the FIB lamella during transportation as it is very sensitive and the attached sample can easily brake requiring a repetition of the FIB milling process.

2.3.3 Transmission electron microscopy

A key challenge and requirement in the analysis of the defects is the challenge of visualizing the defects inside the microstructure of ion irradiated samples. With defect sizes below 10nm conventional optical microscopes are incapable of displaying changes in the microstructure of samples. As a solution highly energetic electrons are used to traverse a thin slice of the ion implanted sample.

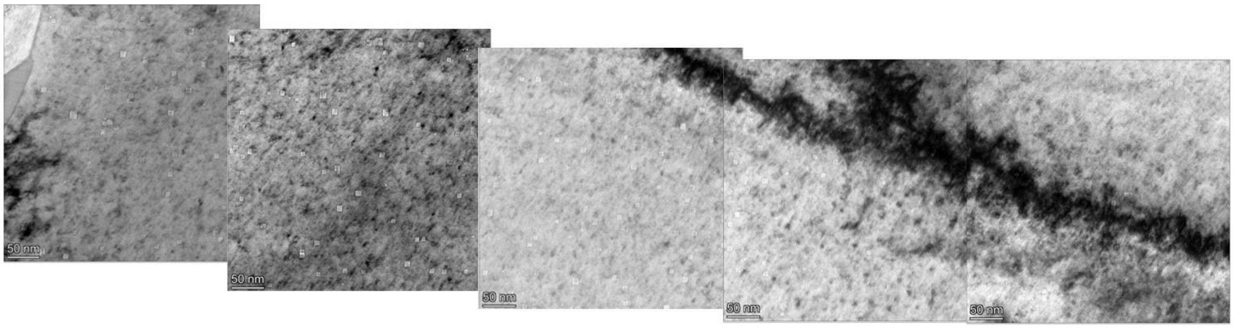

Figure 2.13. Image of pure chromium irradiated at 650 °C with 5 MeV iron ions to a dose of 15 DPA at a rate $3.5 * 10^{-5} \frac{\mathrm{DPA}}{\mathrm{s}}$

During their path through the sample electrons are attenuated at discontinuities inside the sample's crystal structure creating a gradient in electron flux. This gradients in flux create a contrasted image of the sample on a fluorescent screen which the electrons hit after exiting the sample. Due to the charged nature of the electron beam, it can be highly focused via means of electromagnetic fields. This focusing allows for a very high flux of electrons to pass through the small FIB lamella.

The magnification effect of the image on the fluorescent screen is achieved because the stream of electrons will strongly diverge as it moves away from the focal point of the electron beam which passes through the sample. As this large flux of electrons creates a substantial heat input into the sample, cooling is achieved via a copper cold sink that in turn is cooled via liquid nitrogen.

Images of the sample are taken at different magnifications varying from a factor of 9000 to a factor of 45000. The images are taken across the entire sample width and depth in order to encompass all microstructural changes within the sample. An important feature of the high magnification images is that they are taken in regular increments and at constant magnification. This method allows the images to be spliced together at a later point to create a constant 'map' of the entire sample with sufficient magnification to recognize the individual defects occurring within the sample's microstructure. The splicing of the maps is achieved via recognition of distinct features on two adjacent micrographs and subsequent matching of overlap. During this splicing it is important to conserve the orientation of the sample to ensure continuity across the entire damage region and accurate orientation of the sample perpendicular to the penetrating ion beam.

2.3.4 Void analysis using Image J

With a complete high magnification map of images along the entire damage region, the quantification of the individual types of defect can commence.

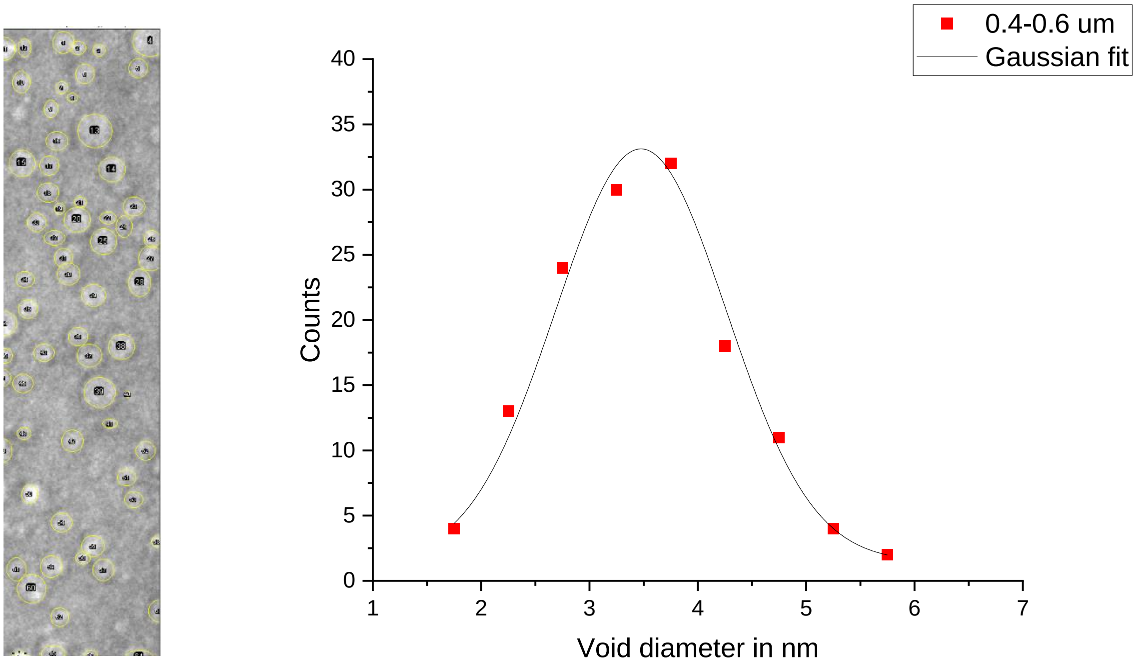

Figure 2.14. Image of a 200nm x 50nm increment from sample L450 analyzed in Image J software and resulting size distribution of voids in said depth increment.

The sample depth is first discretized into increments of 200 nm which will serve as bins which will contain the specific information about defect size, number, and type. This 200 nm deep bins are than widened to a width of 50 nm giving an area of 10000 nm^2 which serves as a representative sample area for the specific depth bin.

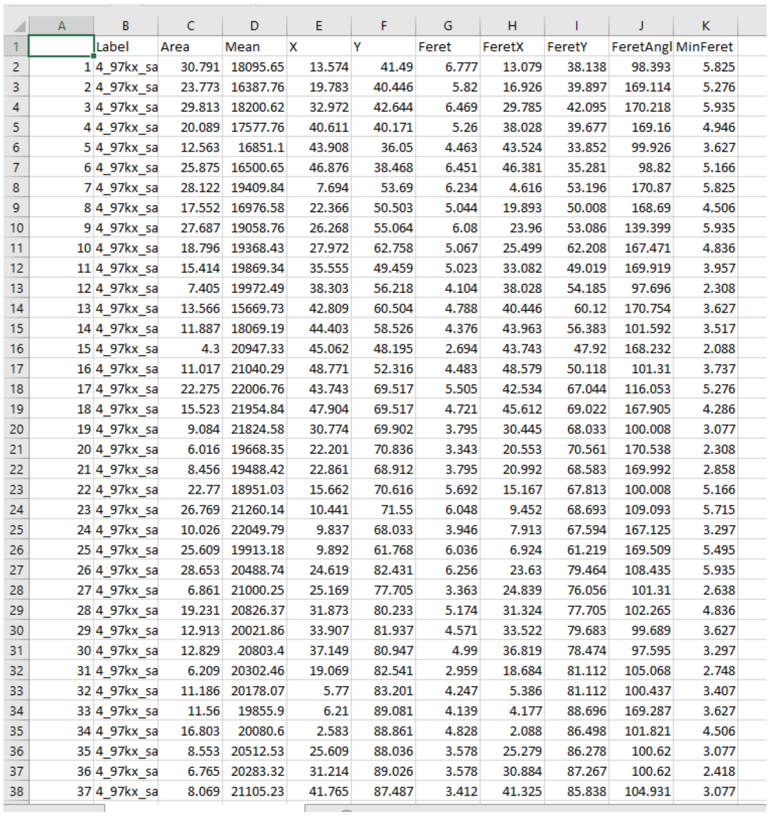

	A	B	C	D	E	F	G	H	I	J	K
1		Label	Area	Mean	X	Y	Feret	FeretX	FeretY	FeretAngl	MinFeret
2	1	4_97kx_sa	30.791	18095.65	13.574	41.49	6.777	13.079	38.138	98.393	5.825
3	2	4_97kx_sa	23.773	16387.76	19.783	40.446	5.82	16.926	39.897	169.114	5.276
4	3	4_97kx_sa	29.813	18200.62	32.972	42.644	6.469	29.785	42.095	170.218	5.935
5	4	4_97kx_sa	20.089	17577.76	40.611	40.171	5.26	38.028	39.677	169.16	4.946
6	5	4_97kx_sa	12.563	16851.1	43.908	36.05	4.463	43.524	33.852	99.926	3.627
7	6	4_97kx_sa	25.875	16500.65	46.876	38.468	6.451	46.381	35.281	98.82	5.166
8	7	4_97kx_sa	28.122	19409.84	7.694	53.69	6.234	4.616	53.196	170.87	5.825
9	8	4_97kx_sa	17.552	16976.58	22.366	50.503	5.044	19.893	50.008	168.69	4.506
10	9	4_97kx_sa	27.687	19058.76	26.268	55.064	6.08	23.96	53.086	139.399	5.935
11	10	4_97kx_sa	18.796	19368.43	27.972	62.758	5.067	25.499	62.208	167.471	4.836
12	11	4_97kx_sa	15.414	19869.34	35.555	49.459	5.023	33.082	49.019	169.919	3.957
13	12	4_97kx_sa	7.405	19972.49	38.303	56.218	4.104	38.028	54.185	97.696	2.308
14	13	4_97kx_sa	13.566	15669.73	42.809	60.504	4.788	40.446	60.12	170.754	3.627
15	14	4_97kx_sa	11.887	18069.19	44.403	58.526	4.376	43.963	56.383	101.592	3.517
16	15	4_97kx_sa	4.3	20947.33	45.062	48.195	2.694	43.743	47.92	168.232	2.088
17	16	4_97kx_sa	11.017	21040.29	48.771	52.316	4.483	48.579	50.118	101.31	3.737
18	17	4_97kx_sa	22.275	22006.76	43.743	69.517	5.505	42.534	67.044	116.053	5.276
19	18	4_97kx_sa	15.523	21954.84	47.904	69.517	4.721	45.612	69.022	167.905	4.286
20	19	4_97kx_sa	9.084	21824.58	30.774	69.902	3.795	30.445	68.033	100.008	3.077
21	20	4_97kx_sa	6.016	19668.35	22.201	70.836	3.343	20.553	70.561	170.538	2.308
22	21	4_97kx_sa	8.456	19488.42	22.861	68.912	3.795	20.992	68.583	169.992	2.858
23	22	4_97kx_sa	22.77	18951.03	15.662	70.616	5.692	15.167	67.813	100.008	5.166
24	23	4_97kx_sa	26.769	21260.14	10.441	71.55	6.048	9.452	68.693	109.093	5.715
25	24	4_97kx_sa	10.026	22049.79	9.837	68.033	3.946	7.913	67.594	167.125	3.297
26	25	4_97kx_sa	25.609	19913.18	9.892	61.768	6.036	6.924	61.219	169.509	5.495
27	26	4_97kx_sa	28.653	20488.74	24.619	82.431	6.256	23.63	79.464	108.435	5.935
28	27	4_97kx_sa	6.861	21000.25	25.169	77.705	3.363	24.839	76.056	101.31	2.638
29	28	4_97kx_sa	19.231	20826.37	31.873	80.233	5.174	31.324	77.705	102.265	4.836
30	29	4_97kx_sa	12.913	20021.86	33.907	81.937	4.571	33.522	79.683	99.689	3.627
31	30	4_97kx_sa	12.829	20803.4	37.149	80.947	4.99	36.819	78.474	97.595	3.297
32	31	4_97kx_sa	6.209	20302.46	19.069	82.541	2.959	18.684	81.112	105.068	2.748
33	32	4_97kx_sa	11.186	20178.07	5.77	83.201	4.247	5.386	81.112	100.437	3.407
34	33	4_97kx_sa	11.56	19855.9	6.21	89.081	4.139	4.177	88.696	169.287	3.627
35	34	4_97kx_sa	16.803	20080.6	2.583	88.861	4.828	2.088	86.498	101.821	4.506
36	35	4_97kx_sa	8.553	20512.53	25.609	88.036	3.578	25.279	86.278	100.62	3.077
37	36	4_97kx_sa	6.765	20283.32	31.214	89.026	3.578	30.884	87.267	100.62	2.418
38	37	4_97kx_sa	8.069	21105.23	41.765	87.487	3.412	41.325	85.838	104.931	3.077

Table 2.1. Ledger containing the number, label, area and dimension of each void counted in a TEM cross section micrograph of dimension 200 nm x 50nm discretized by sample depth.

The analysis of each individual bin is done via the use of ImageJ image processing software. To convert the two-dimensional measurements of the cross- section micrographs to 3-dimensional information, the assumption is made that the shape of void is either spherical or cuboid. Image J is used to mark each individual feature within each bin and tally the position, size and dimension of each feature and keeping track of this information in depth specific ledgers. Said ledgers are subsequently saved under individual file names and stored for further processing.

2.3.5 Calculation and quantification of void swelling

The information of each ledger containing raw measurements is processed in origin to extract all necessary information from the measurements and to convert the measured dimensions to void swelling, void size, and void density. For a specimen of initial unit volume, where the volume is provided by the 10000 nm^2 bin area and thickness from EELS meassurment , the fraction of volume occupied by voids, $V_{void}\%,$ is different from void swelling percentage, $swelling\ \%$. Note that $swelling\ \%$ is the extra volume created due to swelling expansion of the sample which is the dark layer grown on the top of the original volume. If the added layer is void-free, its volume must equal $V_{void}\%$. If the added layer develops the same swelling as the original bulk, the newly added volume is larger than $V_{void}\%$. After swelling, the original unit volume contains only $(1 - V_{void}\%)$ of original atoms. In other words, $(1 - V_{void}\%)$ of total atoms in the original cell now occupy an unit volume. With $1/(1 - V_{void}\%)$ as a volume conversation rate, the newly added volume by the missing atoms in voids is

$$Swelling\% = V_{void}\% \times \frac{1}{1 - V_{void}\%}$$

Or

$$Swelling\% = V_{void} \times \frac{1}{V - V_{void}}$$

where V is the volume of the initial cell.

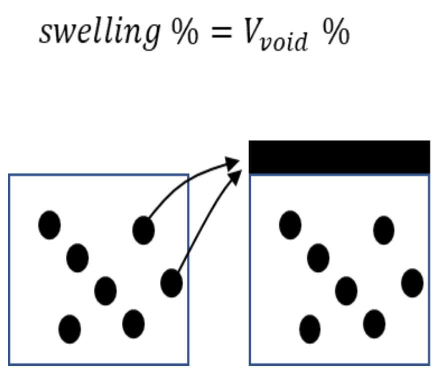

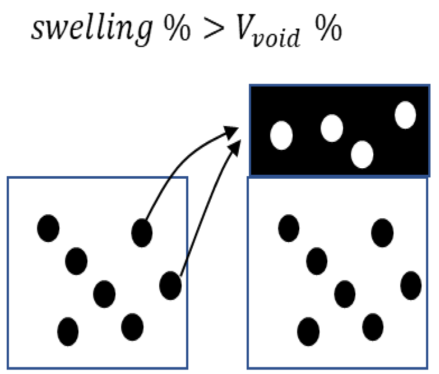

Assuming the diameter of the voids to be the average of the minimum and maximum fertet obtained by each ledger the swelling can now be obtained via the talling and summation of each individual void and the addition of all of them to obtain the void volume fraction, using $V_{void}\% = (\sum \frac{1}{3} 4\pi {r_i}^3)$/V, for spherical voids, where i is the void radius and V is the cell volume. It is importatnt to point out that $V = t \times w \times l$, where t, w, l, are thickness, length and width of specimen. For the summation method and using transmission electron microscopy characterization, the error in measuring r_i, w, and l, are almost zero. The major uncertainty is the accuracy in measuring specimen thickness.

$$\sigma_{V_{void}\%}/V_{void}\% = \sigma_t/\bar{t}$$

Thus, processing and repeating this caclulation for each individual depth increment subsequently yields a detailed analysis regarding void swelling utilizing the discretization of the sample depth in 200 nm increments, has the additional advantage that the swelling of the sample can be displayed as a damage dependent function because the damage increases with increasing sample depth. This detailed analysis and discretization is necessary as it allows for exclusion of the data effect by ion specific damage effects such as the injected interstitial and surface effect which will greatly skew the data displayed by each sample when compared to neutron data. Furthermore it enables the analysis of and comparison of effects attributed to void nucleation and void growth that can only be observed through such thorough investigation and detailed analysis.

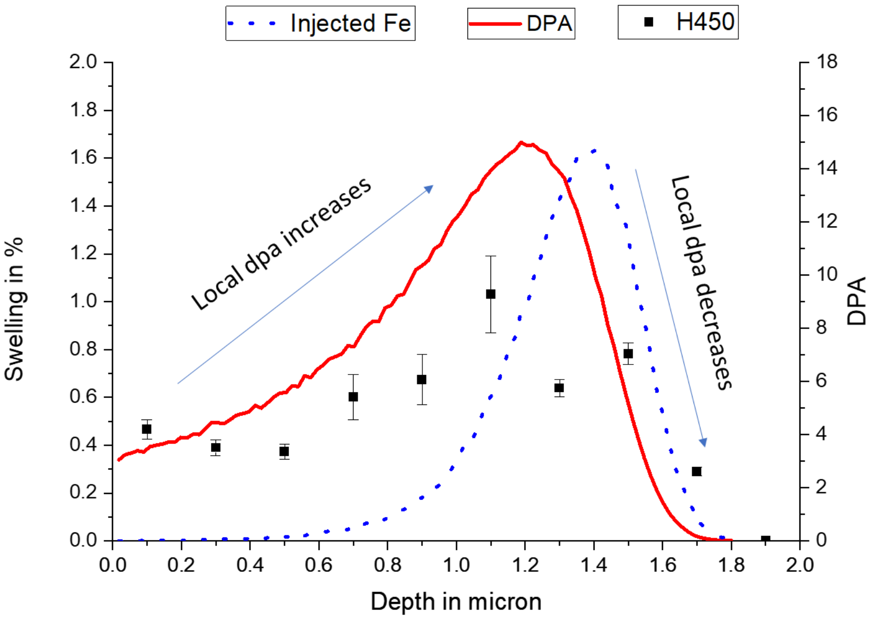

Figure 2.15. Damage and implantation profile simulated in SRIM for 5 MeV Fe ions in Cr substrate overlayed with measured swelling for a sample irradiated at same conditions at a temperature of 450 °C and a damage rate of $3.5 * 10^{-3} \frac{DPA}{s}$.

3. DOSE AND TEMPERATURE DEPENDENT STUDY[*]

3.1 Introduction

As detailed in the above general introduction, the 2011 loss of coolant accident in the Fukushima Daichi accident, painfully highlighted the shortcomings of current light water reactor designs with their Zircalloy based fuel claddings. During the extensive heating of the fuel element in loss of coolant accidents the Zirconium inside the Zircalloy transforms into β-Zirconium which is highly susceptible to oxidation and reaction in a violent exothermic hydrolysis reaction with the remaining moisture inside the reactor. As a result, and as experienced during the Fukushima accident, the fuel cladding loses its integrity allowing for an exposure of the nuclear fuel contained leading to catastrophic consequences for the environment. With said accident in mind, a call for accident tolerant fuels has been introduced and among one of the most viable solutions for the improvement of accident tolerance of nuclear fuel pins are coatings that prevent above explained chain of events during loss of coolant accidents.

Among the prime contenders for coatings of accident tolerant fuels is pure chromium. Chromium in its metallic form has the advantage of being highly corrosion and wear resistant due to its high hardness and ability to form passivated oxide layers. Many industrial applications have been established for the formation of thin chromium layers on different surfaces such as cold spraying which shows remarkable surface adhesion, galvanic deposition and laser deposition. [1-5]

---

[*] Part of the data reported in this chapter is reprinted or modified with permission from "Irradiation-induced swelling of pure chromium with 5 MeV Fe ions in the temperature range 450–650 °C" by EkaterinaRyabikovskaya[a]AaronFrench[a]AdamGabriel[a]HyosimKim[b]TianyaoWang[a]KoroushShirvan[c]Frank A.Garner[a]LinShao[a], Year. *Journal of Nuclear Materials*, Volume Number 543, Copyright 2021, by Elsevier B.V.

In addition chromium has a distinctive advantage in that it does not from any brittle interfaces that might cause delamination such as MAX-phase or FeCrAl coatings on Zircalloy-4 [6, 7]. Regardless of the many advantages chromium offers on paper, a major challenge remains in that there is not much testing data on pure chromium available to establishing an experimental proof of performance on chromium in a radiation environment.

The current work is aiming to remedy the lack of knowledge of the radiation stability of pure chromium coatings via the use of heavy ion irradiation. Heavy Ion irradiation has been established as a powerful tool to surrogate the void swelling and radiation stability behavior of nuclear materials in a reasonable short time and cost-effective manner. A series of heavy Ion irradiation was conducted using 5 MeV Iron ions irradiating chromium at temperatures between 450°C to 650°C to a peak damage of 50 DPA to establish it's peak swelling temperature. Subsequently more damage was added to the specimen experiencing the peak swelling temperature to find a correlation between the ion-dose and swelling behavior of pure chromium.

3.2 Experimental procedure

The substrate Chromium was purchased from American Elements Inc. with a purity of over 99%. In order to ensure uniform height and adequate surface finish, the chromium platelets were initially polished with SiC sand paper and subsequently electropolished using a Tenupol 5 twin jet electro-polisher. The acid-solution deemed the most appropriate for polishing was 5% perchloric acid mixed with 95% methanol. In order to maintain ideal etching conditions and to prevent oxidation of the solution a temperature of -20 ºC was maintained via means of external cooling. The duration of etching for each sample was kept at ~20 seconds with a constant differential voltage of +20 V. After polishing, remining acid was removed and the substrate was sprayed down with methanol to clean off residual acid and stored in a desiccator to avoid moisture contamination.

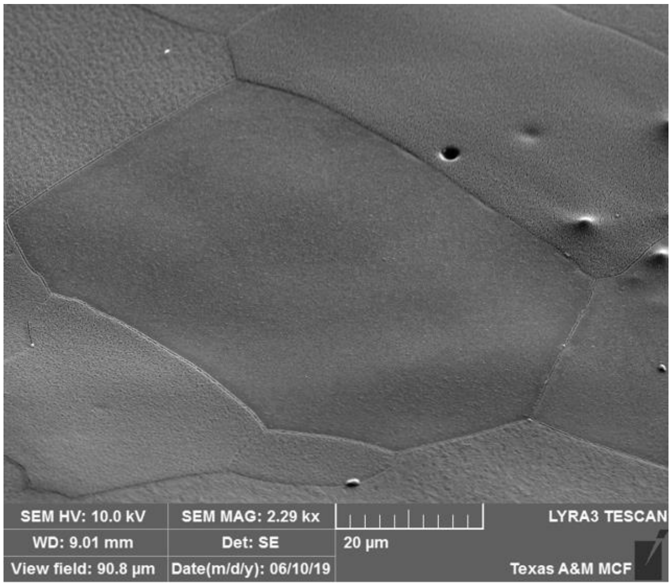

Figure 3.1 SEM image of an exemplary chromium grain used for analysis. (reprinted with permission from) [23]*

To maintain a low thermal gradient between the sample and stage during the high temperature irradiation each sample was kept below a thickness of 1mm, which allows for a deviation of less <2°C including beam heating and black body radiation. Due to the physical limitation of the SNICS ion source used in the series of experiment and the high oxidation affinity of the chromium, 5 MeV iron ions in a static defocused beam were chosen to irradiate all samples. The vacuum in the target chamber was maintained below 6×10^{-8} torr via the use of turbo molecular pumps and a copper cold trap filled with liquid nitrogen. In addition, the beam was deflected through 3 deflection magnets during its final trajectory along the beamline to clean the beam of any colombig drag O,C,N experienced in the ultra-high vacuum system [8,9].

The first part of the experiment consisting of establishing a temperature dependence of void swelling in chromium, established via a set of 5 irradiations conducted between 450°C and 650°C in 50ºC in increments, to a damage level of 50 dpa. With the maximum void-swelling temperature established at 550°C, further damage was added to said sample to a total of 100 dpa and 150dpa with the sample analysis conducted before the addition of each compounding damage. The Stopping and Range of Ions in Matter (SRIM) code was used for damage calculation [10]. The Kinchin-Pease mode with a Cr displacement energy of 40 eV was used in the simmulation. [11].

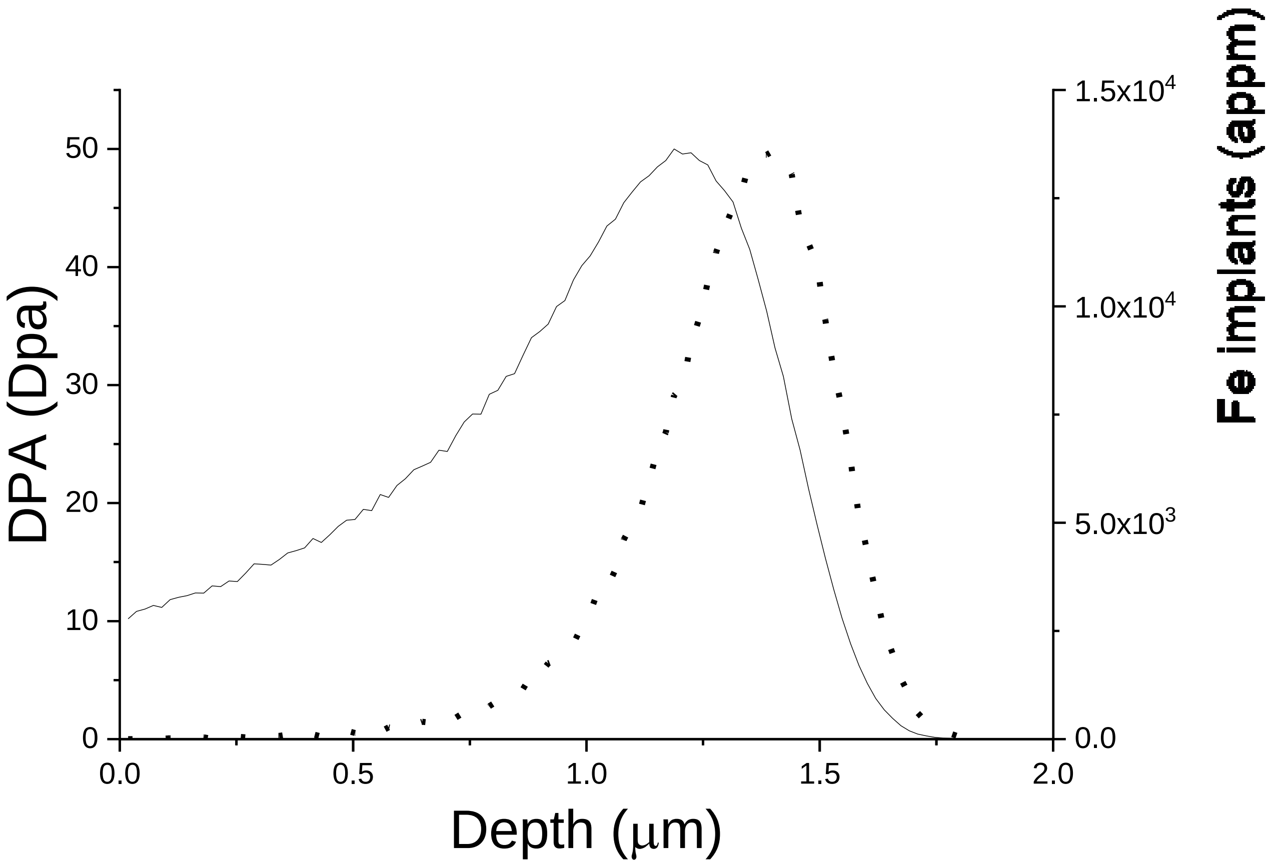

Figure 3.2. Damage distributions of 5 MeV Iron ions injected into pure chromium substrate with respective injected ion distribution (derived via usage of SRIM code)

Transmission Electron microscopy on a FEI Tecnai F20 ST was used to characterize the microstructural changes of the samples. The samples for TEM were manufactured using a Tescan LYRA-3 Model GMH Focused Ion Beam Microscope and measured using a standard Electron Energy loss spectroscopy (EELS).

As can be seen in Figure 2 peak damage is achieved at a depth of 1.2 µm, maximum implantation depth of ions is at 1.5µm and the end of the ion range is seen at about 1.8 µm. Since this experiment uses ions which differentiate from the bulk material, special attention must be paid which depth is used during the analysis process as the implanted Iron can cause a chemical change of the substrate especially during the high dpa implantation which create up to 4% of peak iron concentration at a 150 dpa peak damage. Furthermore, special care must be taken not to use the near surface region of the sample as it can act as an infinite defect sink. This effect is ion specific and must be disregarded when the results are used for evaluation and surrogating the performance of chromium in a neutron environment as encountered in a nuclear reactor.

3.3 Summery of Experimental Results

3.3.1 Peak swelling temperature

Figure 3a shows a sample of pure chromium irradiated to a damage level of 50 peak dpa at a substrate temperature of 550 °C. A damage and implantation curve simulated by SRIM was overlayed over the implanted region of the sample. Several occurrences in the sample can be observed that are of particular interest. Firstly, the void denuded zone which is a typical feature of heavy ion irradiation such as Fe irradiation near the surface is almost nonexistent. In most Fe self-ion irradiations this void denuded zone extends up to 200 nm into the sample bulk. [12] Secondly it seems that the injected Fe at the peak implantation region does not cause a suppression of the void nucleation is it is the case in Fe self-ion irradiation. [6, 13-18] Lastly a common sight between the chromium and most other metallic system depletion of defects can be seen near the grain boundary which is to be expected.

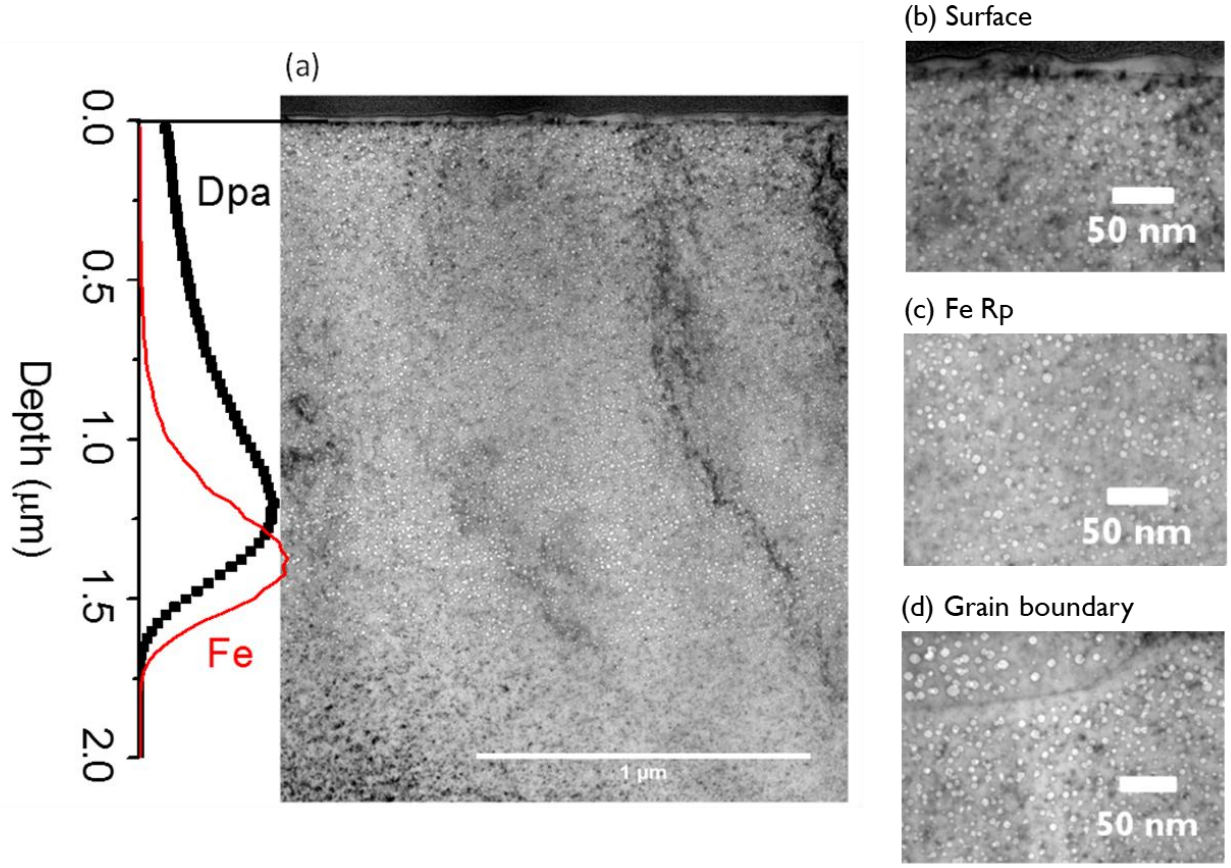

Figure 3.3 (a) TEM image of 5 MeV Fe irradiated chromium substrate to a damage level of 50 dpa at maximum swelling temperature . The images a),b) and c) correspond to higher magnifications of the near surface, peak damage and grain boundary region respectively. (modified with permission from) [23]*

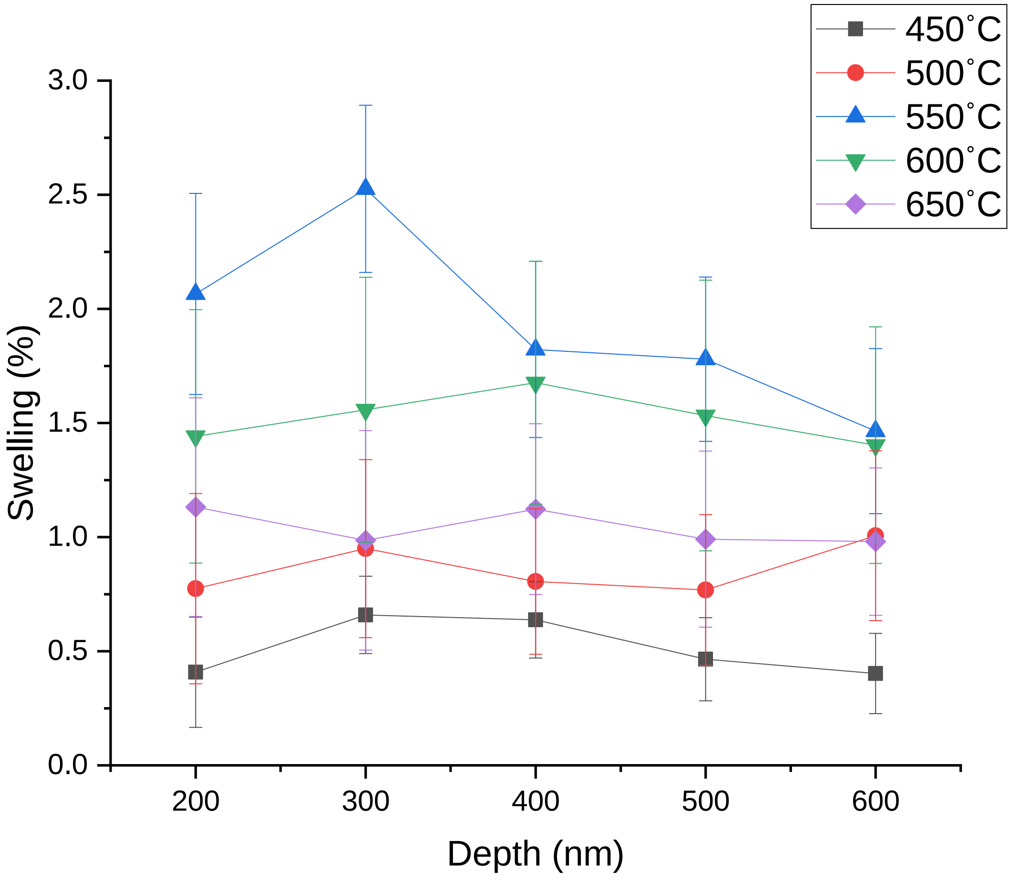

Figure 3.4. Depth-dependent swelling of pure chromium after experiencing 50 peak dpa damage, excluding regions experiencing Ion-specific effects (near surface and injected ion range) (reprinted with permission from) [23]*

With a closer look at Figure 4, it can be clearly observed that the swelling of chromium is quite consistent along the depths from 200nm to 600nm. In clear contrast to this depth independence though, temperature has a profound effect on the amount of void swelling in pure chromium under Fe irradiation. With all samples experiencing the same damage of 50 peak dpa the sample irradiated at 550 °C clearly experienced the largest amount of void swelling. This phenomenon of peak swelling temperature has been well known and observed in similar fashion in pure Iron systems. A main difference though between the pure Iron and Chromium systems are the increase in peak swelling temperature from 475°C to 550°C, which is to be expected since the peak swelling temperature of any alloy is proportional to its melting temperature and the melting temperature of Chromium exceeds the melting temperature of Iron by about 369 K.

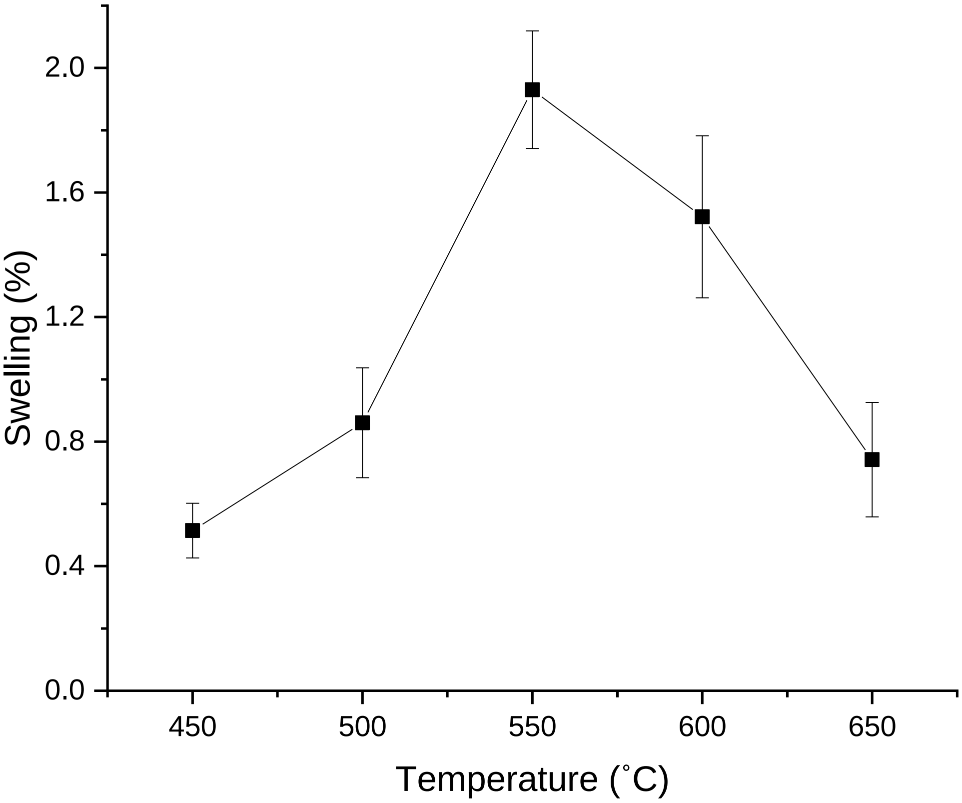

Figure 3.5. Temperature dependent void swelling of pure chromium exposed to 50 peak dpa of 5 MeV Fe damage. Swelling was obtained as the average swelling in the depth regions not experiencing Ion-specific effects. (reprinted with permission from) [23]*

3.3.2 Void alignment

An interesting observation has been made in Fe irradiated chromium in that higher dose samples have the tendency to undergo void alignment.

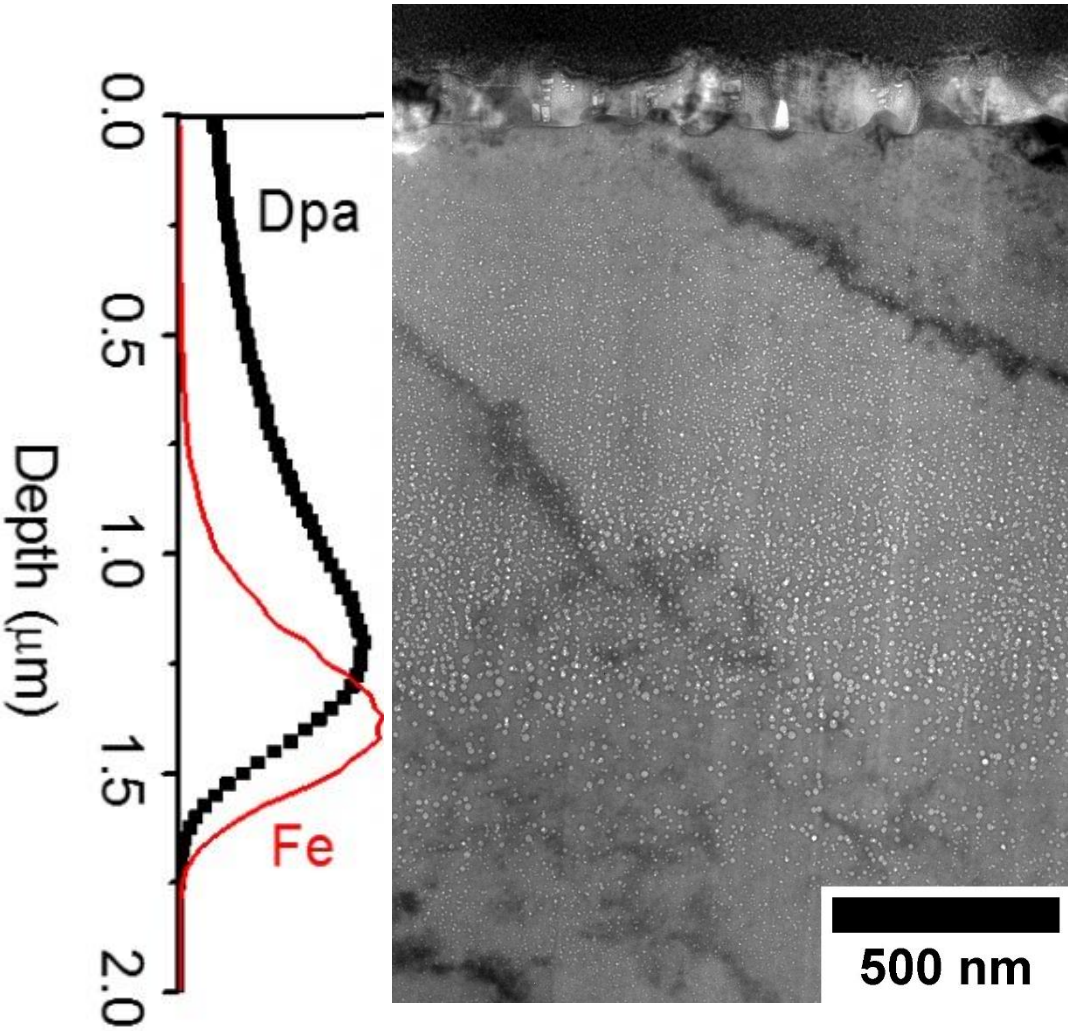

Figure 3.6. TEM image of chromium grain at <111> direction, irradiated to 100 peak dpa at 565°C with 5 MeV Fe. Void alignment can be clearly observed perpendicular to the surface of the sample, indicating an alignment along the [111] direction.

As it can be seen from Figure 6 voids align perpendicular to the surface of the cross-sectional TEM micrograph indicating a alignment along the 111 direction. This phenomenon of defect alignment and formation of superlattices has been observed in different metals subject to implantation of gases and neutron irradiated metals and has been shown to be dependent on damage rate as well as substrate temperature. [19-22].

3.4 Discussion

A baseline behavior of chromium under heavy iron irradiation has been established and a peak swelling temperature of 550 °C has been found. Further investigation has revealed a tendency of chromium to undergo void alignment along the 111 direction when subject to higher dose irradiations under peak swelling temperature.

3.5 References

[1] A.S. Kuprin, V.A. Belous, V.N. Voyevodin, R.L. Vasilenko, V.D. Ovcharenko, G.D. Tolstolutskaya, I.E. Kopanets, I.V. Kolodiy, Vacuum-arc chromium-based coatings for protection of zirconium alloys from the high-temperature oxidation in air, J. Nucl. Mater., 465 (Oct. 2015), pp. 400-406.

[2] Isabel Idarraga-Trujillo, Marion Le Flem, J. C. Brachet, Matthieu Le Saux, Didier Hamon, S. Muller, Valérie Vandenberghe, Marc Tupin, Emilie Papin, Eric Monsifrot, Alain Billard, Frédéric Schuster, Assessment at CEA of coated nuclear fuel cladding for LWRS with increased margins in LOCA and beyond LOCA conditions, Conference Paper LWR Fuel Performance Meeting, Top Fuel 2013, vol. 2 (2013), pp. 860-867

[3] H.-G. Kim, I.-H. Kim, Y.-I. Jung, D.-J. Park, J.-Y. Park, Y.-H. Koo, Adhesion property and high-temperature oxidation behavior of Cr-coated Zircaloy-4 cladding tube prepared by 3D laser coating, J. Nucl. Mater., 465 (Oct. 2015), pp. 531-539

[4] S.J. Zinkle, K.A. Terrani, J.C. Gehin, L.J. Ott, L.L. Snead, Accident tolerant fuels for LWRs: A perspective, Journal of Nuclear Materials 448 (2014) 374–379.

[5] Martin Ševeček, Anil Gurgen, Arunkumar Seshadri, Yifeng Che, Malik Wagih, Bren Phillips, Victor Champagne, Koroush Shirvan, Development of Cr cold spray–coated fuel cladding with enhanced accident tolerance, Nuclear Engineering and Technology, Volume 50, Issue 2, March 2018, Pages 229-236

[6] J.G. Gigax, M. Kennas, H. Kim, T. Wang, B.R. Maier, H. Yeom, G.O. Johnson, K. Sridharan, L. Shao, Radiation response of Ti2AlC MAX phase coated Zircaloy-4 for accident tolerant fuel cladding, Journal of Nuclear Materials 523, 26-32 (2019).

[7] J.G. Gigax, M. Kennas, H. Kim, B.R. Maier, H. Yeom, G.O. Johnson, K. Sridharan, L. Shao, Interface reactions and mechanical properties of FeCrAl-coated Zircaloy-4, Journal of Nuclear Materials 519, 57-63 (2019).

[8] J.G. Gigax, Eda Aydogan, Tianyi Chen, Di Chen, Lin Shao, Y. Wu, W. Y. lo, Y. Yang, F. A. Garner, The influence of ion beam rastering on the swelling of self-ion irradiated pure iron at 450 °C, Journal of Nuclear Materials 465, 343-348 (2015).

[9] L. Shao, Jonathan Gigax, Di Chen, Hyosim Kim, Frank A. Garner, Jing Wang, Mychailo B. Toloczko, Standardization of accelerator irradiation procedures for simulation of neutron induced damage in reactor structural materials, Journal of Nuclear Materials 409, 251-254 (2017).

[10] J.G. Gigax Hyosim Kim, Eda Aydogan, Frank A. Garner, Stu Maloy & Lin Shao Beam-contamination-induced compositional alteration and its neutron-atypical consequences in ion simulation of neutron-induced void swelling, Mat. Res. Lett. 5, 478-485 (2017).

[11] J.F. Ziegler, M.D. Ziegler, J.P. Biersack, SRIM – the stopping and range of ions in matter, Nucl. Instr. Meth. Phys. Res. B 268 (2010).

[12] R.E. Stoller, M.B. Toloczko, G. S. Was, A. G. Certain, S. Dwaraknath, F. A. Garner, On the use of SRIM for computing radiation damage exposure, Nuclear Instruments and Methods in Phys. Res. B 310, 75-80 (2013).

[13] F. A. Garner, "Impact of the Injected Interstitial on the Correlation of Charged Particle and Neutron-Induced Radiation Damage", J. Nucl. Mater., 117 (1983) 177-197.

[14] C. Sun, F.A. Garner, L. Shao, X. Zhang, S.A. Maloy, "Influence of injected interstitials on the void swelling in two structural variants of 304L stainless steel induced by self-ion irradiation at 500°C, Nucl. Instr. Meth. Res. B 409 (2017) 323-327.

[15] C. Sun, L. Malerba, M.J. Konstantinovic, F.A. Garner and S.A. Maloy, "Emulating Neutron-Induced Void Swelling in Stainless Steels Using Ion Irradiation", Proceedings of the 18th International Conference on Environmental Degradation of Materials in Nuclear Power Systems–Water Reactors 2017, The Minerals, Metals & Materials Series, pp. 669-680.

[16] J.G. Gigax, T. Chen, Hyosim Kim, J. Wang, L.M. Price, E. Aydogan, S.A. Maloy, D.K. Schreiber, M.B. Toloczko, F.A. Garner, Lin Shao, "Radiation response of alloy T91 at damage levels up to 1000 peak dpa", J. Nucl. Mater. 482 (2016) 257-265.

[17] E. Getto, G. Vancoevering, G. S. Was, The co-evolution of microstructure features in self-ion irradiated HT9 at very high damage levels, J. Nucl. Mater. 484 (2017) 193-208.

[18] E. Aydogan, T. Chen, J.G. Gigax, D. Chen, X. Wang, P.S. Dzhumaev, O.V. Emelyanova, M.G. Ganchenkova, B.A. Kalin, M. Leontiva-Smirnova, R.Z. Valiev, N.A. Enikeev, M.M. Abramova, Y. Wu, W.Y. Lo, Y. Yang, M. Short, S.A. Maloy, F.A. Garner, L. Shao, "Effect of self-ion irradiation on the microstructural changes of alloy EK-181 in annealed and severely deformed conditions", J. Nucl. Mater. 487 (2017) 96-104.

[19] Krishan, K., “Invited review article ordering of voids and gas bubbles in radiation environments”, Radiat. Eff., 66 (1982) 121.

[20] Jäger, W. and Trinkaus, H., “Defect ordering in metals under irradiation”J. Nucl. Mater., 205 (1993) 394 .

[21] N.M. Ghoniem, D. Walgraff and S.J. Zinkle, Theory and experiment of nanostructure self-organization in irradiated materials Journal of Computer-Aided Materials Design, 8: 1–38, 2002.

[22] D.J. Johnson, P.B. and Mazey, Gas-bubble superlattice formation in bcc metals, J. Nucl. Mater., 218 (1995) 273-288.

[23] Ekaterina Ryabikovskaya, Aaron French, Adam Gabriel, Hyosim Kim, Tianyao Wang, Koroush Shirvan, Frank A. Garner, Lin Shao, Irradiation-induced swelling of pure chromium with 5 MeV Fe ions in the temperature range 450–650 °C, Journal of Nuclear Materials, Volume 543, 2021,

4. DOSE RATE DEPENDENT STUDY

4.1 Introduction

Materials qualifications are impossible without sufficient data on swelling behavior Swelling resistance of any coating film is critical to evaluate the overall structural integrity. As the substrate, Zircaloy does not swell under a neutron environment. If coating films swell easily, the large difference in volume changes between films and tubes can induce significant interface stress and may cause debonding. Although Cr is an essential element in stainless steel, the previous knowledge on void swelling of pure Cr is very limited. A summary on previous findings, including Cr and low-alloying Cr are provided as supplementary information in reference 6, since such data was published in limited-distribution reports written in Russian These studies suggested that Cr belongs to a group of materials that easily swell. Monolithic Cr coating has 0.2% swelling after 0.5 NRT dpa irradiation in Massachusetts Institution Technology testing reactor [6]. The finding, together with other reactor and accelerator irradiation studies [7-11], suggests that Cr has a very short or no incubation period for swelling. Most recently, we have studied Cr swelling in the temperature range of 450–650 °C [12], with observations that (1) for the peak dpa rate of $\sim3.5\times10^{-3}$ dpa/s, maximum swelling temperature occurs at 550 °C , (2) Cr develops superlattice voids at dpa ≥50, and (3) the swelling incubation period is less than 10 dpa. The previous study was performed using only one peak dpa and the dpa rate effect is unclear. The difference from local dpa rates, varying by a factor of ~2, is too small to extract a dependence.

Majority of previous irradiations of pure Cr or low alloying Cr-based alloys were performed at a temperature well above the typical temperatures of pressurized water reactors. Without easy access to testing reactors, accelerators can be used as an effective emulation method to simulate neutron environments [13,14]. One key question to be addressed, is the effect of dpa rates in damage equivalence between accelerator irradiation and reactor irradiation. The expected dpa rate in light water reactors are typically 1×10^{-7} to 1×10^{-6} dpa/s, while the typical dpa rate from an accelerator is 1×10^{-3} dpa/s. The difference in dpa rates over three orders of magnitude expects to shift the swelling peaks. There are two modeling approaches to estimate such temperature shifting. The model from Brailsford and Bullough considers defect trapping and defect emission from each type of defect sinks, considering the difference in neutral sinks, variable-bias sinks, and fixed-biased sinks. The net vacancy flux to voids determines the swelling rate. In this model, the flux of each type of point defect is influenced by all sink types. In the model from Mansor, only one type of defect sink is included, and defect emission is not included. The dpa rate effect also depends on the invariance assumed under different irradiation conditions.

The present study on dpa rate effects in Cr has significance in both materials development and fundamental studies. From the viewpoint of irradiation testing, developing predicting capability on Cr swelling at reactor temperatures and reactor characteristic dpa rate is important for Cr quantification. From the viewpoint of radiation materials science, Cr is unique for studying dpa rate effect because of two reasons: first, Cr swells easily. Due to the fact that Cr swells readily at low overall damage, very low dpa rates can be used to achieve said damages in a reasonable timeframe. Second, Cr has a low or no swelling incubation period. This helps to compare with dpa rate effect formulas from previous studies since both models do not include void nucleation.

For the present study, the testing matrix includes three dpa rates of 3.5´10-5, 3.5´10-4, 3.5´10-3 dpa/s, at temperatures of 350 °C, 450 °C, 500 °C, 550°C,600 and 650°C, respectively. All irradiations reach 15 peak dpa. The two orders of magnitude in damage rate difference is large enough to show the temperature shift effect systematically. For the highest dpa rates, a beam current of 400 nA was applied which is still reasonable to minimize the beam heating effect (~5

°C). For the lowest dpa rate, a beam current of 4 nA is still reasonable to finish the irradiation after 120 hours.

4.2 Experimental procedure

Cr samples of purity of 99.95% were obtained from Goodfellow (Coraopolis, PA, USA). They were polished using silicon carbide sandpaper to 2400 grid, and subsequently, electro polished using a Tenupol 5 twin jet electro-polisher. The etching solution was 5% perchloric acid mixed with 95% methanol. The polishing time for each individual sample was ~20 seconds with a voltage gradient of 19.5 V between the sample and solution. After the polishing remaining acid residue was removed by repeatedly rinsing the samples in methanol. Samples were then dried with nitrogen gas. Figure 4.1 shows a typical SEM image of one polished Cr sample. The grain boundaries are clearly visible. Grain sizes vary from ~200 mm to ~600 mm. No deformation or twining is observed on the surface. The polished Cr samples were irradiated using 5 MeV Fe ions. For the present study, Fe ions were selected since the beam current can be adjusted up to two orders of magnitude difference. Ideally, Cr self-ion beam is the best choice, but a stable Cr ion beam cannot be produced using a Cs sputtering-based ion source, largely due to Cr’s high oxygen affinity. The Fe ion beam current is controlled primarily by adjusting Cs flux for sputtering. The beam currents are changed by two orders of magnitude, with the equivalent of peak damage rate of 3.5×10^{-3} dpa/s, 3.5×10^{-4} dpa/s, and 3.5×10^{-5} dpa/s, respectively. Although the beam heating at the highest dpa rate is small (~5 °C), the beam heating is not ignored and is included as one contribution to sustain the substrate temperature, which means the power to the heat stage is automatically adjusted. Also, the sample thickness is intentionally controlled to be about 0.5 mm to minimize the temperature gradient. A static beam is used in all irradiations since a raster beam creates a pulse beam effect in which void swelling is suppressed [15]. The vacuum of the target chamber was maintained at 8×10^{-8} torr or better during all irradiations

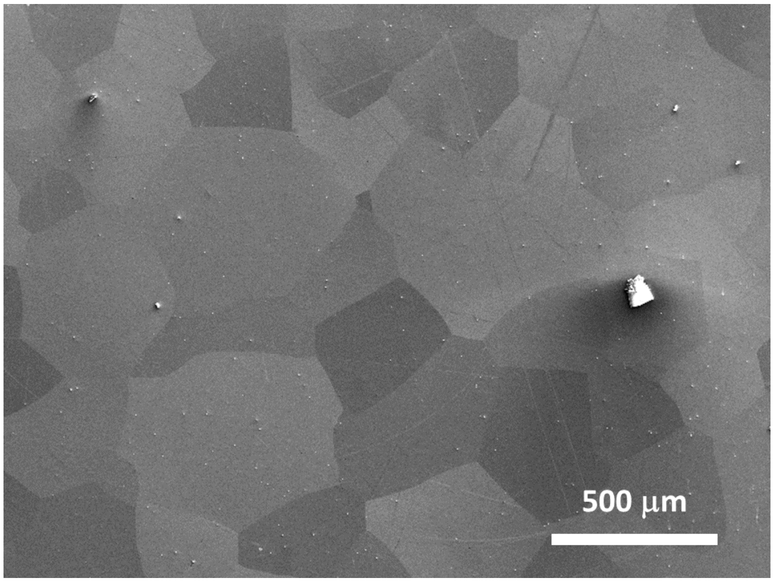

Figure 4.1. SEM image of polished Cr prior to ion irradiation.

Furthermore, a multiple beam deflection technique was utilized to minimize carbon contamination [16,17]. The feedback for the temperature control of the sample stage was provided by a thermocouple attached to the stage. The temperature variations during the irradiation is less than ± 5 °C.

The 5 MeV Fe ions create a damage layer that peaks at about 1.2 µm. The projected range of Fe ions is about 1.4 µm. All irradiations have an ion fluence of $1.51 * \frac{10^{16} Ions}{cm^2}$ equivalent to 15 peak dpa. Figure 4.2. shows the damage profile and Fe implant profiles obtained via using the Stopping and Range of Ions in Matter (SRIM) code [18]. The Kinchin-Pease model is used for damage calculation [19], and Cr displacement energy is 40 eV [20]. The amount of Fe implanted has a peak concentration about 0.4%, which is too small to cause a significant doping effect. The swelling analysis covers the whole range but the analysis on swelling resistance of Cr carefully excludes Fe projected range, as to be discussed.

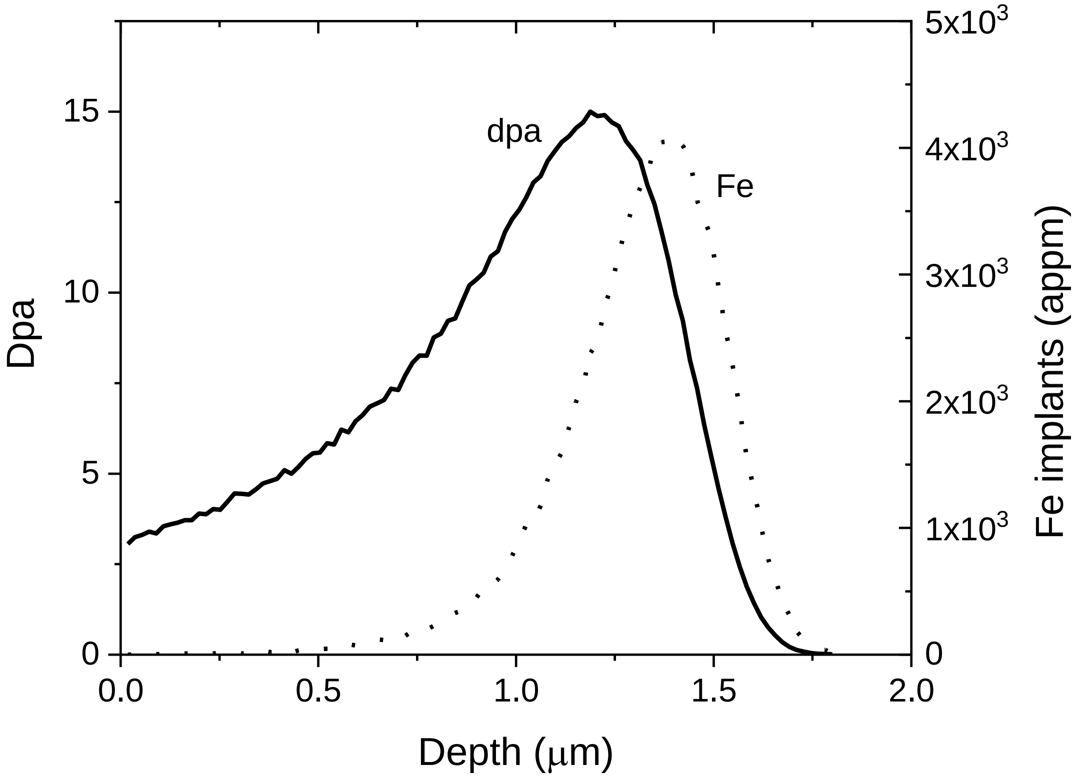

Figure 4.2. SRIM predicted dpa profile and Fe implant profile for 5 MeV Fe ions in Cr.

The samples are characterized by using a FEI Tecnai F20 ST Transmission Electron Microscopy (TEM) with an operating voltage of 200 kV. TEM specimens are prepared by using a Tescan LYRA-3 Model GMH Focused Ion Beam Microscope (FIB). The thickness of each sample was determined via standard electron energy loss spectroscopy (EELS). The thickness is measured at multiple points to check the uniformity. The thickness has a slight variation from the bottom to the top of the TEM specimen (<20%), and such changes are included in the local void swelling analysis.

The swelling data and void statistics used in all graphs and calculations were derived via the use of representative squares of 50 nm width and 200 nm depth that were taken from the TEM micrographs of each sample. For the calculation of swelling, we use $Swelling\,\% = V\%/(1 - V\%)$, where $V\%$ is the volume fraction of voids measured from TEM.

4.3 Summery of Experimental Results

Figure 4.3a shows the cross-sectional TEM image of the sample irradiated at 450 °C by using the lowest dpa rate (3.5×10^{-5} dpa/s). It consists of multiple images combined over the whole irradiated region up to 2 μm. Figure 4.3b plots the swelling as a function of depth. SRIM calculated dpa curve is also provided for the comparison. The overall swelling changes agree with the damage profile. Swelling is peaked at about 1.1 μm, which is shallower than, but very close to, the peak damage. Figure 4.3c plots the void diameter changes as a function of depth. The error represents the statistic distributions of void sizes at each depth interval. The average void size changes roughly follow the damage profile, with the largest voids observed at a depth of about 1.1 μm. Figure 4.3d plots the void density changes as a function of depth. Different from depth dependence change of void sizes, void density is peaked at 0.5 μm and decreases at deeper depths. If we ignore the near-surface region (shallower than 0.3 μm, to be safe) due to the possible free surface defect sink effect and the deep region (>1.2 μm) due to the injected interstitial and Fe doping effect, the depth regions of 0.5 μm to 1.1 mm exhibit the following trend: with increasing local dpa, swelling is increased, void sizes become larger and void density becomes lower. Such

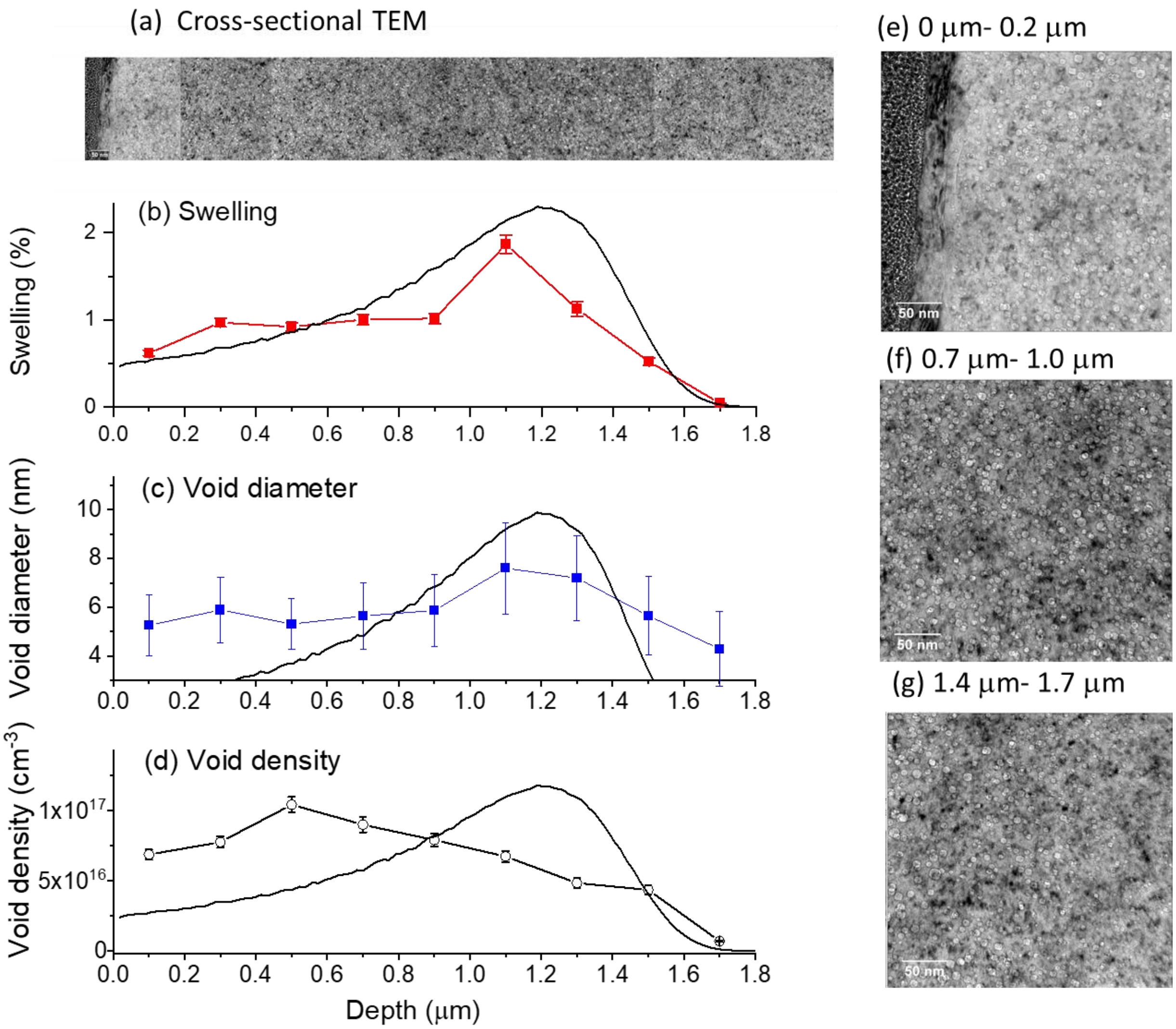

Figure 4.3. (a) Cross-sectional TEM image of Cr irradiated by 5 MeV Fe ion to 15 peak dpa, at 450 °C, and with the lowest dpa rate of 3.5×10^{-5} dpa/s, (b) the corresponding depth profile of swelling, (c) the depth profile of void diameter changes, (d) the depth profile of void density, and (e-g) enlarged TEM image at depths 0-0.2 μm, 0.7-1.0 μm, and 1.4-1.7 μm, respectively. SRIM obtained dpa profile is also plotted in (b-d).

void morphology difference is expected from Ostwald ripening [21]. Classical Ostwald ripening theory predicts that, with increasing precipitate volume (analogous to swelling), the average radius of precipitates (analogous to void sizes) increases, and precipitate density (analogous to void densities) decrease. Such opposite trend changes of size and density are due to the competitive growth when the precipitate volume is considered. The growth rates of precipitates are determined not only by the difference between the bulk solute concentration and the equilibrium solute concentration around a precipitate but also by the precipitate size and total precipitate volume (analogous to void size and the local swelling, respectively). Both the precipitate size and the precipitate volume appear as an additional modification to the growth rate [21]. The higher the precipitate volume, the higher the growth rate for the same precipitate radius. Hence, larger precipitate volumes lead to lower densities and larger average precipitate sizes [21]. Note that classical Ostwald ripening theory is for a close system in which the total solute atoms are conserved. Ion irradiation is an open system in which the total vacancy number is increasing as a function of irradiation time. The difference between open- and classical closed system Oswald ripening is sufficiently large, that to date, there has not been an analytical solution available for the case of Oswald ripening in Ion irradiation induced void swelling. The analogies between Oswald ripening and its major feature of competitive growth and its impact on total swelling though aid in the understanding of Fig 3c and 3d.

Figure 4.4. compares the typical TEM images obtained from the depth region of 0.7-1.0 μm for all samples irradiated under various conditions. The rows refer to the same dpa rates, and the column refers to the same irradiation temperatures. The labeling of a, b, c, and d refers to irradiation temperatures of 350 °C, 450 °C, 550 °C, and 650 °C, respectively. The labeling of 1, 2, and 3 refers to dpa rates of 3.5×10^{-3} (dpa/s) (also referred as high dpa rate in the following discussion), 3.5×10^{-4} (dpa/s) (medium dpa rate), and 3.5×10^{-5} (dpa/s) (low dpa rate). Voids are

observed in all images. All TEM images show spherical voids, except for figure c-3, d-2, and d-3, in which box-like voids appear.

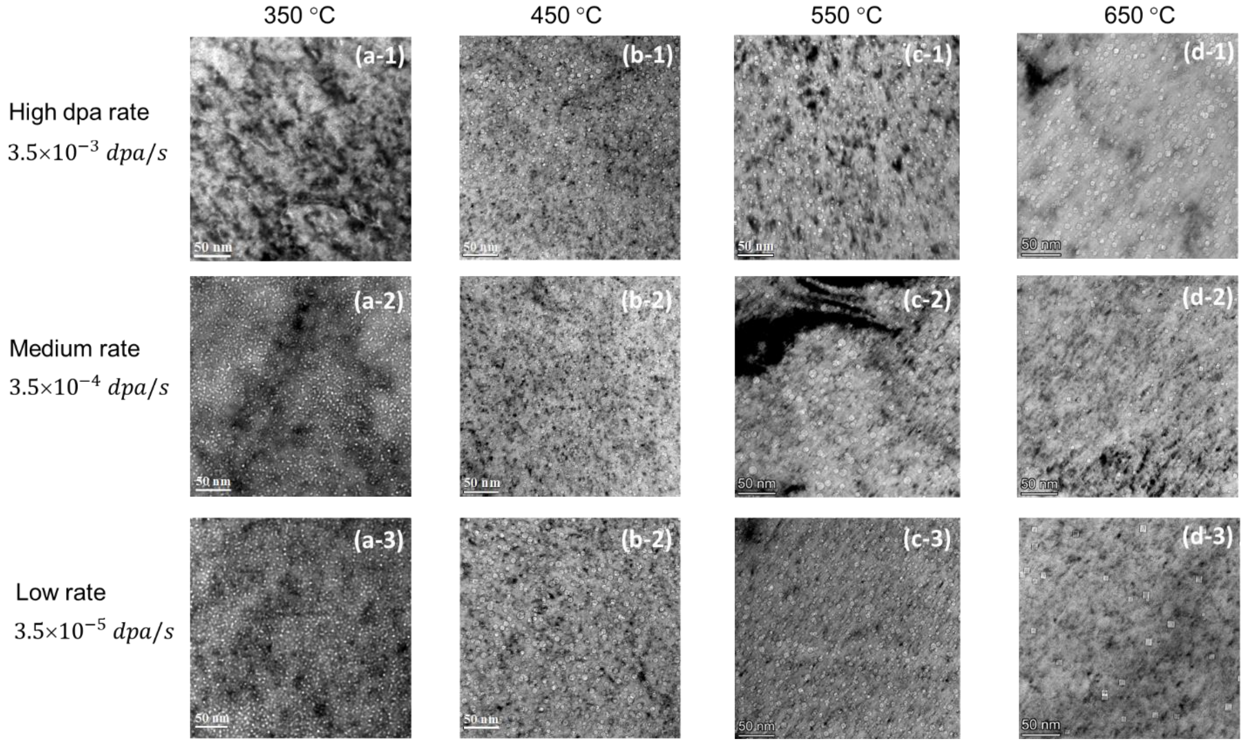

Figure 4.4. TEM image of Cr irradiated by 5 MeV Fe ions at (a-1) 350 °C using a high dpa rate of 3.5×10^{-3} dpa/s, (a-2) 350 °C using a medium dpa rate of 3.5×10^{-4} dpa/s, (a-3) 350 °C using a low dpa rate of 3.5×10^{-4} dpa/s, (b1-b3) 450 °C using three different dpa rates, (c1-c3) 550 °C using three different dpa rates, and (d1-d3) irradiation at 650 °C using three different dpa rates. All TEM images are taken from the depth region 0.7-1.0 μm.

These three figures correspond to low dpa rate irradiation at 550 °C, medium dpa rate irradiation at 650 °C, and low dpa rate irradiation at 650 °C. Note that these three conditions have the largest thermal budgets (the product of temperature and time period) to develop square voids. The evolution from spherical voids to box-like voids requires sufficient atomic mobility. Thus, atoms on the inner lining of voids can reposition themselves to minimize void formation energies. The final void shape is determined by Wulff construction. The evolution can be achieved by either direct atom jumps on the inner surface of voids or by vacancy dissolution and re-absorption by voids. One consequence of the shape change is the change in vacancy binding energies. For spherical voids, the void curvature plays a determinizing role in binding energy. Once evolved into a box-like cavity, the disappearance of curvature makes the void surface more like a free surface. This definitely influences the vacancy concentrations around voids and further changes the vacancy diffusion flux among voids. In other words, void growth is not necessary to follow the growing trend of small voids of spherical shapes.

Figure 4.5. plots the void size distributions in the depth region of 0.6 mm to 0.8 mm. The solid lines are Gaussian fitting of void distributions. For irradiations using the same dpa rate (corresponding to a row), higher temperatures lead to large void sizes and fewer void counts. For example, for the irradiation using a high dpa rate (3.5×10^{-3} dpa/s), the average void sizes are 4.0 nm at 350 °C, 3.9 nm at 450 °C, 4.9 nm at 550 °C, and 5.8 nm at 650 °C. For the irradiating using a medium dpa rate (3.5×10^{-4} dpa/s), the average void size is 3.2 nm at 350 °C. It increases to 4.6 nm at 450 °C, and to 5.0 nm at 550 °C. However, the average void size reduces to 4.0 nm at 650 °C. As pointed above, this condition (Figure 4.5. d2) begins to develops box-like voids and the void growth may deviate from the trend due to the change in void binding energies. For the low dpa rate irradiation (3.5×10^{-5} dpa/s), the average void size increase from 4.2 nm at 350 °C to 5.8 nm at 450 °C. At 550 °C, the size reduces to 4.7 nm. Again, this condition develops box-like voids, instead of spherical voids, due to prolonged irradiation time required for a low dpa rate.

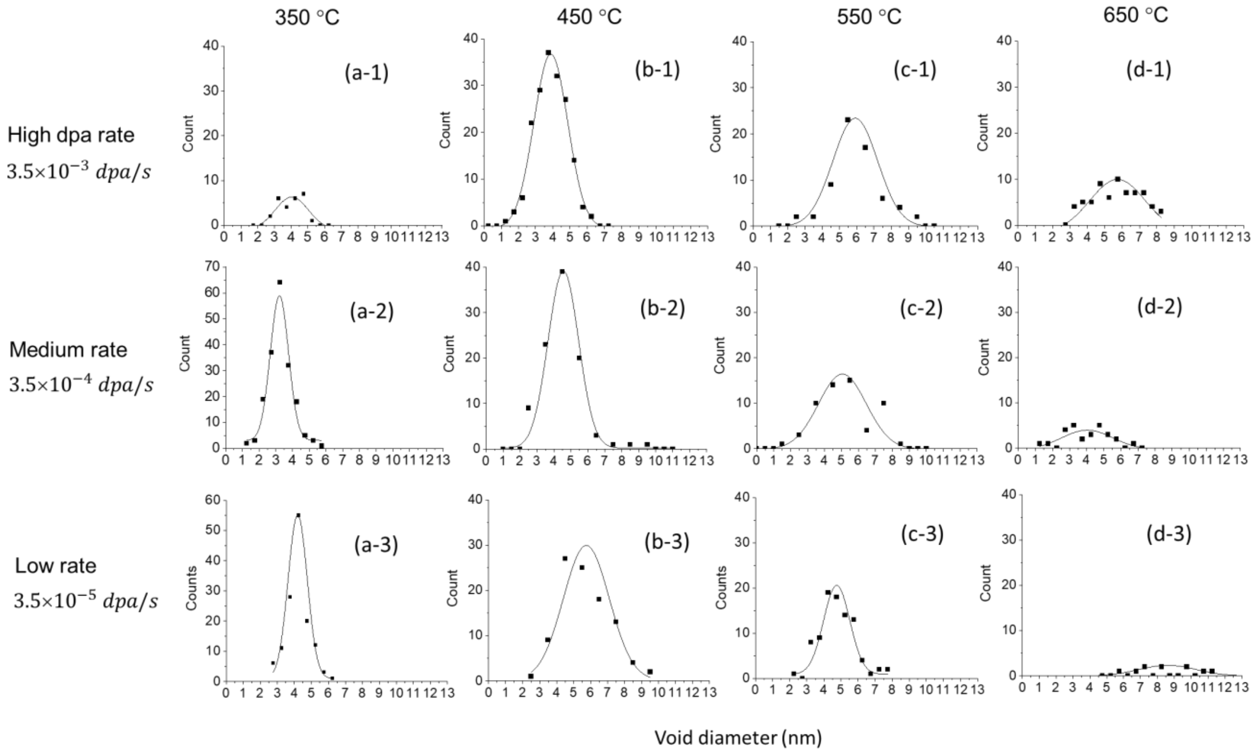

Figure 4.5 Void analysis of the depth region of 0.6 to 0.8 μm in Cr irradiated by 5 MeV at (a-1) 350 °C using a high dpa rate, (a-2) 350 °C using a medium dpa rate, (a-3) 350 °C using a low dpa rate, (b1-b3) 450 °C using high, medium, and low dpa rates, (c1-c3)) 550 °C using high, medium, and low dpa rates, and (d1-d3) 650 °C using high, medium, and low dpa rates. The high dpa rate refers to 3.5×10^{-3} dpa/s. The medium dpa rate refers to 3.5×10^{-4} dpa/s. The low dpa rate refers to 3.5×10^{-5} dpa/s. The solid lines are Gaussian fitting.

Figure 4.6. plots swelling profiles in all samples. The solid lines are dpa profiles. As a general observation, the swelling profiles follow the damage profile, particularly for the irradiations using the high dpa rate. As shown in Figure 4.9 a-1, b-1, c-1, and d-1, swelling in all four temperatures share one common feature that swelling increases as a function of depth, reaches a peak at a depth very close to the peak damage, and reduces quickly at deep depths. For

irradiation using the low dpa rate, however, swelling shows weak dependence on depths (or local dpa values). As shown in Figure 4.6. a-3, b-3, c-3, and d-3, swelling appears relatively flat within the damaged regions.

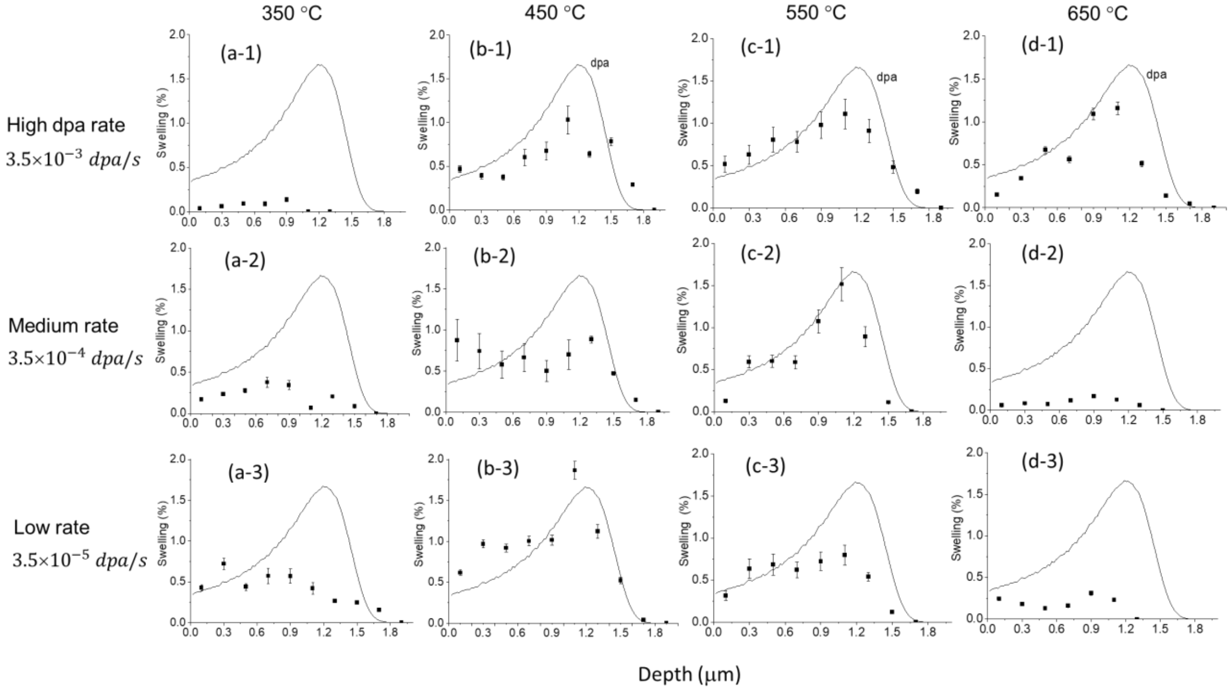

Figure 4.6. Depth profiles of void swelling in in Cr irradiated by 5 MeV at (a-1) 350 °C using a high dpa rate, (a-2) 350 °C using a medium dpa rate, (a-3) 350 °C using a low dpa rate, (b1-b3) 450 °C using high, medium, and low dpa rates, (c1-c3)) 550 °C using high, medium, and low dpa rates, and (d1-d3) 650 °C using high, medium, and low dpa rates. The high dpa rate refers to 3.5×10^{-3} dpa/s. The medium dpa rate refers to 3.5×10^{-4} dpa/s. The low dpa rate refers to 3.5×10^{-5} dpa/s. The solid lines are SRIM-calculated dpa profiles.

The details of swelling distributions are important for data analysis. If swelling profiles follow local dpa profiles, as observed in the high dpa rate irradiation, it is possible to extract swelling as a function of local dpa values. If the swelling profiles become less sensitive to local dpa values, as observed in a few irradiations using the lowest dpa rate (Figure 4.6. a-3, c-3, and d-3), swelling should be averaged over a depth region. If the swelling peaks occurs at the surface, data interpretation is difficult since defect removal through the surface may be significant. Such sharp surface swelling peak is not observed in all irradiations.

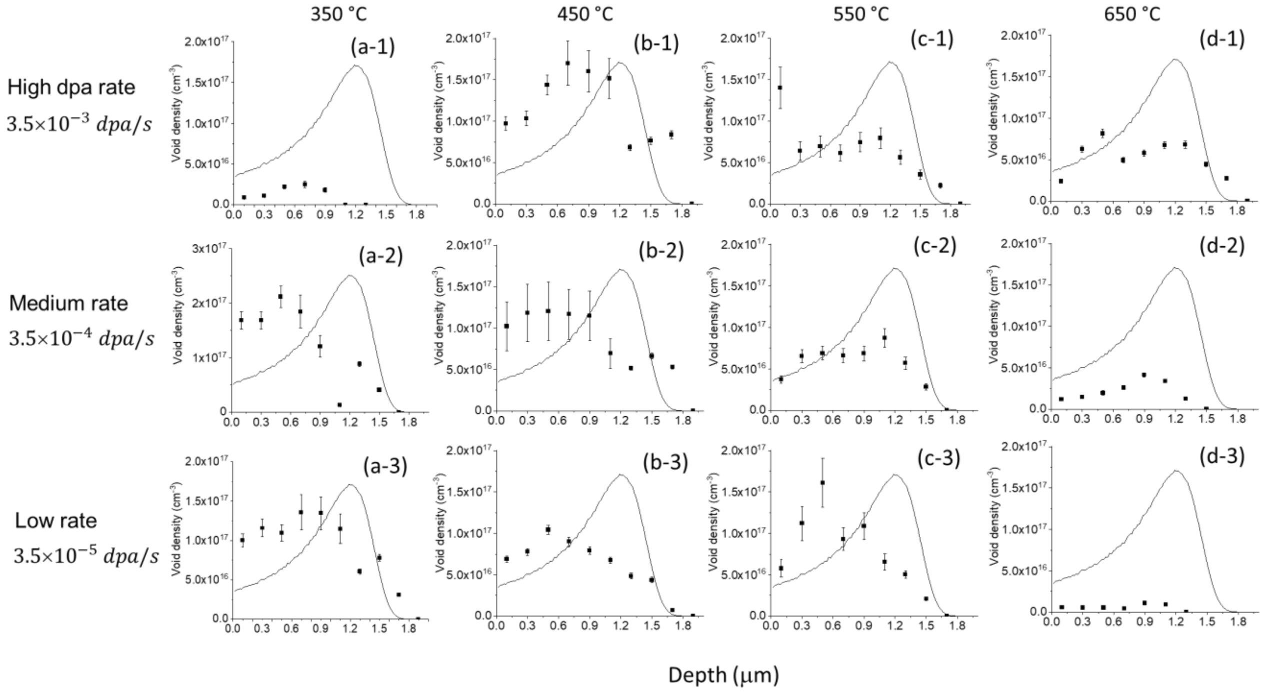

Figure 4.7 Depth profiles of void densities in in Cr irradiated by 5 MeV at (a-1) 350 °C using a high dpa rate, (a-2) 350 °C using a medium dpa rate, (a-3) 350 °C using a low dpa rate, (b1-b3) 450 °C using high, medium, and low dpa rates, (c1-c3)) 550 °C using high, medium, and low dpa rates, and (d1-d3) 650 °C using high, medium, and low dpa rates. The high dpa rate refers to 3.5×10^{-3} dpa/s. The medium dpa rate refers to 3.5×10^{-4} dpa/s. The low dpa rate refers to 3.5×10^{-5} dpa/s. The solid lines are SRIM-calculated dpa profiles.

Figure 4.7. plots the void density distributions for all irradiation conditions. The void density profiles are different from the swelling profiles. First, the void swelling profiles (Figure 4.6.), in general, follow dpa profiles with swelling peaks very close to damage peaks. The void density profiles, in general, reach a peak at about half of the projected range and decrease at deeper depths. Lower void densities at higher swelling level is characteristics of Ostwald ripening. Second, under a fixed dpa rate, void densities decrease with increasing temperatures, which is also characteristic of Ostwald ripening. The only exception is the high dpa rate irradiation at 350 °C (Figure 4.7. a-1), which can be explained by the difficulty in void nucleation at such a low temperature, or the difficulty of TEM to characterize ultra-small voids. Third, under the same temperature, void densities do not change dramatically for different dpa rates, except for the highest temperature 650 °C. Void densities are systematically reduced at lower dpa rates for 650 °C. This suggests that the thermal annealing effect cannot be ignored for prolonged annealing at high temperatures.

4.3.1 Shift of peak swelling temperature

Figure 4.8. compares the swelling as a function of irradiation temperatures for all three dpa rates. Swelling data is averaged through the region 0.2 μm to 1.0 μm. The solid lines are polynomial fitting of the third order used to extract the temperature of the maximum swelling under each dpa rate. The swelling temperature decreases with decreasing dpa rates. For the high dpa rate of 3.5×10^{-3} dpa/s, the maximum swelling temperature is 565 °C. For the medium dpa rate of 3.5×10^{-4} dpa/s, the maximum swelling temperature is shifted to 520 °C. For the low dpa rate of 3.5×10^{-5} dpa/s, the maximum swelling temperature is shifted to 480 °C. The maximum swellings of both low and high dpa rates are comparable to each other within the error bars. The maximum

swelling of the medium dpa rate is lower. This can be understood by the effect of defect removal through the surface. For the low dpa rate, the maximum swelling temperature is low, and the vacancy removal can be low since low vacancy diffusivity at low temperature, even the irradiation time period is long. For the high dpa rate, the maximum swelling temperature is high. Although the vacancy diffusivity is high, but the irradiation time period is short. Hence the amount of vacancy removal from the surface can be limited as well.

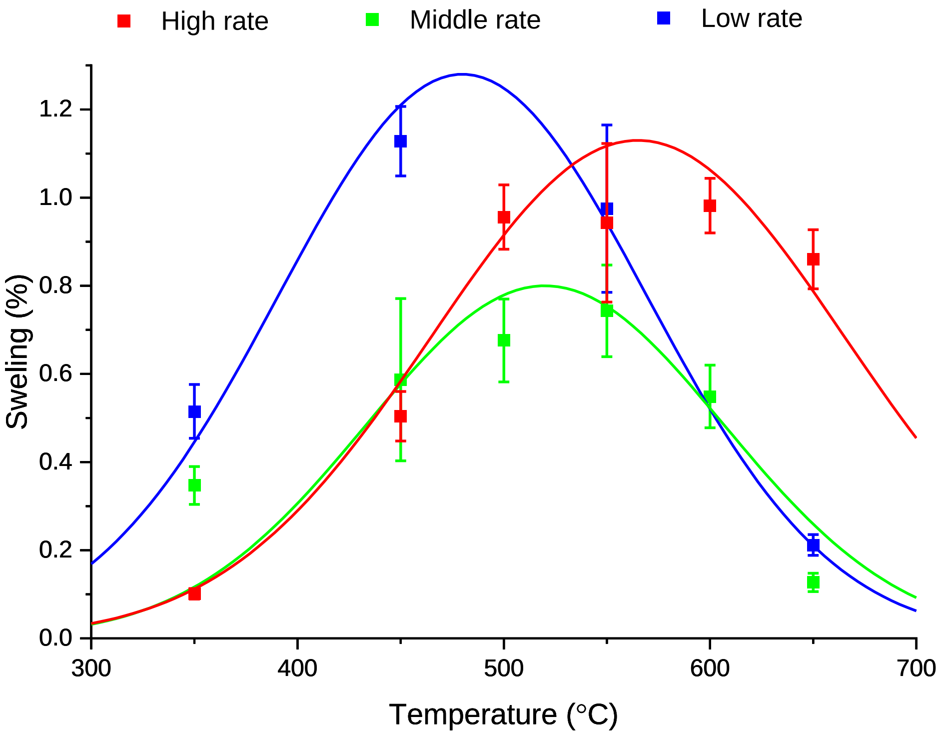

Figure 4.8. Swelling as a function of irradiation temperature for thee dpa rates (3.5×10^{-3} dpa/s, 3.5×10^{-4} dpa/s, 3.5×10^{-5} dpa/s). Swelling data is averaged in the region 0.2 μm to 1.0 μm.

For medium dpa rate, the vacancy removal can be higher than the other two cases, leading to lower peak swelling.

4.3.2 Extrapolation of swelling temperature to low damage rates

Figure 4.9. plots the maximum swelling temperatures as a function of dpa rates. The solid line is a liner fitting using logK as the variable. The above equation suggests the following relationship of T_{peak} and K.

$$\frac{1}{T_{peak}} \approx a \times log_{10}K + c \qquad [1]$$

where a and c are two temperature independent constants, under the assumption that dislocation density and neutral defect sinks are not changed.

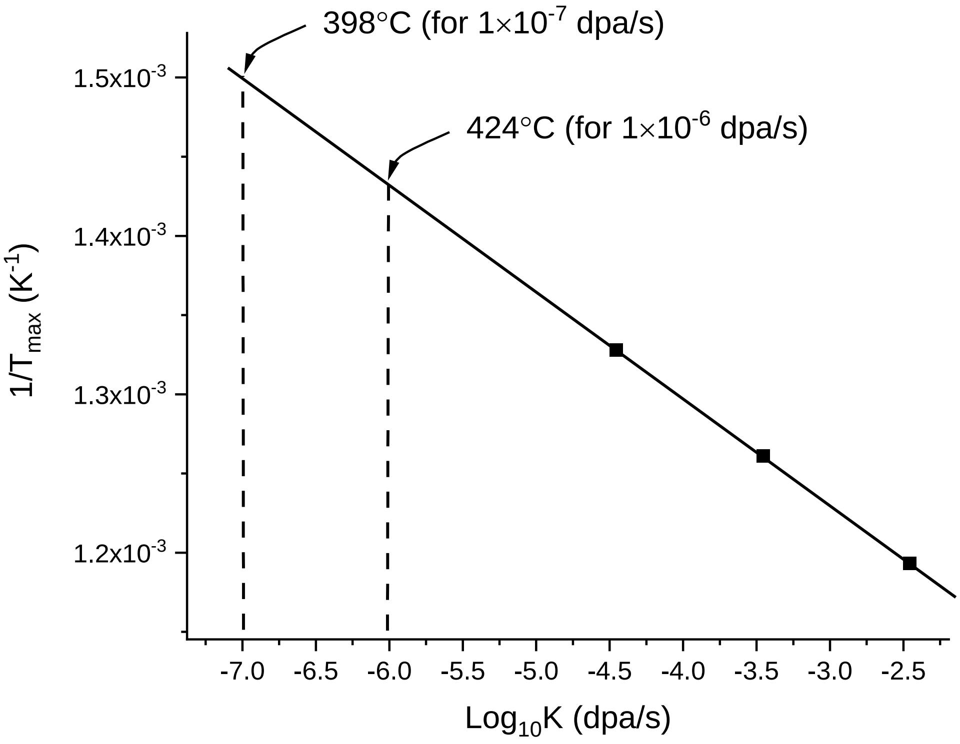

Figure 4.9 The plot of the reciprocal of the maximum swelling temperatures as a function of peak dpa rates in log scale. The solid line is a linear fitting.

Such T_{peak} dependence on K is observed in the present study by plotting $\frac{1}{T_{peak}}$ vs. $log_{10}K$, as shown in Figure 4.8.The linear fitting obtains $a = -6.74 \times 10^{-5} \pm 2.11 \times 10^{-6}$, and $b = 1.03 \times 10^{-3} \pm 7.48 \times 10^{-7}$, which can be used to predict T_{peak} $(in\ Kelvin)$ and K $(in\ \frac{dpa}{s})$. For typical reactor dpa rates of 1×10^{-7} dpa/s (LWRs) and 1×10^{-6} dpa/s (fast reactors), the T_{peak} values are 398 °C and 424 °C

The above T_{peak} dependence on dpa rate K can be understood based on the theory proposed by Brailsford and Bullough [22]. In this classical paper, defect sinks are divided into different types, including (1) neutral sinks such as voids which have no preference for trapping interstitials or vacancies, (2) variable-bias sinks such as coherent precipitates, which have a finite capacity for defect trapping, and their trapping bias is influenced by other sinks, and (3) fixed-bias sinks such as dislocation loops which preferentially trap interstitials. The model also considers the defect emission difference for different point defects. For example, the emission of interstitials is not included for sink types since interstitial defect formation energy is high. On the other hand, the emission of vacancies depends on sink types. For example, dislocation loops have different vacancy emissions in comparison with that of networking dislocation. With all defect sink effects included in the rate theory, the defect flux towards voids are used to calculate void growth, which leads to the following expression [23]

$$\frac{1}{T_{peak}} \approx \frac{2.3 \times k}{Q + E_m^V} log_{10} \left\{ \left(\frac{Q}{E_f} \right) \frac{\left[D_V^0 (\rho_d + 4\pi r_s C_s) \right]^3 \rho_d^L}{10^{17} K^2 (Z_i - Z_v) \rho_d} \right\}$$

where

T_{peak} temperature having the maximum swelling rate (swelling per dpa)

k Boltzmann constant

Q activation energy for self diffusion ($Q = E_m^V + E_f^V$)

E_m^V vacancy migration energy

D_V^0 vacancy diffusivity prefactor

ρ_d the total dislocation density

ρ_d^L the dislocation loop density

r_s trapping radius of neutral sinks

C_s density of neutral sinks

K dpa rate

Z_i the efficiency to catch an interstitial by dislocations

Z_v the efficiency to capture a vacancy by dislocations

Assuming that all defect sink density and sink strength are temperature independent leads to equation [1]. Hence, the present study confirms the accuracy of the model in the first-order approximation. Another popular model in explanation of dpa rate effect was given by Mansor [23,24]. In this model, an invariance, such as defect flux or net defect flux, is introduced to establish an equivalence under different irradiation conditions. However, it is difficult to apply Mansor's temperature shifting equation since the model does not provide a description of swelling temperature peak as the other mode, and it is not straightforward to define the invariance at the maximum swelling temperature. Note the swelling rate at the peak swelling is not necessary to the same under different dpa rates.

It is feasible to use a single ion irradiation to obtain the swelling dependence on local dpa after excluding the regions which are affected by the surface and injected interstitial. Local dpa rates along the ion path are somewhat different in a single ion irradiation but the effect might be second-order and therefor ignorable considering the difference is only a factor of two difference from 0.4 µm to 1.0 µm. Figure 4.10. combines the data from the present study (15 peak dpa) and previous studies (50 and 100 peak dpa Ribjakovkaja et al.). All curves appear to reasonably merge into one single dpa dependence curve. Note the 15 peak dpa data from the present study were obtained using the peak dpa rate of 3.5×10^{-3}dpa/s, but the 50 and 100 peak dpa data were obtained using a peak dpa rate of 1.75×10^{-3}dpa/s.

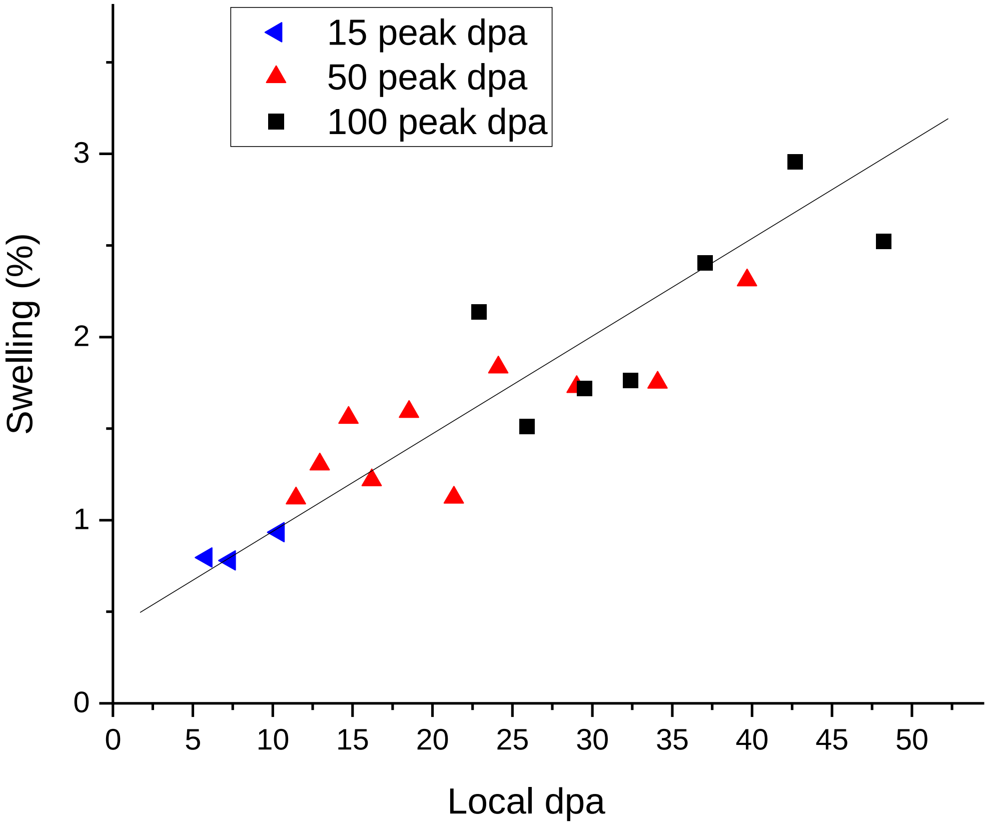

Figure 4.10. Swelling as a function of local dpa, obtained from Cr irradiated by 5 MeV Fe ions at 550°C, and up to 15, 50, and 100 peak dpa.

Once again, we assume that a factor of 2 difference is a second-order effect that does not invalidate our current study spanning two orders of magnitude in dpa rate. The consistency on dpa dependence of swelling in Figure 4.10. suggests that it is feasible and reliable to use depth-dependent swelling to predict swelling behaviors at large damage levels.

Our previous studies at peak dpa > 50 have observed superlattice void formation. There is no such superlattice void formation observed in the present study because of its relatively lower damage level (15 peak dpa). Superlattice voids maximize the void density and make voids as the dominant sinks for point defects. Once void becomes dominant defect sinks instead of dislocations, swelling will reach saturation [24]. This might be the cause of low swelling rate observed (0.04-0.05% /dpa).

4.4 DISCUSSION

Figure 4.3a shows the cross-sectional TEM image of the sample irradiated at 450 °C by using the lowest dpa rate (3.5×10^{-5} dpa/s). It consists of multiple images combined over the whole irradiated region up to 2 μm. Figure 4.3b plots the swelling as a function of depth. SRIM calculated dpa curve is also provided for the comparison. The overall swelling changes agree with the damage profile. Swelling is peaked at about 1.1 μm, which is shallower than, but very close to, the peak damage. Figure 4.3c plots the void diameter changes as a function of depth. The error represents the statistic distributions of void sizes at each depth interval. The average void size changes roughly follow the damage profile, with the largest voids observed at a depth of about 1.1 μm. Figure 4.3d plots the void density changes as a function of depth. Different from depth dependence change of void sizes, void density is peaked at 0.5 μm and decreases at deeper depths.

4.5 References

[1] Hyun-Gil Kim, Jae-Ho Yang, Weon-Ju Kim, Yang-Hyun Koo, Development Status of Accident-tolerant Fuel for Light Water Reactors in Korea, Nuclear Engineering and Technology 48, 1-15 (2016).

[2] H.G. Kim, I.H. Kim, Y.I. Jung, D.J. Park, J.Y. Park and Y.H. Koo, Adhesion property and high-temperature oxidation behavior of Cr-coated Zircaloy-4 cladding tube prepared by 3D laser coating, J. Nucl. Mater., 465 (2015), pp. 531-539

[3] Martin Ševeček, Anil Gurgen, Arunkumar Seshadri, Yifeng Che, Malik Wagih, Bren Phillips, Victor Champagne, Koroush Shirvan, Development of Cr cold spray–coated fuel cladding with enhanced accident tolerance, Nuclear Engineering and Technology, Volume 50, Issue 2, March 2018, Pages 229-236

[4] J.G. Gigax, M. Kennas, H. Kim, T. Wang, B.R. Maier, H. Yeom, G.O. Johnson, K. Sridharan, L. Shao, Radiation response of Ti2AlC MAX phase coated Zircaloy-4 for accident tolerant fuel cladding, Journal of Nuclear Materials 523, 26-32 (2019).

[5] J.G. Gigax, M. Kennas, H. Kim, B.R. Maier, H. Yeom, G.O. Johnson, K. Sridharan, L. Shao, Interface reactions and mechanical properties of FeCrAl-coated Zircaloy-4, Journal of Nuclear Materials 519, 57-63 (2019).

[6] Peter J. Doyle a, Takaaki Koyanagi, Caen Ang, Lance Snead, Peter Mouche, Yutai Katoh, Stephen S. Raiman, Evaluation of the effects of neutron irradiation on first-generation corrosion mitigation coatings on SiC for accident-tolerant fuel cladding, Journal of Nuclear Materials 536 (2020) 152203

[7] V.I.Trefilov, V.F.Zelenskiy, I.M.Nekhludov, A.N.Rakitskiy, .N.Voevodin, L.S.Ozhigov, V.S. Karasev, A.P.Rudoy, V.N.Minakov, Y.V. Milman, A.S. Davidenko, Minor-alloyed Cr-based alloys, RM-8 (1991) pp. 185-194 (in Russian).

[8] V. P. Chakin, V. A. Kazakov, “Radiation resistance of minor-alloyed Cr alloys”, RIAR preprint No. 7 (790), RIAR, Dimitrovgrad, (1990) in Russian.

[9] V.Bryk, V.N.Voevodin, V.F.Zelenskiy, B.V.Matveenko, I.M.Nekhludov, V.K.Horenko, T.P.Chernyaeva, A.N.Rakitskiy, V.I.Trefilov, Investigation of radiation swelling of the deformed minor-alloyed Cr alloy under its irradiation at the accelerator. VANT 1981, pp. 33-38 (in Russian)

[10] V.V. Bryk, V.N. Voyevodin, I.M. Neklyudov, A.N. Rakitskij, Microstructure investigation of Cr and Cr alloys irradiated with heavy ions, Journal of Nuclear Materials 225 (1995) 146-153. Nuclear Materials 225 (1995) 146-153

[11] A.S. Kuprin, V.A. Belous, V.N. Voyevodin, R.L. Vasilenko, V.D. Ovcharenko, G.D. Tolstolutskaya, I.E. Kopanets, I.V. Kolodiy, Journal of Nuclear Materials 510 (2018) 163-167

[12] Ekaterina Ryabikovskaya, Aaron French, Adam Gabriel, Hyosim Kim, Tianyao Wang, Koroush Shirvan, Frank A Garner, Lin Shao, Irradiation-induced swelling of pure chromium with 5 MeV Fe ions in the temperature range 450–650° C, J. Nucl. Mat. 543, 152585 (2021).

[13] GS Was, Z Jiao, E Getto, K Sun, AM Monterrosa, SA Maloy, O Anderoglu, BH Sencer, M Hackett, Emulation of reactor irradiation damage using ion beams, Scripta Materialia 88, 33-36 (2014).

[14] SJ Zinkle, LL Snead, Opportunities and limitations for ion beams in radiation effects studies: Bridging critical gaps between charged particle and neutron irradiations, Scripta Materialia 143, 154-160 (2018).

[15] J.G. Gigax, Eda Aydogan, Tianyi Chen, Di Chen, Lin Shao, Y. Wu, W. Y. lo, Y. Yang, F. A. Garner, The influence of ion beam rastering on the swelling of self-ion irradiated pure iron at 450 °C, Journal of Nuclear Materials 465, 343-348 (2015).

[16] L. Shao, Jonathan Gigax, Di Chen, Hyosim Kim, Frank A. Garner, Jing Wang, Mychailo B. Toloczko, Standardization of accelerator irradiation procedures for simulation of neutron induced damage in reactor structural materials, Journal of Nuclear Materials 409, 251-254 (2017).

[17] J.G. Gigax Hyosim Kim, Eda Aydogan, Frank A. Garner, Stu Maloy & Lin Shao Beam-contamination-induced compositional alteration and its neutron-atypical consequences in ion simulation of neutron-induced void swelling, Mat. Res. Lett. 5, 478-485 (2017).

[18] J.F. Ziegler, M.D. Ziegler, J.P. Biersack, SRIM – the stopping and range of ions in matter, Nucl. Instr. Meth. Phys. Res. B 268 (2010).

[19] R.E. Stoller, M.B. Toloczko, G. S. Was, A. G. Certain, S. Dwaraknath, F. A. Garner, On the use of SRIM for computing radiation damage exposure, Nuclear Instruments and Methods in Phys. Res. B 310, 75-80 (2013).

[20] A.Yu. Konobeyev, U. Fischer, Yu.A. Korovin, S.P. Simakov, Evaluation of effective threshold displacement energies and other data required for the calculation of advanced atomic displacement cross-sections, Nuclear Energy and Technology 3, 169-175 (2017).

[21] J. A. Marqusee and John Ross, Theory of Ostwald ripening: Competitive growth and its dependence on volume fraction, J. Chem. Phys. 80, 536-543 (1984).

[23] A.D. Brailsford, R. Bullough, The rate theory of swelling due to void growth in irradiated metals, J. Nucl. Mat. 44, 121-135 (1972).

[24] L. K. Mansur (1978) Void Swelling in Metals and Alloys Under Irradiation: An Assessment of the Theory, Nuclear Technology 40, 5-34 (1978).

[25] L.K. Mansur, Theory of transitions in dose dependence of radiation effects in structural alloys, Journal of Nuclear Materials 206, 306-323 (1993).

[26] B. H. Sencer and F.A. Garner, "Compositional and Temperature Dependence of Void Swelling in Model Fe-Cr Base Alloys Irradiated in EBR-II", J. Nucl. Mater., 283-287 (2000) 164-168.

[27] F. A. Garner, M. B. Toloczko and B. H. Sencer, "Comparison of Swelling and Irradiation Creep Behavior of fcc-Austenitic and bcc-Ferritic/Martensitic Alloys at High Neutron Exposure", J. Nucl. Mater., 276 (2000) 123-142.

5. MECHANICAL TESTING

5.1 Introduction

In light of the recent Fukushima Daichi reactor accident and the subsequent call for accident tolerant fuels, a spike in interest for chromium as accident tolerant nuclear fuel cladding coating has been prevalent.[1-3] Some of the many advantages of pure chromium are its excellent corrosion resistance in super-heated steam environment such as loss of coolant accidents and the ease of application on existing zirconium-based fuel cladding via cold spraying. [4]

With the rise in interest in pure chromium the swelling behavior of chromium has been investigated [5] and it was found that chromium displays the tendency to develop large numbers of voids at low irradiation doses compared to zircaloy which experiences almost no swelling at low damage dose [6]. This stark difference in swelling behavior can lead to dissimilar growth rates at the chromium zircalloy interface and cause debonding as well as cracking and other types of mechanical failures. In order to establish the viability of pure chromium as an accident tolerant fuel coating, the stress resistance and irradiation hardening of chromium has to be investigated and a correlation ship between reactor temperature irradiation damage and mechanical changes in chromium have to be established. The following study uses the unique ability of accelerator driven proton irradiation and modern micro manipulation and mechanical testing to established said correlations.

Pure chromium substrate is irradiated with 2 MeV protons via the use of particle accelerators to damage levels between 0.5 and 10 dpa which correspond to typical LWR doses. These irradations create damage layers of up to 20 µm depths with increasing damage profile.

With the damage region established, Focused Ion beam analysis is used to manufacture nanometer sized piller inside a single grain and outside the damage region which are subsequently compressed and yield critical mechanical data such as yield stress and in the case of same grain orientation resolved stress.

5.2 Experimental procedure

The chromium substrate was obtained from Goodfellow inc. with a purity of 99.95%. Prior to proton irradiation the samples were prepped via mechanical polishing up to a 2400 grid using Silicon-Carbide sanding paper. The final polish was achieved using a Tenupol 5 twin jet electro-polisher in conjunction with a polishing solution containg 5% perchloric acid and 95 % methanol. The samples were polished using a voltage bias or 19.5 volts and were polished for 20 seconds each. In order to prevent cross contamination the samples were repeatedly rinsed in methanol post polishing. Final drying was accomplished using dried nitrogen gas. The irradaiton was conducted using a 1.7MV General Ionex tandem particle accelerator and SNICS Ion source. The cathode used to obtain the protons in the experiment was a 3:1 mix Ag, TiH powder cathode that was sintered in a cathode copper jacket. The Irradiated are on the sample was set to 4mm x 4mm and the rastered area to 12mmx 12mm. This large amount of oversteer in conjunction with the rastering allows for good uniformity as well as reduction of beam heating effects. The sample temperature was maintained at 350 ºC via means of an internal light bulb heater and temperature feedback via a stage mounted thermocouple. The proton fluence for the chromium substrate was chosen to be 1.78×10^{19} ions/cm^2 for obtaining a peak dpa of 9.5. The correlation between damage and dose was obtained via the usage of SRIM code [6] assuming a displacement energy of 40 eV [7] for chromium and a Kinchean-Pease calculation model[8]. The

4 pillers used for micro pillar manufacturing and compression were located at depths of 5.8 μm (corresponding to 0.5 dpa), 9.8 μm (0.7 dpa), 14.7 μm (1.0 dpa), and 25.3 μm (0 dpa).
The dimension of each pillar was maintained at 3.3μm×3.3μm×6μm. And careful care was taken to manufacture all pillars in the same grain ensuring consistent crystal orientation. The orientation of the grain was determined via the use of EBSD and X-ray diffraction pattern.
Figure 5.1 displays the relative damage experienced by each micropillar with respect to its relative depth.

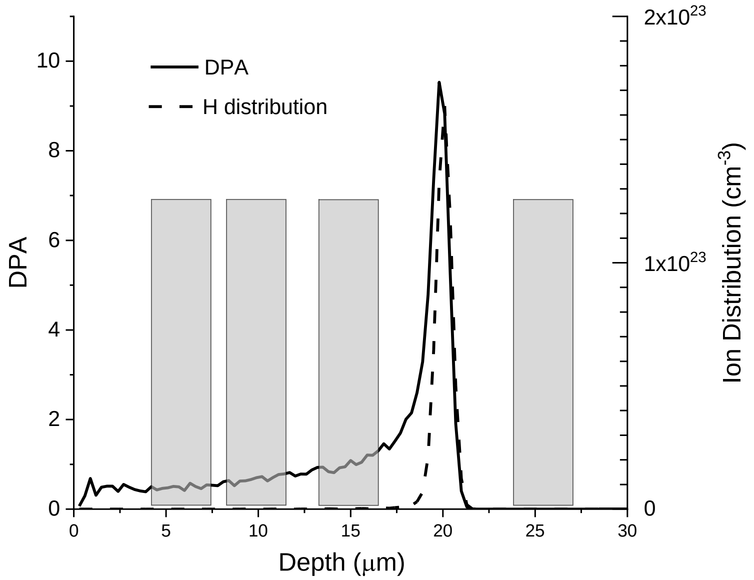

Figure 5.1. Dpa profile (solid line) and H profile (dash line) obtained from SRIM. The shadowed boxes refer to the locations of micro-pillars.

Figure 5.2 a) displays the cross section of the irradiated chromium substrate after polishing with its typical large grains allowing for the manufacture of several micropillars from the same grain, with 5.2 b) depicting the same area after a light polish using a low energy Gallium beam and an overlayed EBSD map overlayed indicating the crystallographic orientation of the different grains. This crystallographic map was subsequently used in the manufacturing of the individual micropillars as seen in Figure 5.3, with the red line indicating the maximum penetration depth

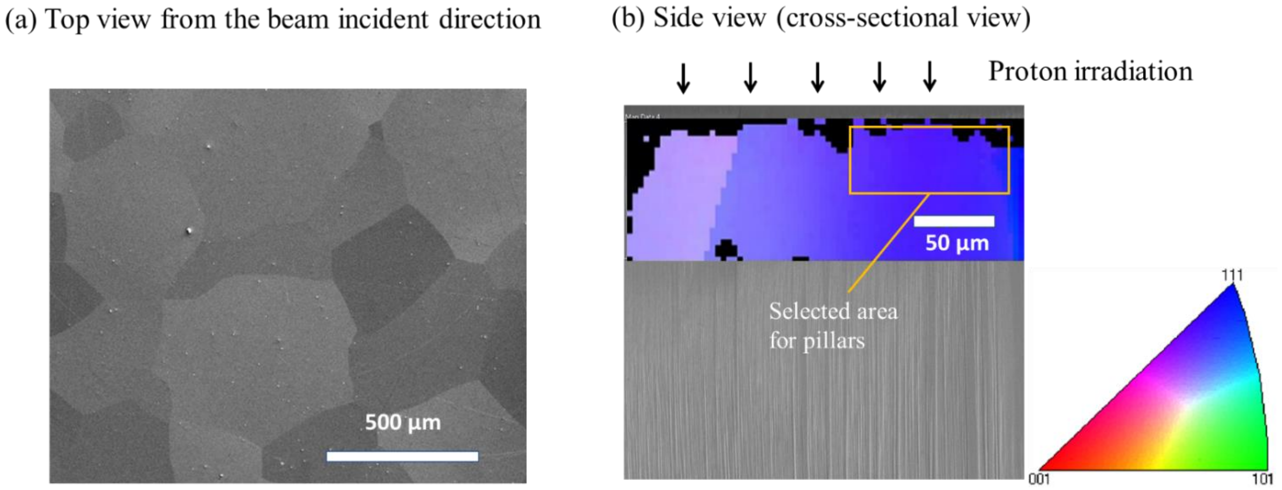
(a) Top view from the beam incident direction

(b) Side view (cross-sectional view)

Figure 5.2 SEM images of (a) the top view of Cr prior to irradiation and (b) the side view (cross-sectional view) of FIB-polished cross section and EBSD mapping of grains. The yellow box refers to the region selected for pillar preparation.

and damage region of the impeding protons. Furthermore, the red arrow indicates the entry direction of the protons and each distinctive square indicates the cross section of a micropillar as seen from a birds eye view (along the z-axis later to be compressed). Pillar compression was performed using a Hysitron PI-85 Picoindenter inside a Tescan LYRA-3 Model GMH. The strain rate of the compression was 0.001 s^{-1}. After the compression, one selected pillar was characterized by using a 200 KeV FEI Talos F200X Scanning/Transmission Electron Microscope (S/TEM). In order to improve the speed and quality of the FIB machining process different instruments were used for each step. A Tescan FERA-3 Model GMH was used for FIB polishing of the cross section and a Tescan LYRA-3 Model GMH was used for pillar fabrication.

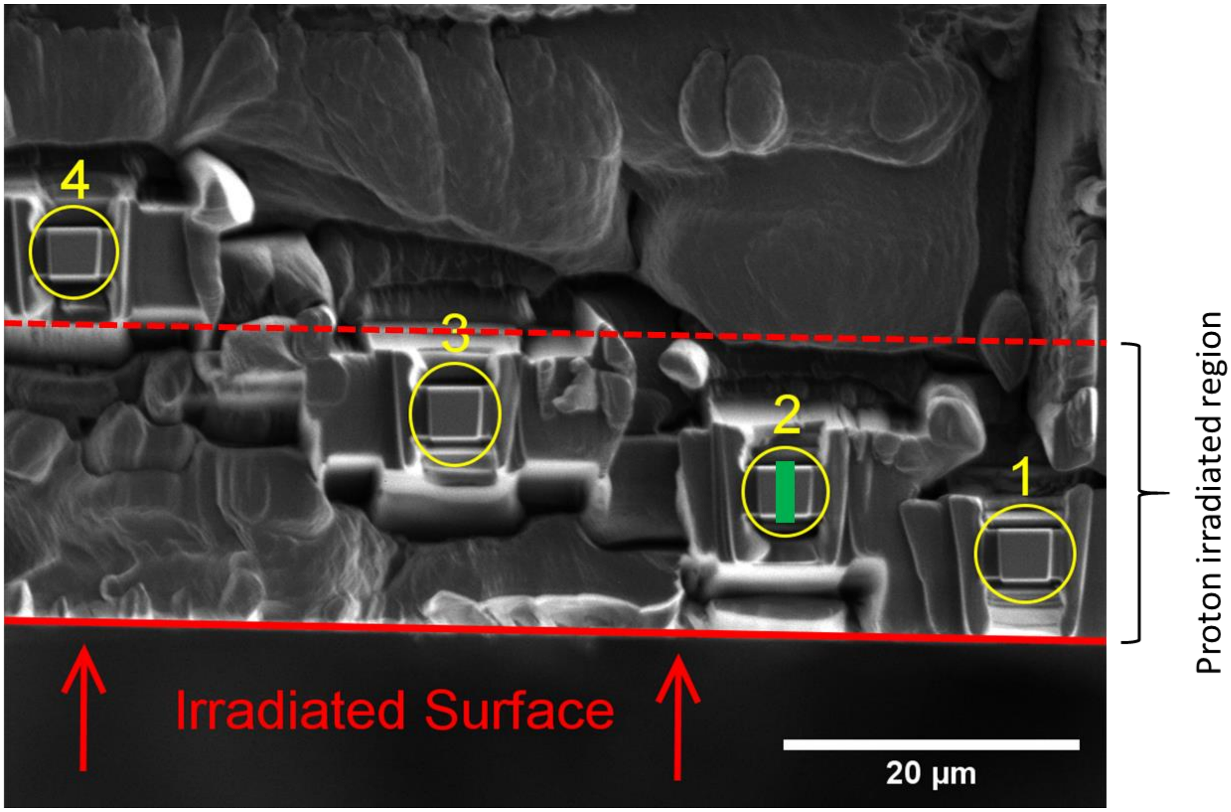

Figure 5.3 SEM image of the cross section of the irradiated chromium. Circles highlight the micro-pillars prepared from FIB. The red line refers to the depth of peak damage, obtained from SRIM simulation. The small green bar over pillar 2 refers to TEM lamellar orientation.

5.3 Summery of Experimental Results

Figure 5.4 displays the engineering stress strain curved as experienced by micropillar number 4 which serves as the unirradiated virgin benchmark. Each image of the institute micro compression is marked via vertical line inside the stress strain curve as a snapshot of the visual deformation of the micropillar in the SEM chamber. The first line and image correspond to the yield stress of the virgin micropillar displaying no visible failure. With increasing stress, slip bands appear at points 2 and 3 and final failure occurs via cracking as seen in point 4 of image 5.4.

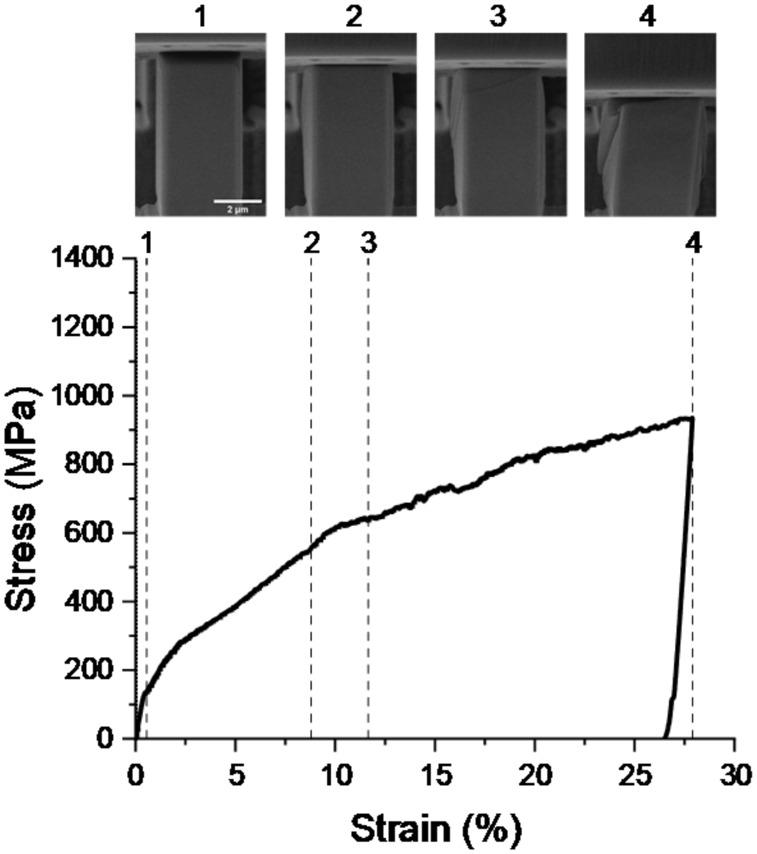

Figure 5.4. Strain-stress curve and SEM images obtained from *in situ* micropillar compression of pillar 4 (corresponding to 0 dpa, and at depth beyond the H protected range).

With a benchmark established in the virgin chromium, the remaing micropillers are compressed with the resulting engineering stress strain curves depicted in Figure 5.5. It can be observed that for all pillars experiencing any kind of irradiation damage, the hardness increases. Particullarly for the pillars experiencing more 0.5 dpa damage, the sensitivity to radiation damage increaseas quickly, with little difference seen between the pillars experiencing 0.7 and 1 dpa damage. The flat tops observed in the irradiated samples are due to the piller hardness exceeding the load capacity of the load cell mounted on the nano indenter used in compressing the pillars. The virgin pillar has small load fluctuations beyond 10% strain, but the entire curve is quite smooth. The smoothness suggests a high friction of dislocation migration, which makes major gliding events difficult. Usually, a major gliding event will lead a large drop/dip in stress causing a relaxation in the material.

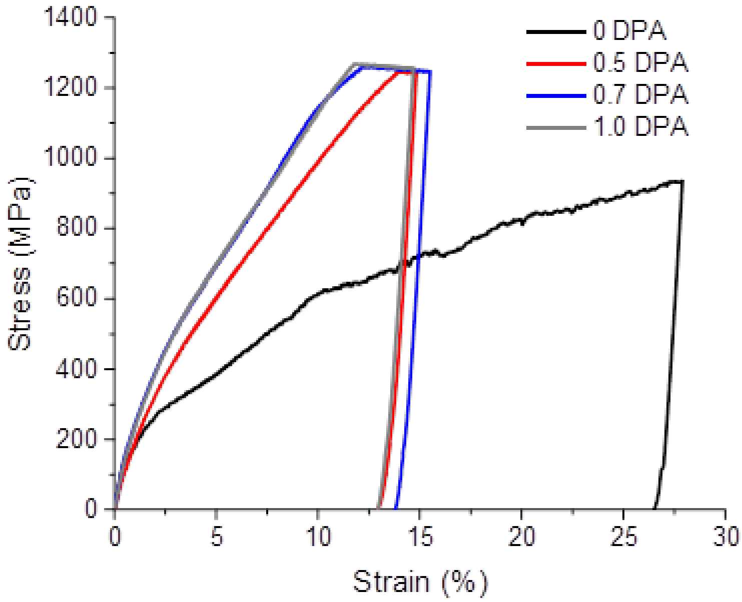

Figure 5.5 Engineering strain-stress curves of micro-pillars at locations corresponding to 0 dpa, 0.5 dpa, 0.7 dpa, and 1 dpa.

Figure 5.6 depicts all micropillers post compression. It can be seen from the images that due to the choise of manufacturing all micropillers inside the same grain orientation the dislocation slippage direction in all pillers is consistent. Further due to this consitent crystal orientation a consistent schmidt factor is experienced across all samples. From the resuslts of the EBSD the gliding direction of the dislocations is [111] on a (100) plane. For the pillar experiencing no irradiation damage, no cracking is observed with narrow gliding bands. Due to the limitation of the loading cell, it could not be determined as this point whether or not the samples experiencing radiation hardening have a higher tendency for cracking under in situ load.

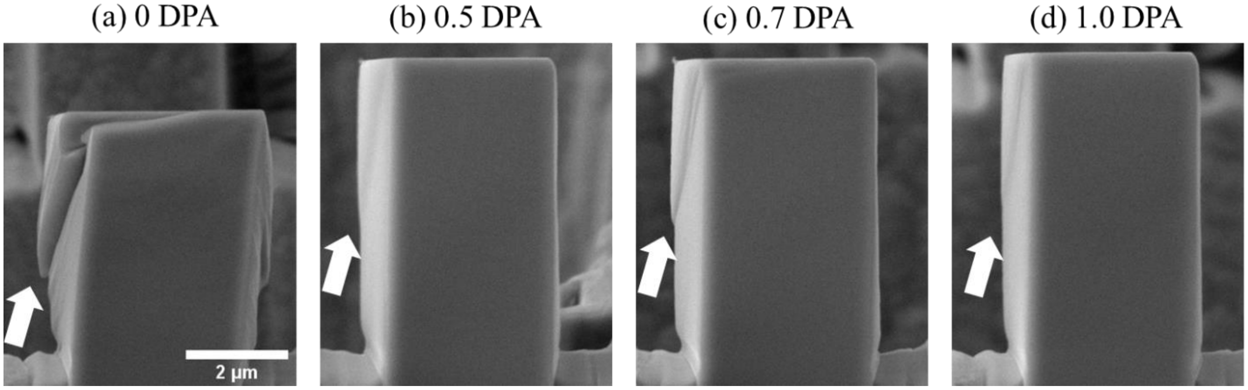

Figure 5.6 SEM images of the pillars (0, 0.5, 0.7, and 1 dpa) at the end of pillar compression. The arrows refer to dislocation gliding direction, which is determined to be [111] on a (110) plane.

Lastly the change in yield stress as normalized to the unirradiated virgin micropillar is depicted in Figure 5.7. the yield stress was chosen via a customary 0.2% offset in strain. It can be observed that for the lowest dose of 0.5 dpa the yield stress increases by 20% and for the highest damage level of 1 dpa the yield stress increases by 57%. Again due to the manufacturing of all pillars along the same crystallographic axis, the increase yield stress corresponds to the increase in resolved critical stress.

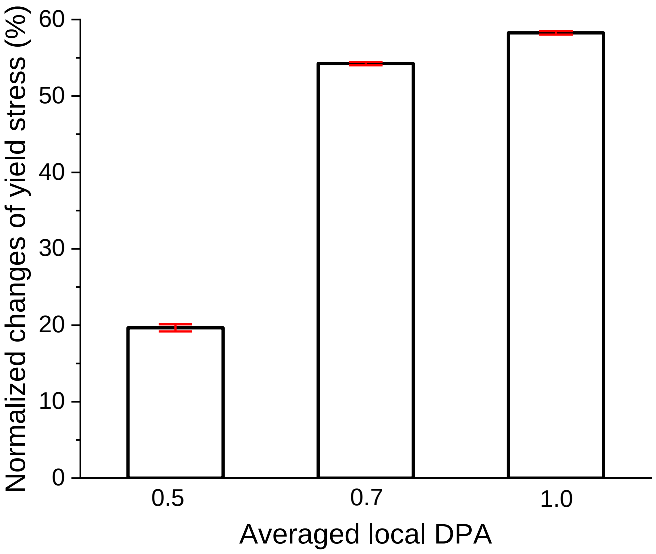

Figure 5.7 Increase in yield stress of proton irradiated micropillars as normalized percentage against virgin micropillar manufactured from the same grain.

5.4 Discussion

The experimental results clearly indicate that the dimensional changes and dissimilar growth of Zircalloy and Chromium can produce stresses which due to the hardening of the chromium under irradiation damage can exceed its established yield stress and cause debonding of the coating and possible catastrophic failure. Therefore, great care must be taken when establishing chromium based coatings on zircalloy based fuel cladding taking into account the mechanical property changes of chromium.

5.5 References

[1] Hyun-Gil Kim, Jae-Ho Yang, Weon-Ju Kim, Yang-Hyun Koo, Development Status of Accident-tolerant Fuel for Light Water Reactors in Korea, Nuclear Engineering and Technology 48, 1-15 (2016).

[2] H.G. Kim, I.H. Kim, Y.I. Jung, D.J. Park, J.Y. Park and Y.H. Koo, Adhesion property and high-temperature oxidation behavior of Cr-coated Zircaloy-4 cladding tube prepared by 3D laser coating, J. Nucl. Mater., 465 (2015), pp. 531-539

[3] Martin Ševeček, Anil Gurgen, Arunkumar Seshadri, Yifeng Che, Malik Wagih, Bren Phillips, Victor Champagne, Koroush Shirvan, Development of Cr cold spray–coated fuel cladding with enhanced accident tolerance, Nuclear Engineering and Technology, Volume 50, Issue 2, March 2018, Pages 229-236 Erences

[4] Ekaterina Ryabikovskaya, Aaron French, Adam Gabriel, Hyosim Kim, Tianyao Wang, Koroush Shirvan, Frank A Garner, Lin Shao, Irradiation-induced swelling of pure chromium with 5 MeV Fe ions in the temperature range 450–650° C, J. Nucl. Mat. 543, 152585 (2021).

[5] Adam Gabriel, Yongchang Li, Aaron French, Zhihan Hu, Frank Garner, Lin Shao, The dpa rate effects on shifting the maximum swelling temperatures of ion-irradiated Cr, submitted.

[6] [SRIM] J.F. Ziegler, M.D. Ziegler, J.P. Biersack, SRIM – the stopping and range of ions in matter, Nucl. Instr. Meth. Phys. Res. B 268 (2010).

[7] R.E. Stoller, M.B. Toloczko, G. S. Was, A. G. Certain, S. Dwaraknath, F. A. Garner, On the use of SRIM for computing radiation damage exposure, Nuclear Instruments and Methods in Phys. Res. B 310, 75-80 (2013).

[8] A.Yu. Konobeyev, U. Fischer, Yu.A. Korovin, S.P. Simakov, Evaluation of effective threshold displacement energies and other data required for the calculation of advanced atomic displacement cross-sections, Nuclear Energy and Technology 3, 169-175 (2017

6. CONCLUSION

With the results presented in this work a cumulative assembly of knowledge on the radiation response of pure chromium has been created. It was found that pure chromium reaches a steady state swelling rate of about 0.045 %/dpa at low and intermediate damage levels and void ordering occurs at high damage levels. A large set of varying temperature and damage rate irradiations were conducted up to 15 peak dpa in pure chromium using 5 MeV Iron Ions and an appropriate formula was obtained to predict the shift of peak swelling temperature in pure chromium of the form $\frac{1}{T_{peak}} = a \times log_{10}K + c$ with constants of $a = -6.74 \times 10^{-5} \pm 2.11 \times 10^{-6}$, and $b = 1.03 \times 10^{-3} \pm 7.48 \times 10^{-7}$. The peak swelling temperature of pure chromium at reactor typical damage rates of 1×10^{-7} dpa/s (LWRs) and 1×10^{-6} dpa/s (fast reactors) are 398 °C and 424 °C respectively. Furthermore pure chromium irradiated up to 1 dpa with 2 MeV protons was mechanically tested via micro pillar compression revealing an increase in yield stress of up to 57 %.